

Compact $cs\bar{s}\bar{s}$ Tetraquarks in the Charm–Strange Sector: Mass Spectra, Rearrangement Decays and Regge Trajectories with D_s Threshold Inputs

Chetan Lodha

Department of Physics, Sardar Vallabhbhai National Institute of Technology,
Surat, Gujarat-395007, India
iamchetanlodha@gmail.com

Ajay Kumar Rai

Department of Physics, Sardar Vallabhbhai National Institute of Technology,
Surat, Gujarat-395007, India
raiajayk@gmail.com

Abstract

This work presents a spectroscopy-focused study of the compact open-charm, multi-strange tetraquark configuration $cs\bar{s}\bar{s}$, modeled as an axial diquark–antidiquark system $[cs][\bar{s}\bar{s}]$. The conventional D_s meson spectrum is retained as a calibration sector for the model parameters and as a reference for the dominant two-meson thresholds; however, the primary emphasis is placed on the mass spectrum, threshold structure, rearrangement decay mechanisms, and Regge systematics of the $cs\bar{s}\bar{s}$ tetraquark. The spectrum is computed within a Cornell-potential framework using both semi-relativistic and non-relativistic treatments, with the $\bar{\mathbf{3}} - \mathbf{3}$ and $\mathbf{6} - \bar{\mathbf{6}}$ color configurations analyzed separately. Owing to the presence of two identical strange antiquarks, Pauli symmetry imposes restrictions on the $[\bar{s}\bar{s}]$ antidiquark, favoring axial-vector building blocks as the natural low-lying degrees of freedom for the $J^P = 0^+, 1^+, 2^+$ tetraquark multiplet. The strong-decay sector is formulated in terms of the rearrangement topology $cs\bar{s}\bar{s} \rightarrow (c\bar{s})(s\bar{s})$, with the $D_s^{(*)}\eta$, $D_s^{(*)}\eta'$, and $D_s^{(*)}\phi$ modes identified through spin-color Fierz recoupling and normalized using two-point and three-point QCD-sum-rule amplitudes. Orbital and radial Regge trajectories are constructed to characterize the excitation patterns of the compact tetraquark and to benchmark them against the calibrated D_s spectrum. This framework provides a dedicated phenomenological basis for identifying $cs\bar{s}\bar{s}$ candidates in hidden-strangeness open-charm final states.

Keywords: $cs\bar{s}\bar{s}$ tetraquark; charm–strange exotics; diquark–antidiquark model; rearrangement decay; QCD sum rules; Regge trajectories; D_s thresholds.

1 Introduction

Quantum chromodynamics (QCD) allows any color-singlet combination of quarks and gluons, although the conventional quark model organizes most established hadrons as $q\bar{q}$ mesons and qqq baryons [1–3]. The success of this classification does not exclude multiquark states, hadronic molecules, hybrids, threshold cusps, or dynamically generated coupled-channel poles. Since the observation of the $X(3872)$, many candidates outside a simple quarkonium picture have appeared in hidden-charm, hidden-strange, and

open-flavor channels [4–13]. Open-flavor systems are particularly useful because their flavor quantum numbers can prevent an ordinary quarkonium assignment and make the roles of color correlations, Fermi symmetry, and meson–meson thresholds more transparent.

The charm–strange sector provides a natural setting for such studies. The narrow $D_{s_0}^*(2317)$ and $D_{s_1}(2460)$ states lie below early relativized quark-model expectations and have motivated interpretations involving compact tetraquark components, DK or D^*K molecules, and strong coupled-channel effects [12, 14–19]. More recently, LHCb observations of open-charm strange structures, including the neutral $T_{cs_0}^*(2870)^0$, have shown that scalar and near-threshold resonances in DK -type channels can be accessed experimentally in heavy-flavor decays [9–11, 20]. Although these states do not have the same minimal flavor content as $cs\bar{s}\bar{s}$, they demonstrate that strange open-charm exotics can be studied through reconstructed charm mesons and provide useful guidance for more strange-rich configurations.

Detailed $c\bar{s}$ spectroscopy has therefore been developed in several complementary frameworks. Relativized and nonrelativistic quark models, including the Godfrey–Isgur model and later heavy-light potential calculations, provide reference spectra for orbital and radial D_s excitations, Regge trajectories, decay constants, and strong-decay patterns [17, 21–25]. Related calculations in the non-strange D sector help isolate the effect of replacing a light quark by a strange quark in the charm-light interaction [26]. Heavy-quark chiral symmetry, unitarized coupled-channel approaches, and molecular models explain how positive-parity D_s masses can be shifted by nearby DK and D^*K thresholds [12, 18, 27–29], while lattice-QCD calculations with explicit scattering operators further support the importance of threshold dynamics [19, 30, 31]. These conventional $D_s^{(*)}$ inputs are essential here because they set both the calibration scale and the rearrangement thresholds of the $cs\bar{s}\bar{s}$ tetraquark. They also allow the tetraquark spectrum to be discussed in the same mass convention as the experimentally established charm–strange mesons, which is necessary when identifying states close to $D_s^{(*)}X_s$ thresholds.

Theoretical analyses of open-charm tetraquarks use a similarly broad set of tools. Constituent potential models describe compact states through quark masses, one-gluon-exchange Coulomb terms, confinement, and spin-dependent interactions, while diquark–antidiquark models emphasize effective $\mathbf{\bar{3}}_c \otimes \mathbf{3}_c$ and $\mathbf{6}_c \otimes \mathbf{\bar{6}}_c$ color couplings [4, 32]. QCD sum rules test whether compact or molecular interpolating currents can support the relevant masses and residues [33–35], whereas molecular, coupled-channel, lattice-QCD, and Born–Oppenheimer approaches focus on pole generation, finite-volume levels, and heavy-quark static potentials [13, 19, 36]. Chiral SU(3) quark-model work has already examined $cn\bar{n}\bar{s}$ and $cs\bar{s}\bar{s}$ configurations in connection with the anomalous $D_{s,J}$ states [37], and related diquark–antidiquark studies in all-charm, hidden charm–hidden strange, all-light, and light-strange sectors provide useful comparisons for spin splittings, color configurations, Regge behavior, and decay mechanisms [38–41]. These approaches differ in their treatment of clustering and thresholds, but together they show which observables are most useful: masses relative to two-meson thresholds, color-spin splittings, Regge regularity, and allowed decay modes.

The $cs\bar{s}\bar{s}$ tetraquark is less explored than hidden-charm or non-strange open-charm systems, but it is especially useful for testing the interplay of compact color structure and hidden-strangeness thresholds. Its dominant rearrangement topology is

$$cs\bar{s}\bar{s} \rightarrow (c\bar{s})(s\bar{s}),$$

which naturally gives final states such as $D_s^{(*)}\eta$, $D_s^{(*)}\eta'$, and $D_s^{(*)}\phi$ after physical η – η' mixing. This flavor flow separates it from the more commonly discussed $cq\bar{s}\bar{q}$, $c\bar{s}q\bar{q}$, and $cs\bar{q}\bar{q}$ configurations and suggests experimental searches in hidden-strangeness open-charm final states. The appearance of η , η' , and ϕ in the daughter system is also useful phenomenologically because it connects the tetraquark signal to well-studied strangeonium components, while the accompanying $D_s^{(*)}$ meson tags the open-charm flavor unambiguously. The two identical strange antiquarks also impose a strong Pauli constraint. For a

ground-state $[\bar{s}\bar{s}]$ antiquark, the flavor and spatial wave functions are symmetric; in the color-triplet channel the color part is antisymmetric, so Fermi statistics requires a symmetric spin wave function. The lowest $[\bar{s}\bar{s}]$ cluster is therefore axial rather than scalar, and coupling it to a $[cs]$ diquark produces the low-lying $J^P = 0^+, 1^+, 2^+$ multiplet considered in this work [4, 32, 39].

For a phenomenological calculation, this system requires three ingredients: a calibrated D_s spectrum for the relevant $D_s^{(*)}\eta^{(\prime)}$ and $D_s^{(*)}\phi$ thresholds, explicit treatment of the $\bar{\mathbf{3}}_c \otimes \mathbf{3}_c$ and $\mathbf{6}_c \otimes \bar{\mathbf{6}}_c$ color structures, and decay information that can distinguish compact levels from broad threshold enhancements. We therefore construct the $cs\bar{s}\bar{s}$ state as $[cs][\bar{s}\bar{s}]$, impose the Pauli restriction on the identical antiquarks, and calculate the $J^P = 0^+, 1^+, 2^+$ ground multiplet together with radial and orbital excitations. The masses are compared with relevant two-meson thresholds and previous open-charm strange predictions, and the decay analysis is formulated through spin-color rearrangement into $D_s^{(*)}$ plus hidden-strangeness mesons. In this way the calculation keeps the compact diquark–antidiquark picture as the central organizing scheme, but still records the threshold information needed to judge whether a predicted level is likely to appear as a narrow candidate, a broad enhancement, or a state strongly mixed with nearby meson–meson channels. The same spectrum is further organized through Regge trajectories so that the compact tetraquark patterns can be compared with the calibrated D_s baseline.

The paper is organized as follows. Section 2 presents the theoretical framework, including the potential model, spin-dependent interactions, color factors, and Pauli constraints. Section 3 gives the D_s calibration, axial diquark inputs, and compact $cs\bar{s}\bar{s}$ spectra. Section 4 discusses radial and orbital Regge trajectories, Section 5 presents the decay analysis and hidden-strangeness rearrangement widths, Section 6 discusses the main phenomenological implications, and Section 7 summarizes the conclusions.

2 Theoretical Framework

The present framework is designed to isolate the compact $cs\bar{s}\bar{s}$ tetraquark while keeping the conventional D_s sector as a calibration and threshold reference. It extends our earlier investigations of singly charmed tetraquark systems by replacing the light constituents of the previously analyzed $cq\bar{q}\bar{q}$ configuration with strange constituents and by focusing on the multi-strange open-charm flavor assignment $[cs][\bar{s}\bar{s}]$ [42, 43]. Both semi-relativistic and non-relativistic formalisms are employed so that the sensitivity of the predicted tetraquark masses to the charm–strange kinetic treatment can be assessed explicitly.

A defining feature of the $cs\bar{s}\bar{s}$ configuration is the presence of two identical strange antiquarks in the antiquark cluster. For the ground-state $[\bar{s}\bar{s}]$ antiquark in the color-triplet configuration, the spatial wavefunction is taken to be symmetric, while the color part is antisymmetric. The Pauli principle then requires the spin-flavor part to be symmetric; since the flavor component is already symmetric, the allowed antiquark spin is $S_{\bar{D}} = 1$. This makes axial-vector $[cs]$ and $[\bar{s}\bar{s}]$ clusters the natural building blocks for the low-lying $J^P = 0^+, 1^+, 2^+$ $cs\bar{s}\bar{s}$ multiplet, in line with QCD-sum-rule analyses of related axial-diquark open-charm strange tetraquarks [35].

To evaluate the masses and binding energies of the resulting states, we employ a modified time-independent radial Schrödinger equation in the center-of-mass frame [44]. The semi-relativistic and non-relativistic Hamiltonians are written as

$$H_{SR} = \sum_{i=1}^2 \sqrt{M_i^2 + p_i^2} + V^{(0)}(r) + V_{SD}(r), \quad (1)$$

$$H_{NR} = \sum_{i=1}^2 \left(\frac{p_i^2}{2M_i} + M_i \right) + V^{(0)}(r) + V_{SD}(r), \quad (2)$$

where M_i , p_i , $V^{(0)}(r)$, and $V_{SD}(r)$ denote the constituent masses, the relative momentum, the central interaction potential, and the spin-dependent interaction, respectively.

The kinetic term is expanded up to $\mathcal{O}(p^6)$,

$$K.E. = \sum_{i=1}^2 \left[\frac{p^2}{2M_i} - \frac{p^4}{8M_i^3} + \frac{p^6}{16M_i^5} \right], \quad (3)$$

which improves the treatment of systems containing both charm and strange constituents. The interquark interaction is modeled through the Cornell potential,

$$V_{C+L}^{(0)}(r) = \frac{k_s \alpha_s}{r} + br + V_0, \quad (4)$$

where k_s is the color factor, α_s is the effective running coupling, b is the string tension, and V_0 is a phenomenological constant. The full effective potential is written as

$$V^{(0)}(r) = V_{C+L}^{(0)}(r) + V^1(r) \left(\frac{1}{m_1} + \frac{1}{m_2} \right), \quad (5)$$

with the leading-order mass correction

$$V^1(r) = -\frac{C_F C_A \alpha_s^2}{4 r^2}, \quad (6)$$

where $C_F = 4/3$ and $C_A = 3$ [45, 46].

The spin-dependent interaction is treated perturbatively and decomposed into tensor, spin-orbit, and spin-spin contributions,

$$V_{SD}(r) = V_T(r) + V_{LS}(r) + V_{SS}(r), \quad (7)$$

with the explicit Breit-Fermi forms given by

$$\left(-\frac{k_s \alpha_s}{4} \frac{12\pi}{M_{\mathcal{D}} M_{\bar{\mathcal{D}}}} \frac{1}{r^3} \right) \left(-\frac{1}{3} (S_1 \cdot S_2) + \frac{(S_1 \cdot r)(S_2 \cdot r)}{r^2} \right), \quad (8a)$$

$$\left(-\frac{3\pi k_s \alpha_s}{2M_{\mathcal{D}} M_{\bar{\mathcal{D}}}} \frac{1}{r^3} - \frac{b}{2M_{\mathcal{D}} M_{\bar{\mathcal{D}}}} \frac{1}{r} \right) (L \cdot S), \quad (8b)$$

$$\left(-\frac{k_s \alpha_s}{3} \frac{8\pi}{M_{\mathcal{D}} M_{\bar{\mathcal{D}}}} \left(\frac{\sigma}{\sqrt{\pi}} \right)^3 e^{-\sigma^2 r^2} \right) (S_1 \cdot S_2). \quad (8c)$$

These terms generate the fine and hyperfine splittings that distinguish states with the same orbital structure but different spin couplings. The resulting framework has been used consistently in our earlier open-charm and multiquark studies and is retained here for the charm-strange sector.

3 Spectroscopy

3.1 Meson Spectra

We begin with the mass spectra of the D_s meson family not as the main target of the paper, but as the calibration sector required for fixing the charm–strange model parameters and for constructing the $D_s^{(*)} \eta^{(\prime)}$ and $D_s^{(*)} \phi$ thresholds relevant to the $cs\bar{s}\bar{s}$ tetraquark analysis. Within SU(3) color symmetry, a meson is formed from the color-singlet combination $\bar{\mathbf{3}} \otimes \mathbf{3} = \mathbf{1} \oplus \mathbf{8}$, with the singlet channel corresponding

to the color factor $k_s = -4/3$. The mass of an individual $[c\bar{s}]$ state is written as

$$M_{(c\bar{s})} = M_c + M_{\bar{s}} + E_{(c\bar{s})} + \langle V^0(r) \rangle, \quad (9)$$

where M_c and M_s denote the constituent charm- and strange-quark masses and $E_{(c\bar{s})}$ is the corresponding binding energy. The final masses listed below include both the relativistic corrections to the kinetic energy and the spin-dependent interaction contributions. The predicted spectrum of the D_s family is presented in Table 1.

Note: The states are listed in the unmixed LS -coupling basis. For the heavy-light $c\bar{s}$ system, states with the same J^P , such as n^1P_1 - n^3P_1 , n^1D_2 - n^3D_2 , and n^1F_3 - n^3F_3 , can mix to form the physical meson states.

Table 1: Central D_s meson masses in MeV. Present semi-relativistic (SR) and non-relativistic (NR) results are compared with the experimental central values compiled by the Particle Data Group [3] and with selected theoretical studies

State	J^P	Present		Comparison							
		SR	NR	[3]	[23]	[24]	[47]	[48]	[22]	[49]	[50]
L = 0 states											
1^1S_0	0^-	1967.9	2003.5	1968.35	1970	1965	1966	1969	1969	1979	1969
2^1S_0	0^-	2560.1	2599.2	–	2688	2680	2645	2649	2688	2673	2709
3^1S_0	0^-	2955.9	3004.2	–	3158	3247	3118	3126	3219	3154	3139
4^1S_0	0^-	3298.5	3342.8	–	3556	3764	3487	–	3652	3547	3481
1^3S_1	1^-	2113.1	2128.7	2112.2	2117	2120	2119	2112	2111	2129	2087
2^3S_1	1^-	2637.1	2665.5	2714	2723	2719	2683	2737	2731	2732	2714
3^3S_1	1^-	3010.9	3054.5	–	3180	3265	3135	3191	3242	3193	3139
4^3S_1	1^-	3336.1	3384.8	–	3571	3775	3496	–	3669	3575	3481
L = 1 states											
1^1P_1	1^+	2474.8	2495.4	2535.11	2530	2529	2534	2528	2536	2549	2524
2^1P_1	1^+	2866.8	2904.6	–	3019	3081	3015	3002	3067	3018	3019
3^1P_1	1^+	3198.6	3247.2	–	–	3587	3401	–	3618	3416	3384
4^1P_1	1^+	3510.2	3551.9	–	–	–	3719	–	–	3764	3691
1^3P_0	0^+	2382.7	2402.3	2317.8	2444	2438	2436	2409	2509	2484	2461
2^3P_0	0^+	2780.7	2817.3	–	2947	3022	2958	2940	3054	3005	3003
3^3P_0	0^+	3114.1	3162.3	–	–	3541	3358	–	3513	3412	3377
4^3P_0	0^+	3424.7	3468.3	–	–	–	3685	–	–	3764	3687
1^3P_1	1^+	2466.0	2485.6	2459.5	2540	2541	2485	2545	2574	2556	2535
2^3P_1	1^+	2858.7	2895.3	–	3023	3092	2987	3026	3154	3038	3009
3^3P_1	1^+	3189.8	3237.9	–	–	3596	3379	–	3519	3433	3373
4^3P_1	1^+	3499.0	3542.6	–	–	–	3702	–	–	3778	3680
1^3P_2	2^+	2512.0	2531.6	2569.1	2566	2569	2548	2575	2571	2592	2572
2^3P_2	2^+	2905.4	2942.0	–	3048	3109	3022	3053	3142	3048	3015
3^3P_2	2^+	3237.2	3285.3	–	–	3609	3405	–	3580	3439	3374
4^3P_2	2^+	3546.9	3590.5	–	–	–	3722	–	–	3783	3680
L = 2 states											
1^1D_2	2^-	2737.0	2765.0	–	2816	2853	2844	2857	2931	2900	2883
2^1D_2	2^-	3077.6	3121.4	–	3312	3368	3262	3267	3403	3298	3278
3^1D_2	2^-	3386.9	3435.5	–	–	3857	3606	–	–	3650	3600
4^1D_2	2^-	3691.2	3721.7	–	–	–	3895	–	–	–	–
1^3D_1	1^-	2729.4	2757.3	–	2873	2882	2866	2843	2913	2899	2857
2^3D_1	1^-	3065.8	3109.5	–	3292	3394	3280	3233	3383	3306	3268
3^3D_1	1^-	3372.5	3421.1	–	–	3858	3620	–	–	3658	3596
4^3D_1	1^-	3674.6	3705.6	–	–	–	3907	–	–	–	–
1^3D_2	2^-	2740.7	2768.7	–	2896	2872	2836	2911	2961	2926	2869
2^3D_2	2^-	3079.9	3123.6	–	3248	3384	3258	3306	3456	3323	3259
3^3D_2	2^-	3388.3	3436.9	–	–	3869	3602	–	–	3672	3581
4^3D_2	2^-	3691.7	3722.6	–	–	–	3892	–	–	–	–
1^3D_3	3^-	2738.5	2766.4	2860	2834	2860	2841	2882	2971	2917	2886
2^3D_3	3^-	3082.5	3126.2	–	3263	3372	3258	3299	3469	3311	3264
3^3D_3	3^-	3393.9	3442.5	–	–	3878	3602	–	–	3661	3583
4^3D_3	3^-	3699.5	3730.4	–	–	–	3892	–	–	–	–
L = 3 states											
1^1F_3	3^+	2949.1	2986.0	–	–	–	3095	3123	3254	3186	3164
2^1F_3	3^+	3262.0	3310.3	–	–	–	3472	–	–	3540	3505

Continued on next page

Table 1 – continued from previous page

State	J^P	Present		Comparison							
		SR	NR	[3]	[23]	[24]	[47]	[48]	[22]	[49]	[50]
3^1F_3	3^+	3561.1	3604.2	–	–	–	3786	–	–	–	–
4^1F_3	3^+	3867.7	3876.3	–	–	–	4051	–	–	–	–
1^3F_2	2^+	2962.2	2999.0	–	–	–	3122	3176	3230	3208	3148
2^3F_2	2^+	3270.6	3318.9	–	–	–	3493	–	–	3562	3498
3^3F_2	2^+	3566.5	3609.7	–	–	–	3803	–	–	–	–
4^3F_2	2^+	3870.8	3879.4	–	–	–	4066	–	–	–	–
1^3F_3	3^+	2954.9	2991.7	–	–	–	3096	3205	3266	3218	3138
2^3F_3	3^+	3266.6	3314.9	–	–	–	3473	–	–	3569	3478
3^3F_3	3^+	3564.9	3608.0	–	–	–	3787	–	–	–	–
4^3F_3	3^+	3870.9	3879.5	–	–	–	4052	–	–	–	–
1^3F_4	4^+	2937.4	2974.3	–	–	–	3080	3134	3300	3190	3149
2^3F_4	4^+	3253.8	3302.1	–	–	–	3460	–	–	3544	3482
3^3F_4	4^+	3555.3	3598.4	–	–	–	3775	–	–	–	–
4^3F_4	4^+	3863.6	3872.3	–	–	–	4042	–	–	–	–

3.2 Diquarks

Diquarks (\mathcal{D}) and antidiquarks ($\bar{\mathcal{D}}$) are correlated two-quark and two-antiquark subsystems held together by gluonic exchange, and they provide an effective description of the internal structure of multi-quark hadrons. Although they are not observed as free particles, diquarks play an important role in the quark–diquark description of baryons and in the construction of compact tetraquarks and pentaquarks [51]. In the present work, the $cs\bar{s}\bar{s}$ tetraquark is described as a bound state of a $[cs]$ diquark and a $[\bar{s}\bar{s}]$ antidiquark. Within the framework of QCD color symmetry, diquarks transform as $\mathbf{3} \otimes \mathbf{3} = \bar{\mathbf{3}} \oplus \mathbf{6}$ [52], while antidiquarks transform as $\bar{\mathbf{3}} \otimes \bar{\mathbf{3}} = \mathbf{3} \oplus \bar{\mathbf{6}}$. The color-antitriplet channel is attractive, with color factor $k_s = -\frac{2}{3}$, whereas the sextet channel is repulsive, with $k_s = \frac{1}{3}$ [53]. Modeling the tetraquark as a diquark–antidiquark bound system effectively reduces the four-body problem to a two-body one [54].

For the present flavor assignment, the diquark basis is more constrained than in generic open-charm tetraquarks. The $[\bar{s}\bar{s}]$ antidiquark cannot be chosen independently in scalar and axial channels once the identical-antiquark Pauli constraint is imposed; the low-lying compact basis is therefore dominated by axial-vector clusters. This feature is important because recent QCD-sum-rule studies of strange and doubly strange open-charm tetraquarks also identify axial-vector diquark–antidiquark currents as a natural source of the 0^+ , 1^+ , and 2^+ spin multiplet [35]. The same flavor structure makes the $cs\bar{s}\bar{s}$ state complementary to molecular descriptions of T_{cs} and $T_{c\bar{s}}$ candidates, where the long-distance degrees of freedom are two color-singlet mesons rather than compact color-correlated clusters [36].

In the present spectroscopy, the tetraquark basis is constructed from axial-vector diquark and antidiquark building blocks. Accordingly, the relevant diquark inputs are the 1^3S_1 states of $[cs]$ and $[ss]$, while the mass of the $[\bar{s}\bar{s}]$ antidiquark is taken to be equal to that of the corresponding $[ss]$ diquark. The methodology for calculating diquark and antidiquark masses parallels that used for mesons, and the resulting masses are expressed as

$$M_{(ss)} = 2M_s + E_{(ss)} + \langle V^0(r) \rangle, \quad (10a)$$

$$M_{(cs)} = M_c + M_s + E_{(cs)} + \langle V^0(r) \rangle. \quad (10b)$$

Here, M_s and M_c denote the constituent strange- and charm-quark masses, while $E_{(ss)}$ and $E_{(cs)}$ are the corresponding diquark binding energies. The calculated masses of the axial-vector diquarks used in the present work are summarized in Table 2.

Table 2: Mass spectra of the axial-vector $[cs]$ and $[ss]$ diquarks employed in the present $cs\bar{s}\bar{s}$ tetraquark calculation, with comparison values from the relativistic diquark model of Ebert–Faustov–Galkin [32]. Related light- and heavy-light-diquark Regge treatments are discussed in Refs. [55,56]. The corresponding antiquark masses are taken to be identical. All values are in MeV.

Diquark	Present work				Ref. [32]
	$\bar{\mathbf{3}}$ [SR]	$\bar{\mathbf{3}}$ [NR]	$\mathbf{6}$ [SR]	$\mathbf{6}$ [NR]	
$[cs]_A$	2214.23 ± 21.39	2225.75 ± 21.34	2257.53 ± 38.28	2259.37 ± 38.26	2158
$[ss]_A$	1317.32 ± 12.81	1329.08 ± 12.64	1337.93 ± 12.81	1340.16 ± 12.76	1203

3.3 Tetraquark Spectra

In a color-singlet state, the compact $cs\bar{s}\bar{s}$ tetraquark can be realized through two possible diquark–antidiquark couplings: (i) a color antitriplet diquark combined with a color triplet antidiquark, $\bar{\mathbf{3}} - \mathbf{3}$, and (ii) a color sextet diquark combined with a color antisextet antidiquark, $\mathbf{6} - \bar{\mathbf{6}}$. For the interaction between the diquark and antidiquark clusters, the corresponding color factors are taken as $k_s = -\frac{4}{3}$ and $k_{\bar{s}} = -\frac{10}{3}$, respectively [52,57]. In the present construction, both the diquark and antidiquark are treated as axial-vector constituents, $S_d = S_{\bar{d}} = 1$, so that the total tetraquark spin can take the values $S_T = 0, 1$, and 2. The overall parity is determined by the relative orbital angular momentum, $P = (-1)^{L_T}$.

This choice of basis is motivated by the small but growing body of work devoted specifically to multi-strange open-charm tetraquarks. The chiral SU(3) quark model studied $cn\bar{n}\bar{s}/cs\bar{s}\bar{s}$ configurations in relation to the anomalous D_{sJ} states [37]; relativistic diquark–antidiquark models explored open-charm and charm-strange tetraquark masses [32]; QCD sum rules analyzed strange and doubly strange $T_{c\bar{s}}$ partners with $J^P = 0^+, 1^+, 2^+$ [35]; and recent four-body Gaussian-expansion plus complex-scaling calculations found no bound $Qs\bar{s}\bar{s}$ states below the lowest thresholds but predicted compact charm resonances around the 3.7–3.9 GeV region [58]. The present calculation is therefore aimed at providing a potential-model counterpart to these approaches, with the same flavor content and explicit threshold offsets.

Within this framework, the mass of the compact $cs\bar{s}\bar{s}$ tetraquark is written as

$$M_{cs\bar{s}\bar{s}} = M_{cs} + M_{\bar{s}\bar{s}} + E_{(cs\bar{s}\bar{s})} + \langle V^0(r) \rangle. \quad (11)$$

The calculated mass spectra receive contributions from the Cornell-like interaction, relativistic corrections to the kinetic term, and spin-dependent interactions, including the spin–spin, spin–orbit, and tensor terms. To classify the resulting states, we use the basis

$$|T\rangle = |S_d, S_{\bar{d}}, S_T, L_T\rangle_{J_T}, \quad (12)$$

where S_d and $S_{\bar{d}}$ denote the spins of the diquark and antidiquark, respectively, S_T is the total spin, L_T is the relative orbital angular momentum, and J_T is the total angular momentum of the tetraquark. For the S -wave configurations considered here, the allowed states are

$$\begin{aligned} |0^+\rangle_T &= |1, 1, 0, 0\rangle_0, \\ |1^+\rangle_T &= |1, 1, 1, 0\rangle_1, \\ |2^+\rangle_T &= |1, 1, 2, 0\rangle_2. \end{aligned} \quad (13)$$

The present study adopts the compact diquark–antidiquark approximation, which reduces the full four-body system to an effective two-body problem and permits a systematic implementation of the

Cornell potential and its spin-dependent corrections. Meson–meson molecular configurations are not treated explicitly in this work, since they require a different dynamical framework. The computed mass spectra of the $c\bar{s}\bar{s}$ tetraquark for the $\bar{\mathbf{3}} - \mathbf{3}$ and $\mathbf{6} - \bar{\mathbf{6}}$ configurations are presented together in Table 3, where each state is listed once and the masses for the two color configurations are shown side by side. The two-meson thresholds in Table 4 are supplemented by $\Delta = M_T - M_{\text{th}}$, evaluated with the corresponding ground-state tetraquark mass for both color configurations.

Table 3: Predicted mass spectra of the compact $c\bar{s}\bar{s}$ tetraquark for the S , P , and D waves in the diquark–antidiquark framework [4, 32, 35, 37, 58]. The masses are shown side by side for the $\bar{\mathbf{3}} - \mathbf{3}$ and $\mathbf{6} - \bar{\mathbf{6}}$ color configurations in both the semi-relativistic (SR) and non-relativistic (NR) schemes. All values are in MeV.

State	J^P	$\bar{\mathbf{3}} - \mathbf{3}$		$\mathbf{6} - \bar{\mathbf{6}}$	
		Semi-Relativistic	Non-Relativistic	Semi-Relativistic	Non-Relativistic
S-wave states					
1^1S_0	0^+	3345.41 ± 41.76	3379.82 ± 41.80	3564.42 ± 474.28	2595.46 ± 63.34
2^1S_0	0^+	3932.67 ± 43.00	3955.09 ± 42.80	3424.00 ± 42.48	3481.52 ± 41.40
3^1S_0	0^+	4261.53 ± 67.96	4289.22 ± 67.74	3939.72 ± 34.34	3984.00 ± 34.26
4^1S_0	0^+	4523.12 ± 52.81	4558.17 ± 52.41	4277.07 ± 35.90	4323.04 ± 35.65
1^3S_1	1^+	3451.20 ± 73.29	3474.11 ± 72.90	3564.42 ± 371.31	2595.46 ± 38.76
2^3S_1	1^+	3968.39 ± 56.94	3987.37 ± 56.87	3424.00 ± 52.18	3481.52 ± 52.09
3^3S_1	1^+	4285.75 ± 36.68	4310.88 ± 36.57	3939.72 ± 45.47	3984.00 ± 44.74
4^3S_1	1^+	4542.32 ± 46.04	4575.15 ± 45.63	4277.07 ± 57.05	4323.04 ± 56.28
1^5S_2	2^+	3656.37 ± 48.09	3662.70 ± 48.32	3564.42 ± 217.07	2595.46 ± 47.04
2^5S_2	2^+	4039.07 ± 32.83	4051.93 ± 32.93	3424.00 ± 70.23	3481.52 ± 69.54
3^5S_2	2^+	4333.86 ± 39.02	4354.18 ± 39.04	3939.72 ± 52.80	3984.00 ± 52.56
4^5S_2	2^+	4580.56 ± 50.23	4609.11 ± 49.71	4277.07 ± 66.08	4323.04 ± 65.36
P-wave states					
1^1P_1	1^-	3862.80 ± 55.28	3877.57 ± 55.04	3374.72 ± 39.76	3425.82 ± 38.86
2^1P_1	1^-	4192.61 ± 30.03	4213.56 ± 29.85	3892.32 ± 43.82	3931.09 ± 43.06
3^1P_1	1^-	4456.83 ± 43.32	4485.41 ± 43.03	4231.34 ± 28.57	4272.11 ± 28.08
4^1P_1	1^-	4686.59 ± 45.36	4723.46 ± 44.90	4503.01 ± 34.00	4548.97 ± 33.72
1^3P_0	0^-	3781.56 ± 60.37	3795.71 ± 60.29	2216.30 ± 82.37	2305.98 ± 79.05
2^3P_0	0^-	4124.81 ± 49.79	4145.03 ± 49.44	3215.69 ± 65.33	3275.82 ± 63.82
3^3P_0	0^-	4394.47 ± 38.28	4422.23 ± 38.03	3704.61 ± 41.39	3761.55 ± 40.67
4^3P_0	0^-	4627.22 ± 59.28	4663.23 ± 58.75	4049.34 ± 58.82	4109.08 ± 57.84
1^3P_1	1^-	3851.06 ± 44.20	3865.21 ± 44.04	3322.48 ± 45.72	3355.93 ± 45.19
2^3P_1	1^-	4183.58 ± 31.69	4203.79 ± 31.32	3860.55 ± 42.96	3889.69 ± 42.93
3^3P_1	1^-	4448.68 ± 39.95	4476.44 ± 39.43	4204.02 ± 44.50	4237.28 ± 44.21
4^3P_1	1^-	4678.81 ± 49.34	4714.82 ± 48.95	4477.22 ± 63.76	4516.63 ± 63.27
1^3P_2	2^-	3899.42 ± 57.44	3913.56 ± 57.41	3636.87 ± 41.15	3691.71 ± 40.94
2^3P_2	2^-	4225.29 ± 48.09	4245.50 ± 47.97	4046.19 ± 44.38	4086.99 ± 43.88
3^3P_2	2^-	4487.67 ± 60.67	4515.44 ± 60.15	4352.80 ± 43.84	4395.13 ± 43.72
4^3P_2	2^-	4716.28 ± 37.41	4752.28 ± 37.25	4609.05 ± 40.46	4656.36 ± 39.64
1^5P_1	1^-	3802.36 ± 45.86	3815.31 ± 45.74	2692.68 ± 63.51	2726.13 ± 63.00
2^5P_1	1^-	4144.41 ± 42.33	4163.19 ± 42.11	3491.52 ± 61.81	3520.65 ± 61.75
3^5P_1	1^-	4413.06 ± 42.73	4439.23 ± 42.68	3913.91 ± 47.38	3947.16 ± 47.33
4^5P_1	1^-	4644.97 ± 38.49	4679.27 ± 37.79	4224.93 ± 55.17	4264.35 ± 54.63

Continued on next page

Table 3 – continued from previous page

State	J^P	$\bar{\mathbf{3}} - \mathbf{3}$		$\mathbf{6} - \bar{\mathbf{6}}$	
		Semi-Relativistic	Non-Relativistic	Semi-Relativistic	Non-Relativistic
1^5P_2	2^-	3850.72 ± 54.51	3863.67 ± 54.31	3007.07 ± 53.21	3061.91 ± 51.01
2^5P_2	2^-	4186.12 ± 45.86	4204.90 ± 45.57	3677.15 ± 59.48	3717.95 ± 59.24
3^5P_2	2^-	4452.05 ± 52.38	4478.22 ± 51.99	4062.69 ± 48.87	4105.01 ± 48.58
4^5P_2	2^-	4682.44 ± 44.27	4716.74 ± 43.76	4356.77 ± 48.32	4404.07 ± 47.79
1^5P_3	3^-	3961.02 ± 44.76	3973.97 ± 44.55	4267.18 ± 59.59	4300.63 ± 60.26
2^5P_3	3^-	4280.27 ± 43.58	4299.06 ± 43.24	4414.11 ± 53.06	4443.24 ± 53.45
3^5P_3	3^-	4539.47 ± 41.39	4565.64 ± 41.48	4639.19 ± 59.91	4672.45 ± 59.59
4^5P_3	3^-	4766.02 ± 41.05	4800.32 ± 40.59	4855.65 ± 40.03	4895.06 ± 39.91
D-wave states					
1^1D_2	2^+	4098.22 ± 51.53	4114.26 ± 51.31	3816.24 ± 45.67	3848.80 ± 45.35
2^1D_2	2^+	4371.81 ± 44.86	4395.26 ± 44.79	4160.92 ± 57.97	4196.09 ± 57.56
3^1D_2	2^+	4607.94 ± 44.09	4639.51 ± 43.65	4436.70 ± 45.74	4477.35 ± 45.31
4^1D_2	2^+	4820.23 ± 41.01	4860.39 ± 40.72	4675.18 ± 40.21	4722.32 ± 39.74
1^3D_1	1^+	4082.31 ± 38.63	4098.31 ± 38.51	3677.61 ± 56.40	3711.32 ± 55.73
2^3D_1	1^+	4355.94 ± 29.30	4379.29 ± 29.27	4043.23 ± 23.34	4079.84 ± 22.97
3^3D_1	1^+	4592.07 ± 64.33	4623.51 ± 64.00	4328.92 ± 39.66	4371.18 ± 39.15
4^3D_1	1^+	4804.36 ± 53.70	4844.35 ± 53.01	4573.26 ± 55.16	4622.14 ± 54.78
1^3D_2	2^+	4097.11 ± 46.58	4113.11 ± 46.57	3803.42 ± 48.61	3834.84 ± 48.58
2^3D_2	2^+	4370.71 ± 48.16	4394.06 ± 47.88	4154.69 ± 58.46	4188.43 ± 57.81
3^3D_2	2^+	4606.88 ± 42.90	4638.32 ± 42.19	4433.41 ± 61.07	4472.46 ± 60.64
4^3D_2	2^+	4819.22 ± 38.95	4859.22 ± 38.69	4673.53 ± 44.93	4718.96 ± 44.60
1^3D_3	3^+	4106.94 ± 53.02	4122.94 ± 52.85	3884.81 ± 36.75	3917.69 ± 36.66
2^3D_3	3^+	4381.31 ± 48.31	4404.66 ± 48.22	4215.79 ± 44.29	4251.37 ± 44.13
3^3D_3	3^+	4618.00 ± 56.95	4649.44 ± 56.39	4485.24 ± 54.32	4526.34 ± 53.77
4^3D_3	3^+	4830.73 ± 30.76	4870.72 ± 30.45	4720.02 ± 47.69	4767.66 ± 47.47
1^5D_0	0^+	4075.58 ± 55.08	4091.48 ± 54.68	3614.12 ± 48.13	3645.53 ± 47.92
2^5D_0	0^+	4349.03 ± 46.52	4372.21 ± 46.32	3999.82 ± 49.30	4033.56 ± 49.08
3^5D_0	0^+	4585.13 ± 36.49	4616.30 ± 35.91	4294.59 ± 35.59	4333.64 ± 35.09
4^5D_0	0^+	4797.42 ± 23.26	4837.08 ± 22.97	4544.09 ± 53.19	4589.53 ± 52.51
1^5D_1	1^+	4074.32 ± 41.80	4090.23 ± 41.66	3601.88 ± 40.22	3635.59 ± 39.75
2^5D_1	1^+	4348.33 ± 49.34	4371.51 ± 49.39	3981.28 ± 40.79	4017.89 ± 40.30
3^5D_1	1^+	4584.76 ± 36.46	4615.94 ± 36.20	4273.39 ± 47.49	4315.65 ± 47.00
4^5D_1	1^+	4797.30 ± 30.81	4836.95 ± 30.57	4521.49 ± 27.54	4570.36 ± 27.09
1^5D_2	2^+	4089.12 ± 70.14	4105.03 ± 69.78	3727.70 ± 43.43	3759.11 ± 42.92
2^5D_2	2^+	4363.10 ± 44.75	4386.28 ± 44.37	4092.74 ± 44.25	4126.48 ± 44.06
3^5D_2	2^+	4599.58 ± 41.85	4630.75 ± 41.33	4377.89 ± 28.61	4416.93 ± 28.19
4^5D_2	2^+	4812.17 ± 32.58	4851.82 ± 31.88	4621.76 ± 43.16	4667.19 ± 42.96
1^5D_3	3^+	4098.95 ± 33.93	4114.86 ± 33.95	3809.09 ± 34.29	3841.97 ± 34.34
2^5D_3	3^+	4373.70 ± 49.19	4396.88 ± 48.75	4153.85 ± 29.06	4189.42 ± 28.85
3^5D_3	3^+	4610.70 ± 55.89	4641.88 ± 55.38	4429.71 ± 56.38	4470.81 ± 56.19
4^5D_3	3^+	4823.67 ± 30.07	4863.32 ± 29.68	4668.25 ± 43.24	4715.89 ± 42.69
1^5D_4	4^+	4120.72 ± 43.46	4136.63 ± 43.41	3992.73 ± 46.21	4024.14 ± 45.79
2^5D_4	4^+	4395.93 ± 38.12	4419.10 ± 37.75	4309.56 ± 44.49	4343.31 ± 44.24
3^5D_4	4^+	4633.30 ± 62.26	4664.47 ± 61.58	4572.23 ± 45.17	4611.28 ± 44.57
4^5D_4	4^+	4846.57 ± 42.14	4886.22 ± 41.71	4802.96 ± 49.65	4848.40 ± 49.25

Note: The tetraquark states are listed in the unmixed LS -coupling basis. States with the same J^P , such as n^1P_1 , n^3P_1 , and n^5P_1 , may mix in a more complete treatment.

Table 4: Two-meson thresholds relevant to the calculated compact $c\bar{s}\bar{s}$ tetraquark states. The threshold masses are obtained from the present D_s spectrum and the strangeonium-meson inputs of Lodha–Rai [59]; η_s denotes the unmixed hidden-strange pseudoscalar. The mass differences are calculated as $\Delta = M_T - M_{\text{th}}$, using the corresponding ground-state tetraquark mass from Table 3. Positive Δ indicates a tetraquark mass above the threshold. All values are in MeV.

State	Two-meson threshold	Threshold mass		$\mathbf{\bar{3} - \mathbf{3}}$		$\mathbf{6 - \bar{6}}$	
		SR	NR	Δ_{SR}	Δ_{NR}	Δ_{SR}	Δ_{NR}
1S_0	$\eta_s(1S) D_s(1^1S_0)$	2710.88	2764.98	634.53	614.84	853.54	-169.52
3S_1	$\eta_s(1S) D_s^*(1^3S_1)$	2856.06	2890.08	595.14	584.03	708.36	-294.62
	$\phi(1S) D_s(1^1S_0)$	2987.29	3023.50	463.91	450.61	577.13	-428.04
5S_2	$\phi(1S) D_s^*(1^3S_1)$	3132.47	3148.60	523.90	514.10	431.95	-553.14
1P_1	$\eta_s(1S) D_s(1^1P_1)$	3217.86	3256.87	644.94	620.70	156.86	168.95
	$D_s(1^1S_0) h_1(1P)$	3400.22	3439.65	462.58	437.92	-25.50	-13.83
3P_0	$\eta_s(1S) D_s^*(1^3P_0)$	3125.76	3163.75	655.80	631.96	-909.46	-857.77
	$D_s(1^1S_0) f_0(1P)$	3221.52	3251.09	560.04	544.62	-1005.22	-945.11
3P_1	$\eta_s(1S) D_{s1}(1^3P_1)$	3208.99	3246.99	642.07	618.22	113.49	108.94
	$D_s(1^1S_0) f_1(1P)$	3422.00	3461.32	429.06	403.89	-99.52	-105.39
3P_2	$\eta_s(1S) D_{s2}^*(1^3P_2)$	3255.03	3293.02	644.39	620.54	381.84	398.69
	$D_s(1^1S_0) f_2'(1P)$	3454.44	3495.71	444.98	417.85	182.43	196.00
5P_1	$\phi(1S) D_s^*(1^3P_0)$	3402.16	3422.27	400.20	393.04	-709.48	-696.14
	$D_s^*(1^3S_1) f_0(1P)$	3366.70	3376.19	435.66	439.12	-674.02	-650.06
5P_2	$\phi(1S) D_{s1}(1^3P_1)$	3485.40	3505.51	365.32	358.16	-478.33	-443.60
	$D_s^*(1^3S_1) f_1(1P)$	3567.18	3586.42	283.54	277.25	-560.11	-524.51
5P_3	$\phi(1S) D_{s2}^*(1^3P_2)$	3531.44	3551.54	429.58	422.43	735.74	749.09
	$D_s^*(1^3S_1) f_2'(1P)$	3599.62	3620.81	361.40	353.16	667.56	679.82
1D_2	$\eta_s(1S) D_{s2}(1^1D_2)$	3480.05	3526.46	618.17	587.80	336.19	322.34
	$D_s(1^1S_0) \eta_2(1D)$	3804.29	3872.19	293.93	242.07	11.95	-23.39
3D_1	$\eta_s(1S) D_{s1}^*(1^3D_1)$	3472.38	3518.73	609.93	579.58	205.23	192.59
	$D_s(1^1S_0) \phi_1(1D)$	3784.72	3851.78	297.59	246.53	-107.11	-140.46
3D_2	$\eta_s(1S) D_{s2}^*(1^3D_2)$	3483.72	3530.07	613.39	583.04	319.70	304.77
	$D_s(1^1S_0) \phi_2(1D)$	3809.40	3878.15	287.71	234.96	-5.98	-43.31
3D_3	$\eta_s(1S) D_{s3}^*(1^3D_3)$	3481.53	3527.88	625.41	595.06	403.28	389.81
	$D_s(1^1S_0) \phi_3(1D)$	3764.90	3867.91	342.04	255.03	119.91	49.78
5D_0	$\phi(1S) D_{s1}^*(1^3D_1)$	3748.79	3777.25	326.79	314.23	-134.67	-131.72
	$D_s^*(1^3S_1) \phi_1(1D)$	3929.90	3976.88	145.68	114.60	-315.78	-331.35
5D_1	$f_0(1P) D_{s1}^*(1^3D_1)$	3983.02	4004.84	91.30	85.39	-381.14	-369.25
	$D_{s1}(1^3P_1) \phi_1(1D)$	4282.83	4333.79	-208.51	-243.56	-680.95	-698.20
5D_2	$\phi(1S) D_{s1}^*(1^3D_1)$	3748.79	3777.25	340.33	327.78	-21.09	-18.14
	$D_s^*(1^3S_1) \phi_1(1D)$	3929.90	3976.88	159.22	128.15	-202.20	-217.77
5D_3	$\phi(1S) D_{s2}^*(1^3D_2)$	3760.13	3788.60	338.82	326.26	48.96	53.37
	$D_s^*(1^3S_1) \phi_2(1D)$	3954.58	4003.25	144.37	111.61	-145.49	-161.28
5D_4	$\phi(1S) D_{s3}^*(1^3D_3)$	3757.94	3786.40	362.78	350.23	234.79	237.74
	$D_s^*(1^3S_1) \phi_3(1D)$	3910.08	3993.01	210.64	143.62	82.65	31.13

4 Regge trajectories

Regge trajectories provide a useful framework for organizing hadron spectra by relating a state's orbital or radial quantum number to its squared mass. This approach follows the original Regge-pole and Chew–Frautschi ideas and their later spectroscopic applications [60–64]. In recent phenomenological studies, Oudichhya and collaborators have applied the same quasi-linear Regge-systematics program to kaon and strangeonium mesons, open-charm D mesons, singly charmed baryons, and singly bottom or doubly heavy baryons [65–68]. In the present work, the orbital trajectories are characterized through the approximate linear relation in the (L, M^2) plane

$$L = \alpha M^2 + \alpha_0, \quad (14)$$

while the radial trajectories are described through

$$n = \beta M^2 + \beta_0. \quad (15)$$

Here, α and β denote the orbital and radial slopes, respectively. For heavy-light systems such as the D_s mesons and for compact $c\bar{s}\bar{s}$ tetraquarks, deviations from strict linearity can arise from spin-dependent interactions, unequal constituent masses, and the internal structure of the diquark–antidiquark configuration. Nevertheless, approximately linear trajectories continue to provide a compact diagnostic of the spectroscopy and allow useful comparisons between the semi-relativistic and non-relativistic descriptions.

The extracted orbital and radial slopes are summarized separately for the calculated D_s meson family and the $c\bar{s}\bar{s}$ tetraquark sector in Tables 5 and 6, respectively. In the tetraquark table, the shorthand configurations “3-3” and “6-6” denote the $\bar{\mathbf{3}} - \mathbf{3}$ and $\mathbf{6} - \bar{\mathbf{6}}$ color couplings. The same table also includes the tetraquark-to-meson slope ratios for both orbital and radial trajectories wherever a corresponding meson trajectory is available.

Table 5: Regge-trajectory slopes for the D_s meson family obtained from linear fits in the (L, M^2) and (n, M^2) planes, following standard Regge phenomenology [60, 61, 63, 64] and recent meson applications [65, 66]. For orbital trajectories the fixed quantity is the radial quantum number n , while for radial trajectories the fixed quantity is the orbital angular momentum L . All numerical fit values are rounded to four significant figures.

Trajectory	Spin	Fixed	Slope _{SR}	Slope _{NR}	R ratio
Orbital	0	n=0	0.6165	0.6088	1.013
Orbital	0	n=1	0.7347	0.7145	1.028
Orbital	0	n=2	0.7630	0.7577	1.007
Orbital	0	n=3	0.7382	0.7800	0.9463
Orbital	1	n=0	0.7077	0.6817	1.038
Orbital	1	n=1	0.7833	0.7509	1.043
Orbital	1	n=2	0.7840	0.7779	1.008
Orbital	1	n=3	0.7328	0.7889	0.9290
Radial	0	L=0	0.4296	0.4197	1.024
Radial	0	L=1	0.4854	0.4700	1.033
Radial	0	L=2	0.4900	0.4836	1.013
Radial	0	L=3	0.4795	0.4911	0.9764
Radial	1	L=0	0.4514	0.4339	1.040
Radial	1	L=1	0.4794	0.4633	1.035
Radial	1	L=2	0.4909	0.4842	1.014
Radial	1	L=3	0.4800	0.4916	0.9764

Table 6: Regge-trajectory slopes for the $cs\bar{s}\bar{s}$ tetraquark sector obtained from linear fits in the (L, M^2) and (n, M^2) planes [60, 61, 63, 64]. The two color configurations are displayed side by side; “3-3” and “6-6” denote the $\bar{\mathbf{3}} - \mathbf{3}$ and $\mathbf{6} - \bar{\mathbf{6}}$ color couplings, respectively. For orbital trajectories the fixed quantity is n , while for radial trajectories the fixed quantity is L . The columns SR/M and NR/M give the tetraquark-to-meson slope ratios computed from the corresponding mesonic slopes in Table 5; spin-2 ratios are left blank because no spin-2 meson trajectory is available. All numerical fit values are rounded to four significant figures.

Spin	Fixed	$\bar{\mathbf{3}} - \mathbf{3}$					$\mathbf{6} - \bar{\mathbf{6}}$				
		SR	NR	R	SR/M	NR/M	SR	NR	R	SR/M	NR/M
Orbital trajectories											
0	$n = 0$	0.3443	0.3519	0.9785	0.5585	0.5780	0.3652	0.2430	1.503	0.5923	0.3992
0	$n = 1$	0.5439	0.5401	1.007	0.7403	0.7560	0.3518	0.3590	0.9799	0.4789	0.5025
0	$n = 2$	0.6484	0.6373	1.017	0.8498	0.8411	0.4771	0.4760	1.002	0.6253	0.6283
0	$n = 3$	0.7187	0.7012	1.025	0.9737	0.8989	0.5588	0.5515	1.013	0.7570	0.7071
1	$n = 0$	0.4145	0.4162	0.9959	0.5857	0.6105	0.08594	0.1464	0.5872	0.1214	0.2147
1	$n = 1$	0.5783	0.5690	1.016	0.7383	0.7577	0.1990	0.2017	0.9863	0.2540	0.2686
1	$n = 2$	0.6624	0.6462	1.025	0.8449	0.8307	0.2271	0.2305	0.9850	0.2897	0.2964
1	$n = 3$	0.7162	0.6944	1.031	0.9773	0.8802	0.2415	0.2456	0.9832	0.3295	0.3114
2	$n = 0$	0.5458	0.5352	1.020	–	–	0.06179	0.1130	0.5468	–	–
2	$n = 1$	0.6589	0.6401	1.029	–	–	0.1673	0.1668	1.003	–	–
2	$n = 2$	0.7321	0.7063	1.036	–	–	0.1881	0.1880	1.000	–	–
2	$n = 3$	0.7769	0.7458	1.042	–	–	0.1956	0.1962	0.9970	–	–
Radial trajectories											
0	$L = 0$	0.3207	0.3184	1.007	0.7465	0.7586	0.3902	0.2472	1.579	0.9083	0.5890
0	$L = 1$	0.4259	0.4124	1.033	0.8774	0.8774	0.3360	0.3339	1.006	0.6922	0.7104
0	$L = 2$	0.4659	0.4481	1.040	0.9508	0.9266	0.4112	0.4006	1.026	0.8392	0.8284
1	$L = 0$	0.3420	0.3370	1.015	0.7576	0.7767	0.3902	0.2472	1.579	0.8644	0.5697
1	$L = 1$	0.4169	0.4043	1.031	0.8696	0.8727	0.2007	0.2021	0.9930	0.4186	0.4362
1	$L = 2$	0.4651	0.4474	1.039	0.9474	0.9240	0.3912	0.3820	1.024	0.7969	0.7889
2	$L = 0$	0.3934	0.3827	1.028	–	–	0.3902	0.2472	1.579	–	–
2	$L = 1$	0.4096	0.3979	1.029	–	–	0.1630	0.1625	1.003	–	–
2	$L = 2$	0.4634	0.4461	1.039	–	–	0.3591	0.3518	1.021	–	–

The ratios in Tables 5 and 6 provide a useful internal check on the calculated spectra. For the D_s mesons, the semi-relativistic to non-relativistic slope ratios remain close to unity for both orbital and radial trajectories, showing that the fitted meson slopes are not strongly altered by the treatment of relativistic corrections. In the tetraquark sector, the $\bar{\mathbf{3}} - \mathbf{3}$ orbital slopes for the lowest $n = 0$ trajectories are smaller than the corresponding mesonic slopes, while the ratios move closer to the meson values for higher radial excitations. The radial tetraquark-to-meson ratios are generally larger than the lowest orbital ratios, indicating that radial excitation patterns of the compact $[cs][\bar{s}\bar{s}]$ system remain more meson-like than the orbital excitation patterns. By contrast, several $\mathbf{6} - \bar{\mathbf{6}}$ entries show a stronger spread in the SR/NR and tetraquark-to-meson ratios, especially for the lowest orbital trajectories, which reflects the greater sensitivity of this color configuration to the repulsive internal diquark channel and to nearby two-meson thresholds.

Representative orbital and radial Regge plots corresponding to the fitted slopes are displayed in Figs. 1

and 2 for the D_s meson family, in Figs. 3 and 4 for the $\bar{\mathbf{3}} - \mathbf{3}$ tetraquark configuration, and in Figs. 5 and 6 for the $\mathbf{6} - \bar{\mathbf{6}}$ configuration. In each case the non-relativistic and semi-relativistic trajectories are shown separately for the available total-spin assignments.

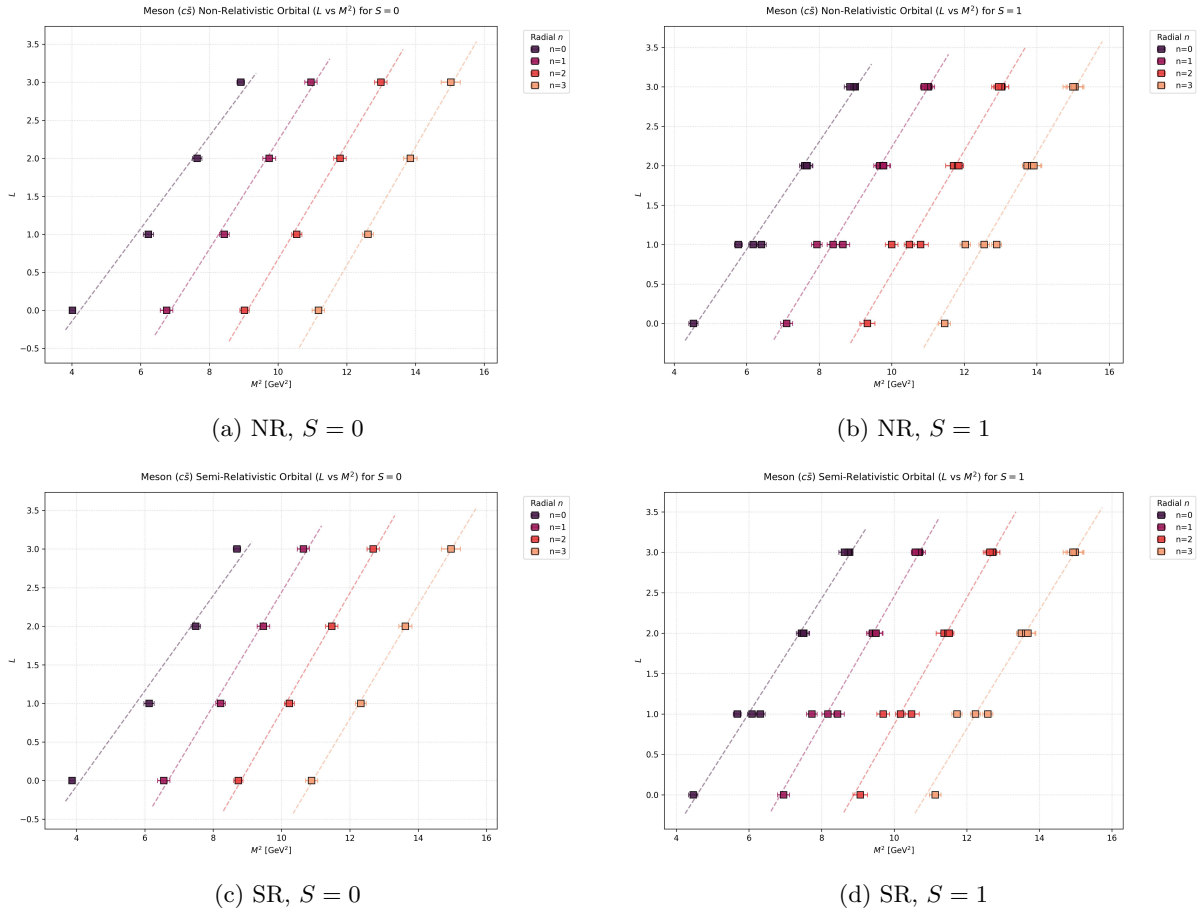


Figure 1: Orbital Regge trajectories in the (L, M^2) plane for the D_s meson family in the non-relativistic and semi-relativistic schemes for $S = 0$ and $S = 1$.

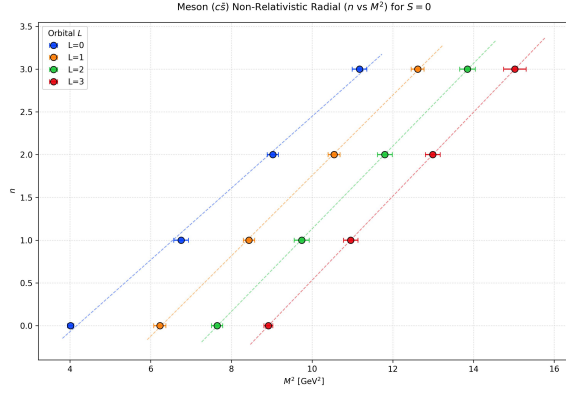
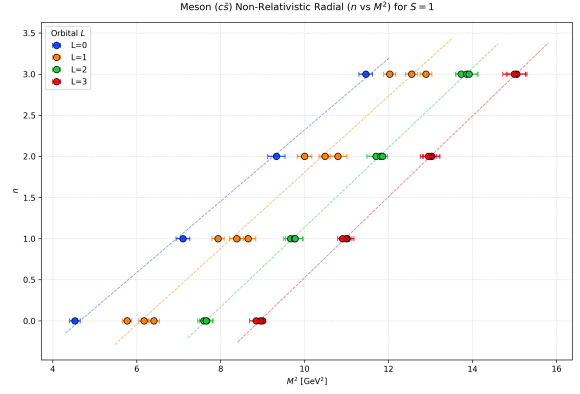
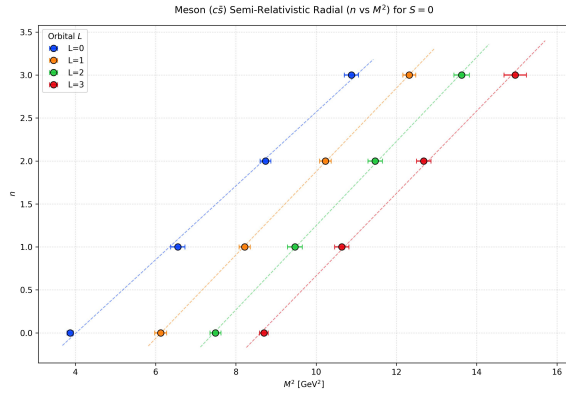
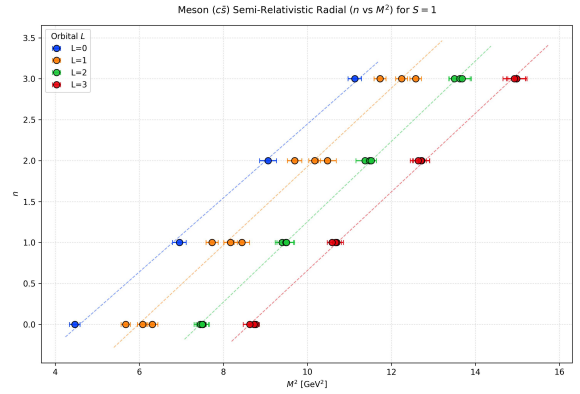
(a) NR, $S = 0$ (b) NR, $S = 1$ (c) SR, $S = 0$ (d) SR, $S = 1$

Figure 2: Radial Regge trajectories in the (n, M^2) plane for the D_s meson family in the non-relativistic and semi-relativistic schemes for $S = 0$ and $S = 1$.

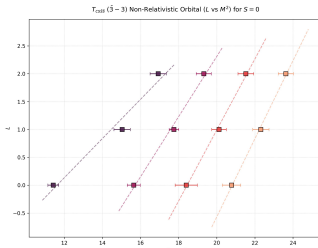
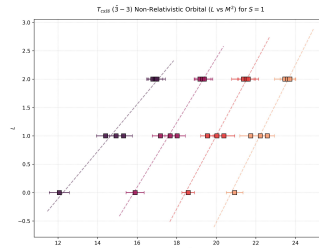
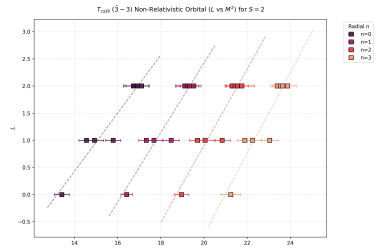
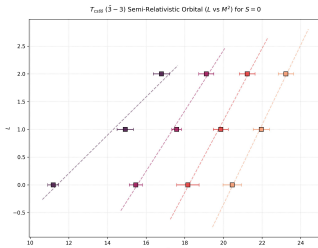
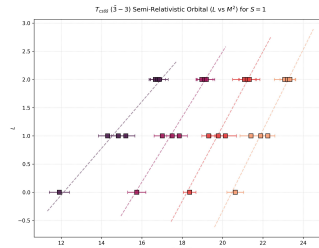
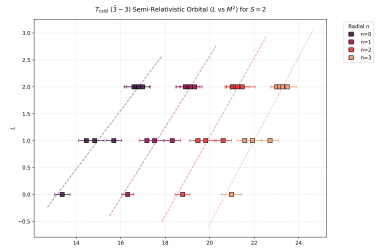
(a) NR, $S = 0$ (b) NR, $S = 1$ (c) NR, $S = 2$ (d) SR, $S = 0$ (e) SR, $S = 1$ (f) SR, $S = 2$

Figure 3: Orbital Regge trajectories in the (L, M^2) plane for the $T_{c\bar{s}\bar{s}\bar{s}}$ tetraquark in the $\bar{\mathbf{3}}-\mathbf{3}$ configuration. The first row shows the non-relativistic results and the second row shows the semi-relativistic results for $S = 0, 1, 2$.

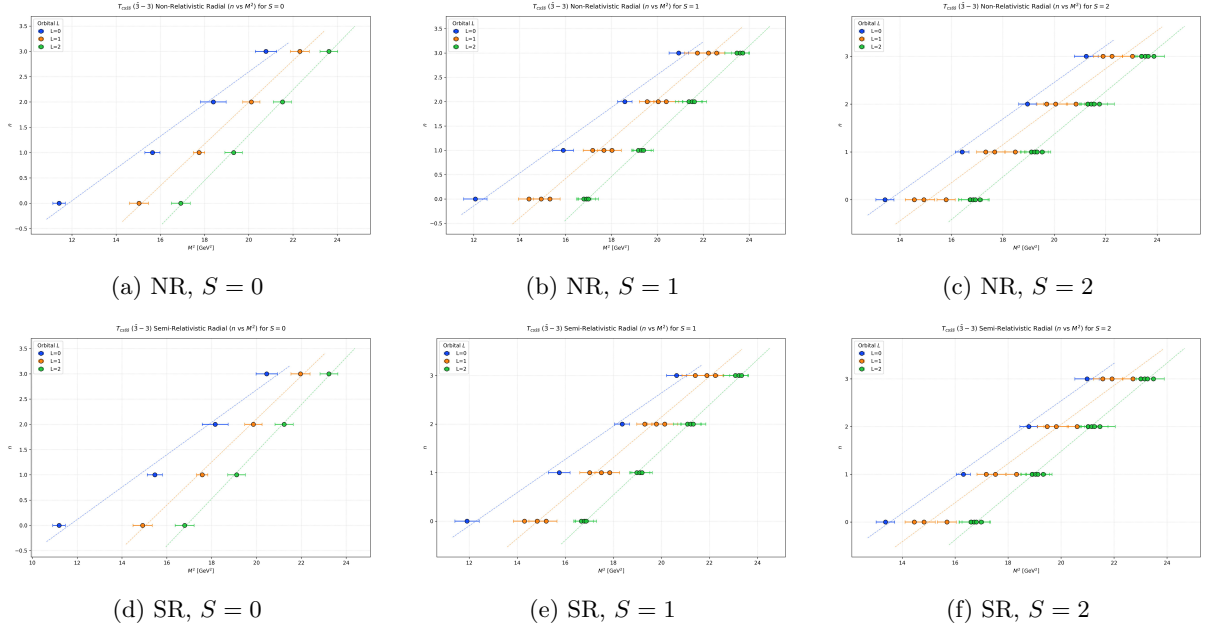


Figure 4: Radial Regge trajectories in the (n, M^2) plane for the $T_{CS\bar{s}\bar{s}}$ tetraquark in the $\bar{\mathbf{3}}-\mathbf{3}$ configuration. The first row shows the non-relativistic results and the second row shows the semi-relativistic results for $S = 0, 1, 2$.

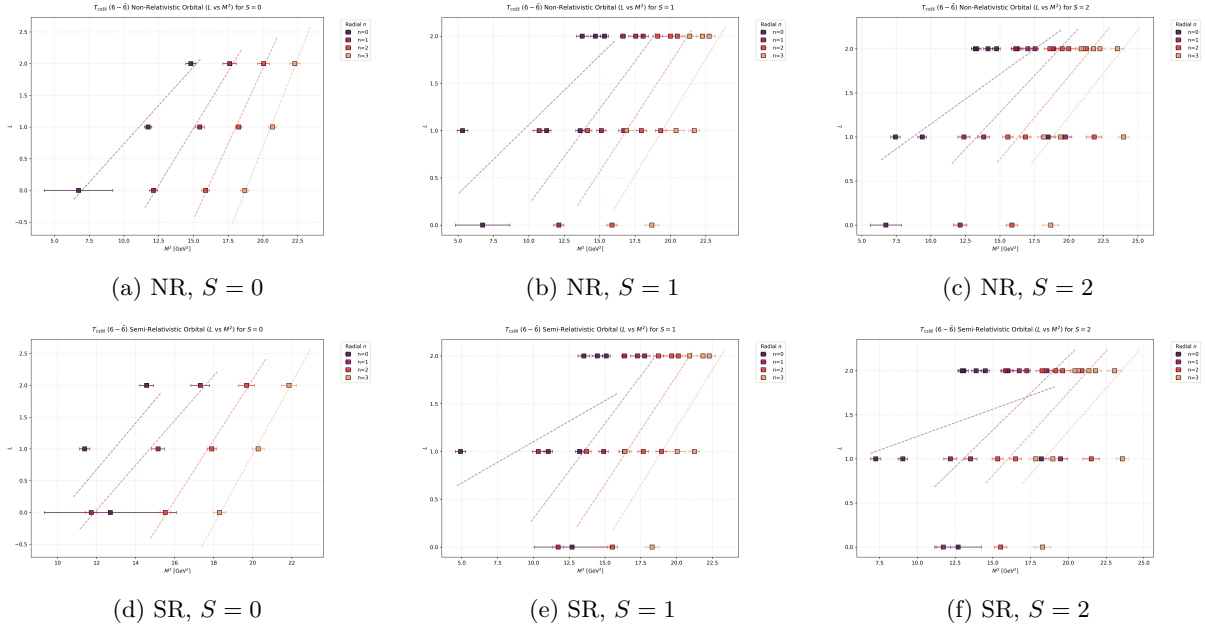


Figure 5: Orbital Regge trajectories in the (L, M^2) plane for the $T_{CS\bar{s}\bar{s}}$ tetraquark in the $\mathbf{6}-\bar{\mathbf{6}}$ configuration. The first row shows the non-relativistic results and the second row shows the semi-relativistic results for $S = 0, 1, 2$.

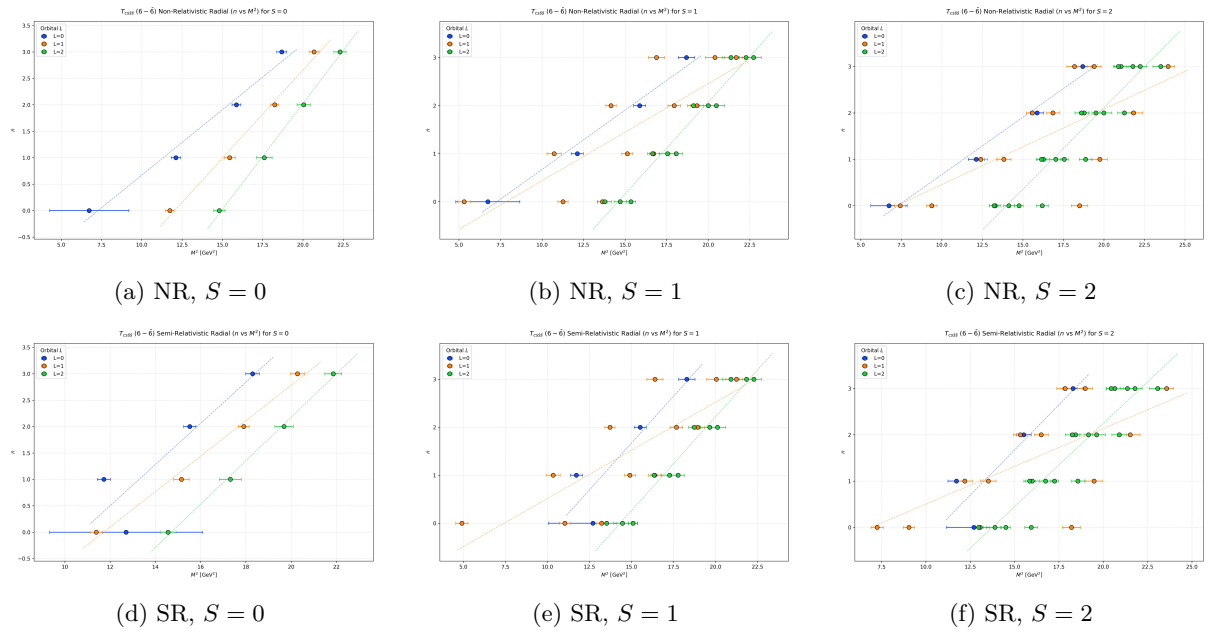


Figure 6: Radial Regge trajectories in the (n, M^2) plane for the $T_{CS\bar{S}\bar{S}}$ tetraquark in the $\mathbf{6}-\bar{\mathbf{6}}$ configuration. The first row shows the non-relativistic results and the second row shows the semi-relativistic results for $S = 0, 1, 2$.

5 Decay

A fundamental property accompanying the mass spectrum of a bound state is its decay width, which provides important information about its stability, internal structure, and dominant interaction mechanism [3, 12]. In the present charm–strange study, the mesonic decay sector contains both open-charm D_s mesons and hidden-strange $s\bar{s}$ mesons that appear among the two-meson thresholds relevant to the rearrangement decays of the compact $cs\bar{s}\bar{s}$ tetraquarks. Accordingly, we discuss benchmark hidden-strange $\phi(1020)$ decays in a local QCD-sum-rule framework, weak D_s decays through QCD-sum-rule-based form factors together with the factorization approximation for selected two-body nonleptonic modes, and compact tetraquark strong decays through direct two-point and three-point QCD sum rules [33–35, 69]. For the $J^P = 0^+, 1^+, 2^+$ $cs\bar{s}\bar{s}$ multiplet, the two-point correlators determine the masses and pole residues, while the three-point correlators determine the channel-dependent hadronic couplings entering the partial widths. This combined treatment links the calculated spectroscopy directly to experimentally accessible decay channels, Fierz-rearranged fall-apart topologies [70], and to the thresholds listed in Table 4.

5.1 Meson Decay

The meson-decay sector considered in the present work has two complementary components. The open-charm part is represented by the weak decays of the D_s family, while the hidden-strange part is represented by benchmark decays of the $\phi(1020)$ meson, which provides a useful $s\bar{s}$ reference for the strangeonium states entering the tetraquark thresholds.

5.1.1 Hidden-strange $s\bar{s}$ meson decay

Besides the weak decays of the open-charm D_s mesons, the present charm–strange system also involves hidden-strange $s\bar{s}$ mesons because they appear among the lowest two-meson thresholds relevant to the rearrangement decays of the compact $cs\bar{s}\bar{s}$ tetraquarks. Among these channels, the $\phi(1020)$ provides the cleanest benchmark for an $s\bar{s}$ decay analysis. Its leptonic, strong, and radiative decays are conveniently described within a local two-point and three-point QCD-sum-rule framework using the currents [71–74]

$$j_\mu^\phi = \bar{s}\gamma_\mu s, \quad j_5^s = \bar{s}i\gamma_5 s, \quad J_s = \bar{s}s, \quad j_5^K = \bar{q}i\gamma_5 s, \quad (16)$$

with the matrix-element definitions

$$\langle 0|j_\mu^\phi|\phi(q, \epsilon)\rangle = f_\phi m_\phi \epsilon_\mu, \quad \langle 0|j_5^s|\eta\rangle = A, \quad \langle 0|j_5^s|\eta'\rangle = A', \quad \langle 0|J_s|f_0\rangle = m_{f_0} \tilde{f}_{f_0}. \quad (17)$$

The benchmark two-point QCD-sum-rule inputs adopted in the present decay analysis are

$$m_\phi = 1.023 \pm 0.013 \text{ GeV}, \quad f_\phi = 0.240 \pm 0.005 \text{ GeV}, \quad (18)$$

$$A = 0.115 \pm 0.004 \text{ GeV}^2, \quad A' = 0.153 \pm 0.011 \text{ GeV}^2, \quad \tilde{f}_{f_0} = 0.180 \pm 0.015 \text{ GeV}. \quad (19)$$

For the strong and radiative channels we use the benchmark couplings

$$\langle K(p)\bar{K}(p')|\phi(q, \epsilon)\rangle = g_{\phi KK}(q^2) \epsilon \cdot (p - p'), \quad g_{\phi KK} = 4.82 \pm 1.30, \quad (20)$$

$$\begin{aligned} g_{\phi\eta\gamma} &= 0.64 \pm 0.06 \text{ GeV}^{-1}, & g_{\phi\eta'\gamma} &= 0.98 \pm 0.20 \text{ GeV}^{-1}, \\ g_{\phi\pi\gamma} &= 0.125 \pm 0.004, & F_1^{\phi f_0}(0) &= 0.34 \pm 0.07 \text{ GeV}^{-1}. \end{aligned} \quad (21)$$

The corresponding benchmark widths are evaluated from

$$\Gamma(\phi \rightarrow \ell^+ \ell^-) = \frac{4\pi\alpha_{\text{em}}^2 Q_s^2}{3m_\phi} f_\phi^2 \left(1 + \frac{2m_\ell^2}{m_\phi^2}\right) \sqrt{1 - \frac{4m_\ell^2}{m_\phi^2}}, \quad Q_s = -\frac{1}{3}, \quad (22)$$

$$\Gamma(\phi \rightarrow K \bar{K}) = \frac{g_{\phi KK}^2}{6\pi m_\phi^2} |\vec{p}_K|^3, \quad |\vec{p}_K| = \frac{\lambda^{1/2}(m_\phi^2, m_K^2, m_{\bar{K}}^2)}{2m_\phi}, \quad (23)$$

$$\Gamma(\phi \rightarrow P\gamma) = \frac{\alpha_{\text{em}} g_{\phi P\gamma}^2}{24} \left(\frac{m_\phi^2 - m_P^2}{m_\phi}\right)^3, \quad P = \eta, \eta', \quad (24)$$

and

$$\Gamma(\phi \rightarrow f_0\gamma) = \frac{\alpha_{\text{em}} [F_1^{\phi f_0}(0)]^2 (m_\phi^2 - m_{f_0}^2)(m_\phi^2 + m_{f_0}^2)^2}{216m_\phi^3}. \quad (25)$$

The resulting benchmark decay widths and branching fractions are summarized in Table 7. These hidden-strange channels are directly relevant to the present tetraquark study because the ϕ , η , η' , and $f_0(980)$ states appear among the natural $s\bar{s}$ products of the rearrangement decays of the compact $cs\bar{s}$ system.

Table 7: Comparison of the present benchmark partial widths for hidden-strange $\phi(1020)$ decays with the PDG 2024 branching fractions and the corresponding PDG partial widths [3]. The PDG partial widths are obtained from $\Gamma_\phi^{\text{PDG}} = 4.249 \pm 0.013$ MeV multiplied by the listed PDG branching fractions.

Mode	Present width	Present branching fraction	PDG branching fraction	PDG partial width
$\phi \rightarrow e^+ e^-$	1.40 ± 0.06 keV	$(3.29 \pm 0.14) \times 10^{-4}$	$(2.979 \pm 0.033) \times 10^{-4}$	1.266 ± 0.015 keV
$\phi \rightarrow \mu^+ \mu^-$	1.40 ± 0.06 keV	$(3.29 \pm 0.14) \times 10^{-4}$	$(2.85 \pm 0.22) \times 10^{-4}$	1.211 ± 0.094 keV
$\phi \rightarrow K^+ K^-$	2.42 ± 1.31 MeV	0.570 ± 0.308	0.491 ± 0.005	2.086 ± 0.022 MeV
$\phi \rightarrow K^0 \bar{K}^0$	1.60 ± 0.86 MeV	0.377 ± 0.202	0.339 ± 0.004	1.440 ± 0.018 MeV
$\phi \rightarrow \eta\gamma$	47.5 ± 8.9 keV	$(1.13 \pm 0.21) \times 10^{-2}$	$(1.301 \pm 0.024) \times 10^{-2}$	55.28 ± 1.03 keV
$\phi \rightarrow \eta'\gamma$	0.50 ± 0.21 keV	$(1.18 \pm 0.49) \times 10^{-4}$	$(6.21 \pm 0.20) \times 10^{-5}$	0.264 ± 0.009 keV
$\phi \rightarrow \pi^0\gamma$	4.59 ± 0.29 keV	$(1.08 \pm 0.07) \times 10^{-3}$	$(1.32 \pm 0.05) \times 10^{-3}$	5.61 ± 0.21 keV
$\phi \rightarrow f_0(980)\gamma$	1.16 ± 0.48 keV	$(2.73 \pm 1.13) \times 10^{-4}$	$(3.22 \pm 0.19) \times 10^{-4}$	1.37 ± 0.08 keV

5.1.2 Weak decays of the D_s meson

The charged D_s^+ meson supports three main weak topologies,

$$c \rightarrow s, d, \quad \bar{s} \text{ spectator}, \quad (26)$$

$$c\bar{s} \rightarrow W^+, \quad \text{weak annihilation}, \quad (27)$$

$$\bar{s} \rightarrow \bar{u}, \quad c \text{ spectator}, \quad (28)$$

with the first class generating the dominant semileptonic channels $D_s^+ \rightarrow \eta \ell^+ \nu_\ell$, $D_s^+ \rightarrow \eta' \ell^+ \nu_\ell$, and $D_s^+ \rightarrow \phi \ell^+ \nu_\ell$, while the spectator- c sector contains the kinematically suppressed transition $D_s^+ \rightarrow D^0 e^+ \nu_e$. For semileptonic charm-changing processes we employ the effective Hamiltonian

$$\mathcal{H}_{\text{eff}}^{c \rightarrow q} = \frac{G_F}{\sqrt{2}} V_{cq}^* [\bar{q}\gamma_\mu(1 - \gamma_5)c] [\bar{\nu}_\ell\gamma^\mu(1 - \gamma_5)\ell], \quad q = s, d, \quad (29)$$

while the spectator- c transition is described through the weak current

$$J_\mu^{\bar{s} \rightarrow \bar{u}} = \bar{s}\gamma_\mu(1 - \gamma_5)u, \quad (30)$$

with CKM factor V_{us} . For factorized two-body nonleptonic channels we use the tree-level Hamiltonian

$$H_{\text{eff}} = \frac{G_F}{\sqrt{2}} V_{cq_1}^* V_{uq_2} [c_1(\mu)(\bar{q}_{1\alpha} c_\alpha)_{V-A} (\bar{u}_\beta q_{2\beta})_{V-A} + c_2(\mu)(\bar{q}_{1\alpha} c_\beta)_{V-A} (\bar{u}_\beta q_{2\alpha})_{V-A}], \quad (31)$$

with

$$a_1 = c_1 + \frac{c_2}{N_c}. \quad (32)$$

In the numerical benchmarks below we take $c_1 = 1.26$, $c_2 = -0.51$, and $N_c = 3$, so that $a_1 = 1.09$ [75].

The mesonic transition form factors are defined through local three-point QCD sum rules. For a generic transition $D_s \rightarrow X$, the correlator is written as

$$\Pi_{\{\mu\dots\}}(p, p') = i^2 \int d^4x d^4y e^{ip'\cdot x} e^{i(p-p')\cdot y} \langle 0 | T \{ J_X(x) J_W(y) J_{D_s}^\dagger(0) \} | 0 \rangle, \quad (33)$$

with

$$q = p - p', \quad P = p + p', \quad Q^2 = -q^2 > 0, \quad (34)$$

and the interpolating current for the initial meson chosen as

$$J_{D_s} = \bar{s} i \gamma_5 c. \quad (35)$$

For the final state we use

$$J_P = \bar{q} i \gamma_5 s, \quad J_\nu^V = \bar{q} \gamma_\nu s, \quad J_S = \bar{q} s, \quad J_D = \bar{u} i \gamma_5 c. \quad (36)$$

The corresponding hadronic normalizations are

$$\langle 0 | \bar{s} i \gamma_5 c | D_s(p) \rangle = \frac{f_{D_s} m_{D_s}^2}{m_c + m_s}, \quad (37)$$

$$\langle 0 | \bar{q} i \gamma_5 s | P(p') \rangle = \frac{f_P m_P^2}{m_q + m_s}, \quad \langle 0 | \bar{q} \gamma_\nu s | V(p', \varepsilon) \rangle = f_V m_V \varepsilon_\nu, \quad (38)$$

$$\langle 0 | J_S | S \rangle = \lambda_S, \quad \langle 0 | \bar{u} i \gamma_5 c | D^0(p') \rangle = \frac{f_D m_D^2}{m_c + m_u}. \quad (39)$$

For a pseudoscalar final state,

$$\langle P(p') | \bar{q}_2 \gamma_\mu q_1 | D_s(p) \rangle = f_+(q^2) P_\mu + f_-(q^2) q_\mu, \quad (40)$$

with scalar form factor

$$f_0(q^2) = f_+(q^2) + \frac{q^2}{m_{D_s}^2 - m_P^2} f_-(q^2), \quad f_0(0) = f_+(0). \quad (41)$$

For a vector final state,

$$\langle V(p', \varepsilon) | \bar{q} \gamma_\mu c | D_s(p) \rangle = \frac{2iV(q^2)}{m_{D_s} + m_V} \epsilon_{\mu\nu\alpha\beta} \varepsilon^{*\nu} p^\alpha p'^\beta, \quad (42)$$

$$\begin{aligned} \langle V(p', \varepsilon) | \bar{q} \gamma_\mu \gamma_5 c | D_s(p) \rangle &= (m_{D_s} + m_V) A_1(q^2) \left[\varepsilon_\mu^* - \frac{\varepsilon^* \cdot q}{q^2} q_\mu \right] \\ &\quad - A_2(q^2) \frac{\varepsilon^* \cdot q}{m_{D_s} + m_V} \left[P_\mu - \frac{m_{D_s}^2 - m_V^2}{q^2} q_\mu \right] \\ &\quad + 2m_V A_0(q^2) \frac{\varepsilon^* \cdot q}{q^2} q_\mu, \end{aligned} \quad (43)$$

subject to

$$A_0(0) = A_3(0), \quad A_3(q^2) = \frac{m_{D_s} + m_V}{2m_V} A_1(q^2) - \frac{m_{D_s} - m_V}{2m_V} A_2(q^2). \quad (44)$$

For scalar final states we identify

$$F_1(q^2) = f_+(q^2), \quad F_0(q^2) = f_+(q^2) + \frac{q^2}{m_{D_s}^2 - m_S^2} f_-(q^2). \quad (45)$$

In the present analysis, the $D_s \rightarrow \phi$ channel is taken as the reference local three-point-QCDSR benchmark, for which we use $V^{D_s \rightarrow \phi}(0) = 1.21$, $A_0^{D_s \rightarrow \phi}(0) = 0.42$, $A_1^{D_s \rightarrow \phi}(0) = 0.55$, and $A_2^{D_s \rightarrow \phi}(0) = 0.59$ [76]. For the channels $D_s \rightarrow \eta$, $D_s \rightarrow \eta'$, and $D_s \rightarrow f_0(980)$, we retain the benchmark values

$$f_+^{D_s \rightarrow \eta}(0) = 0.495, \quad f_+^{D_s \rightarrow \eta'}(0) = 0.558, \quad F_1^{D_s \rightarrow f_0}(0) = 0.516, \quad (46)$$

as phenomenological inputs pending a fully uniform local three-point implementation. Whenever a channel-specific q^2 profile is not available, a simple pole continuation is adopted,

$$F(q^2) = \frac{F(0)}{1 - q^2/m_{\text{pole}}^2}. \quad (47)$$

5.1.3 Form-factor profiles

For compact presentation, the semi-relativistic form-factor behavior is summarized through comparison plots between the corrected and uncorrected channels, as shown in Fig. 7. These panels provide a family-wise view of the changes induced by the corrected implementation and are used as the reference graphical input for the semileptonic, spectator- c , and factorized nonleptonic D_s decay analysis.

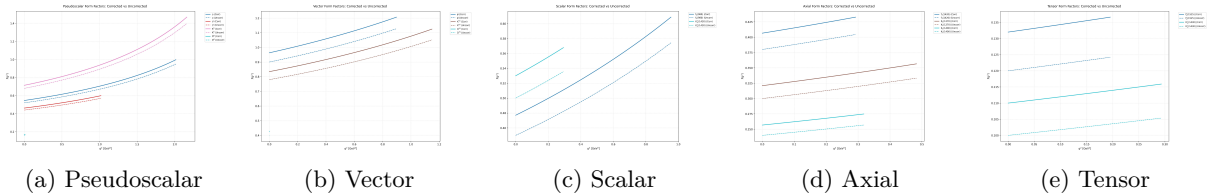


Figure 7: Semi-relativistic form-factor comparison plots for the pseudoscalar, vector, scalar, axial-vector, and tensor D_s decay channels.

The purely leptonic width is given by

$$\Gamma(D_s^+ \rightarrow \ell^+ \nu_\ell) = \frac{G_F^2}{8\pi} |V_{cs}|^2 f_{D_s}^2 m_\ell^2 m_{D_s} \left(1 - \frac{m_\ell^2}{m_{D_s}^2} \right)^2. \quad (48)$$

For semileptonic decays into pseudoscalar or scalar final states,

$$|\mathbf{p}_X(q^2)| = \frac{\lambda^{1/2}(m_{D_s}^2, m_X^2, q^2)}{2m_{D_s}}, \quad X = P, S, \quad (49)$$

with differential widths

$$\frac{d\Gamma(D_s \rightarrow P\ell\nu)}{dq^2} = \frac{G_F^2 |V_{cq}|^2}{24\pi^3} |\mathbf{p}_P(q^2)|^3 |f_+(q^2)|^2, \quad (50)$$

$$\frac{d\Gamma(D_s \rightarrow S\ell\nu)}{dq^2} = \frac{G_F^2 |V_{cq}|^2}{24\pi^3} |\mathbf{p}_S(q^2)|^3 |F_1(q^2)|^2. \quad (51)$$

For vector final states,

$$H_{\pm}(q^2) = (m_{D_s} + m_V)A_1(q^2) \mp \frac{2m_{D_s}|\mathbf{p}_V|}{m_{D_s} + m_V} V(q^2), \quad (52)$$

$$H_0(q^2) = \frac{1}{2m_V\sqrt{q^2}} \left[(m_{D_s}^2 - m_V^2 - q^2)(m_{D_s} + m_V)A_1(q^2) - \frac{4m_{D_s}^2|\mathbf{p}_V|^2}{m_{D_s} + m_V} A_2(q^2) \right], \quad (53)$$

so that

$$\frac{d\Gamma(D_s \rightarrow V\ell\nu)}{dq^2} = \frac{G_F^2 |V_{cq}|^2}{96\pi^3 m_{D_s}^2} q^2 |\mathbf{p}_V(q^2)| (|H_+|^2 + |H_-|^2 + |H_0|^2). \quad (54)$$

The integrated width and branching fraction are then

$$\Gamma = \int_{m_\ell^2}^{(m_{D_s} - m_X)^2} \frac{d\Gamma}{dq^2} dq^2, \quad \mathcal{B} = \Gamma\tau_{D_s}. \quad (55)$$

The corresponding semi-relativistic differential-width profiles comparing electron and muon final states across the pseudoscalar, vector, scalar, axial-vector, and tensor channels are displayed in Fig. 8 for the pseudoscalar, vector, scalar, axial-vector, and tensor channels.

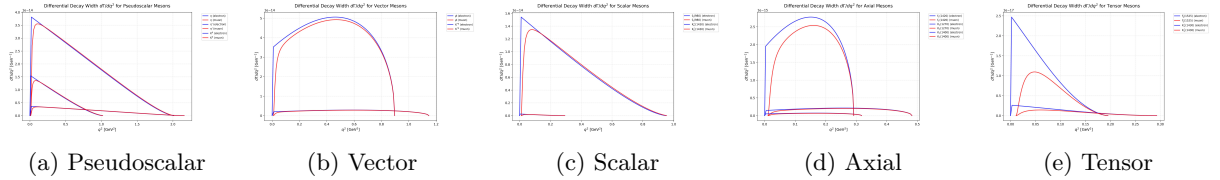


Figure 8: Semi-relativistic differential decay-width distributions for electron and muon final states across the pseudoscalar, vector, scalar, axial-vector, and tensor D_s decay channels.

For factorized nonleptonic channels we use

$$\mathcal{A}(D_s \rightarrow P_1 P_2) = \frac{G_F}{\sqrt{2}} V_{cq_1}^* V_{uq_2} a_1 f_{P_2}(m_{D_s}^2 - m_{P_1}^2) f_0^{D_s \rightarrow P_1}(m_{P_2}^2), \quad (56)$$

$$X_{D_s \rightarrow P, V} = 2f_V m_{D_s} |\mathbf{p}| f_+^{D_s \rightarrow P}(m_V^2), \quad X_{D_s \rightarrow V, P} = 2f_P m_{D_s} |\mathbf{p}| A_0^{D_s \rightarrow V}(m_P^2), \quad (57)$$

with two-body width

$$\Gamma(D_s \rightarrow M_1 M_2) = \frac{|\mathbf{p}|}{8\pi m_{D_s}^2} |\mathcal{A}|^2. \quad (58)$$

A particularly suppressed channel in the spectator- c sector is

$$D_s^+(c\bar{s}) \rightarrow D^0(c\bar{u})e^+\nu_e, \quad (59)$$

for which the physical endpoint is very small,

$$q_{\max}^2(D_s \rightarrow D^0) = (m_{D_s} - m_{D^0})^2 = 1.0714 \times 10^{-2} \text{ GeV}^2. \quad (60)$$

Using $|V_{us}| = 0.2243$ and neglecting the electron mass, the decay width can be written as

$$\Gamma(D_s^+ \rightarrow D^0 e^+ \nu_e) = 4.03 \times 10^{-20} |f_+^{D_s \rightarrow D}(0)|^2 \text{ GeV}, \quad (61)$$

which corresponds to

$$\mathcal{B}(D_s^+ \rightarrow D^0 e^+ \nu_e) = 3.07 \times 10^{-8} |f_+^{D_s \rightarrow D}(0)|^2. \quad (62)$$

For converting widths to branching fractions in the numerical block below, we use

$$\Gamma_{D_s} = \frac{\hbar}{\tau_{D_s}} = 1.31327 \times 10^{-12} \text{ GeV}. \quad (63)$$

The semileptonic, spectator- c , and selected factorized nonleptonic branching-fraction benchmarks of the D_s sector are presented in the unified format of Table 8. This consolidated presentation avoids splitting the open-charm strange decay analysis across multiple separate tables and allows the three input prescriptions to be compared channel by channel in a single place. In the compact version, rows with vanishing branching fractions have been removed, the kinematic q_{\max}^2 column is omitted, and the sector labels are displayed as centered block headings rather than separate columns.

Table 8: Combined non-zero branching fractions for D_s decays in the PDG-fit, semi-relativistic (SR), and non-relativistic (NR) inputs, with weak-decay and branching-fraction inputs guided by Refs. [3, 75]. The quantities \mathcal{B} and \mathcal{B}_C follow the notation of the supplied numerical data; all entries are written in scientific notation to four significant figures.

Channel	PDG fit		SR		NR	
	\mathcal{B}	\mathcal{B}_C	\mathcal{B}	\mathcal{B}_C	\mathcal{B}	\mathcal{B}_C
Semileptonic channels						
$D_s^+ \rightarrow \eta e^+ \nu_e$	2.517×10^{-2}	2.775×10^{-2}	2.502×10^{-2}	2.758×10^{-2}	2.624×10^{-2}	2.893×10^{-2}
$D_s^+ \rightarrow \eta \mu^+ \nu_\mu$	2.470×10^{-2}	2.723×10^{-2}	2.455×10^{-2}	2.707×10^{-2}	2.576×10^{-2}	2.840×10^{-2}
$D_s^+ \rightarrow \eta' e^+ \nu_e$	4.853×10^{-3}	5.350×10^{-3}	4.815×10^{-3}	5.309×10^{-3}	5.123×10^{-3}	5.648×10^{-3}
$D_s^+ \rightarrow \eta' \mu^+ \nu_\mu$	4.637×10^{-3}	5.113×10^{-3}	4.601×10^{-3}	5.072×10^{-3}	4.902×10^{-3}	5.404×10^{-3}
$D_s^+ \rightarrow K^0 e^+ \nu_e$	2.630×10^{-3}	2.900×10^{-3}	2.615×10^{-3}	2.883×10^{-3}	2.742×10^{-3}	3.024×10^{-3}
$D_s^+ \rightarrow K^0 \mu^+ \nu_\mu$	2.587×10^{-3}	2.852×10^{-3}	2.572×10^{-3}	2.835×10^{-3}	2.699×10^{-3}	2.975×10^{-3}
$D_s^+ \rightarrow \phi e^+ \nu_e$	2.586×10^{-2}	2.960×10^{-2}	2.564×10^{-2}	2.935×10^{-2}	2.745×10^{-2}	3.143×10^{-2}
$D_s^+ \rightarrow \phi \mu^+ \nu_\mu$	2.442×10^{-2}	2.796×10^{-2}	2.421×10^{-2}	2.772×10^{-2}	2.596×10^{-2}	2.973×10^{-2}
$D_s^+ \rightarrow K^{*0} e^+ \nu_e$	1.880×10^{-3}	2.153×10^{-3}	1.866×10^{-3}	2.136×10^{-3}	1.985×10^{-3}	2.272×10^{-3}
$D_s^+ \rightarrow K^{*0} \mu^+ \nu_\mu$	1.793×10^{-3}	2.053×10^{-3}	1.779×10^{-3}	2.037×10^{-3}	1.894×10^{-3}	2.169×10^{-3}
$D_s^+ \rightarrow f_0(980) e^+ \nu_e$	4.445×10^{-3}	4.994×10^{-3}	4.410×10^{-3}	4.955×10^{-3}	4.701×10^{-3}	5.282×10^{-3}
$D_s^+ \rightarrow f_0(980) \mu^+ \nu_\mu$	4.232×10^{-3}	4.756×10^{-3}	4.198×10^{-3}	4.717×10^{-3}	4.482×10^{-3}	5.036×10^{-3}
$D_s^+ \rightarrow K_0^*(1430) e^+ \nu_e$	2.189×10^{-5}	2.46×10^{-5}	2.158×10^{-5}	2.425×10^{-5}	2.419×10^{-5}	2.718×10^{-5}
$D_s^+ \rightarrow K_0^*(1430) \mu^+ \nu_\mu$	1.838×10^{-5}	2.065×10^{-5}	1.81×10^{-5}	2.033×10^{-5}	2.046×10^{-5}	2.299×10^{-5}
$D_s^+ \rightarrow f_1(1420) e^+ \nu_e$	4.662×10^{-4}	5.337×10^{-4}	4.594×10^{-4}	5.260×10^{-4}	5.163×10^{-4}	5.911×10^{-4}
$D_s^+ \rightarrow f_1(1420) \mu^+ \nu_\mu$	3.906×10^{-4}	4.472×10^{-4}	3.845×10^{-4}	4.403×10^{-4}	4.359×10^{-4}	4.990×10^{-4}
$D_s^+ \rightarrow K_1(1270) e^+ \nu_e$	5.916×10^{-5}	6.773×10^{-5}	5.848×10^{-5}	6.696×10^{-5}	6.409×10^{-5}	7.337×10^{-5}
$D_s^+ \rightarrow K_1(1270) \mu^+ \nu_\mu$	5.322×10^{-5}	6.093×10^{-5}	5.259×10^{-5}	6.021×10^{-5}	5.786×10^{-5}	6.624×10^{-5}
$D_s^+ \rightarrow K_1(1400) e^+ \nu_e$	1.324×10^{-5}	1.516×10^{-5}	1.306×10^{-5}	1.495×10^{-5}	1.46×10^{-5}	1.671×10^{-5}
$D_s^+ \rightarrow K_1(1400) \mu^+ \nu_\mu$	1.131×10^{-5}	1.295×10^{-5}	1.115×10^{-5}	1.276×10^{-5}	1.256×10^{-5}	1.438×10^{-5}
$D_s^+ \rightarrow f_2'(1525) e^+ \nu_e$	1.255×10^{-6}	1.518×10^{-6}	1.226×10^{-6}	1.483×10^{-6}	1.474×10^{-6}	1.784×10^{-6}
$D_s^+ \rightarrow f_2'(1525) \mu^+ \nu_\mu$	6.676×10^{-7}	8.079×10^{-7}	6.498×10^{-7}	7.863×10^{-7}	8.053×10^{-7}	9.744×10^{-7}
$D_s^+ \rightarrow K_2^*(1430) e^+ \nu_e$	2.022×10^{-7}	2.446×10^{-7}	1.985×10^{-7}	2.401×10^{-7}	2.302×10^{-7}	2.785×10^{-7}
$D_s^+ \rightarrow K_2^*(1430) \mu^+ \nu_\mu$	1.286×10^{-7}	1.556×10^{-7}	1.259×10^{-7}	1.524×10^{-7}	1.487×10^{-7}	1.799×10^{-7}
Spectator-c channel						
$D_s^+ \rightarrow D^0 e^+ \nu_e$	7.888×10^{-10}	9.201×10^{-10}	7.288×10^{-10}	8.501×10^{-10}	1.333×10^{-9}	1.555×10^{-9}
Factorized nonleptonic channels						
$D_s^+ \rightarrow \eta \pi^+$	3.807×10^{-2}	4.197×10^{-2}	3.796×10^{-2}	4.185×10^{-2}	3.887×10^{-2}	4.285×10^{-2}
$D_s^+ \rightarrow \eta \rho^+$	7.091×10^{-2}	7.818×10^{-2}	7.059×10^{-2}	7.782×10^{-2}	7.325×10^{-2}	8.076×10^{-2}
$D_s^+ \rightarrow \eta' \pi^+$	1.537×10^{-2}	1.694×10^{-2}	1.531×10^{-2}	1.687×10^{-2}	1.582×10^{-2}	1.744×10^{-2}
$D_s^+ \rightarrow \eta' \rho^+$	1.343×10^{-2}	1.481×10^{-2}	1.328×10^{-2}	1.464×10^{-2}	1.451×10^{-2}	1.600×10^{-2}
$D_s^+ \rightarrow \phi \pi^+$	3.351×10^{-2}	3.836×10^{-2}	3.336×10^{-2}	3.819×10^{-2}	3.458×10^{-2}	3.959×10^{-2}
$D_s^+ \rightarrow \phi \rho^+$	1.270×10^{-1}	1.454×10^{-1}	1.261×10^{-1}	1.444×10^{-1}	1.329×10^{-1}	1.521×10^{-1}
$D_s^+ \rightarrow K^0 \pi^+$	3.603×10^{-3}	3.972×10^{-3}	3.593×10^{-3}	3.961×10^{-3}	3.677×10^{-3}	4.054×10^{-3}
$D_s^+ \rightarrow K^0 \rho^+$	7.082×10^{-3}	7.808×10^{-3}	7.051×10^{-3}	7.774×10^{-3}	7.302×10^{-3}	8.051×10^{-3}
$D_s^+ \rightarrow K^{*0} \pi^+$	1.670×10^{-3}	1.912×10^{-3}	1.664×10^{-3}	1.905×10^{-3}	1.717×10^{-3}	1.966×10^{-3}
$D_s^+ \rightarrow K^{*0} \rho^+$	7.543×10^{-3}	8.636×10^{-3}	7.508×10^{-3}	8.595×10^{-3}	7.794×10^{-3}	8.923×10^{-3}
$D_s^+ \rightarrow f_0(980) \pi^+$	1.506×10^{-2}	1.693×10^{-2}	1.500×10^{-2}	1.685×10^{-2}	1.552×10^{-2}	1.744×10^{-2}
$D_s^+ \rightarrow K_0^*(1430) \pi^+$	2.486×10^{-4}	2.793×10^{-4}	2.466×10^{-4}	2.770×10^{-4}	2.634×10^{-4}	2.959×10^{-4}
$D_s^+ \rightarrow f_1(1420) \pi^+$	1.783×10^{-3}	2.041×10^{-3}	1.768×10^{-3}	2.024×10^{-3}	1.895×10^{-3}	2.169×10^{-3}
$D_s^+ \rightarrow K_1(1270) \pi^+$	1.389×10^{-4}	1.591×10^{-4}	1.381×10^{-4}	1.581×10^{-4}	1.453×10^{-4}	1.664×10^{-4}
$D_s^+ \rightarrow K_1(1400) \pi^+$	5.004×10^{-5}	5.729×10^{-5}	4.963×10^{-5}	5.682×10^{-5}	5.301×10^{-5}	6.07×10^{-5}
$D_s^+ \rightarrow f_2'(1525) \pi^+$	4.146×10^{-5}	5.016×10^{-5}	4.068×10^{-5}	4.922×10^{-5}	4.724×10^{-5}	5.717×10^{-5}
$D_s^+ \rightarrow K_2^*(1430) \pi^+$	4.681×10^{-6}	5.664×10^{-6}	4.614×10^{-6}	5.582×10^{-6}	5.18×10^{-6}	6.267×10^{-6}

The experimental normalization of the most relevant D_s^+ and D_s^{*+} channels is discussed in Sec. 6.1, where the semi-relativistic corrected branching fractions are converted to partial widths and compared directly with the PDG 2025 listings and the corresponding experimental measurements. This comparison is not used to refit the present form factors; it is used only to identify the daughter modes that are most reliable for the later spectator-cascade estimates.

The combined non-zero branching-fraction results for the D_s meson are collected in Table 8, where the semileptonic, spectator- c , and factorized nonleptonic channels are displayed under separate block headings

through a single Channel column. In the semileptonic sector, the total muonic branching fractions are 5.359×10^{-3} , 5.355×10^{-3} , and 5.391×10^{-3} for the PDG-fit, semi-relativistic, and non-relativistic inputs, respectively, while the corresponding tauonic totals are 5.223×10^{-2} , 5.142×10^{-2} , and 5.811×10^{-2} . For the representative muonic channels one finds $\mathcal{B}(D_s^+ \rightarrow \eta \mu^+ \nu_\mu) = 2.723 \times 10^{-2}$, 2.707×10^{-2} , 2.840×10^{-2} ; $\mathcal{B}(D_s^+ \rightarrow \phi \mu^+ \nu_\mu) = 2.796 \times 10^{-2}$, 2.772×10^{-2} , 2.973×10^{-2} ; $\mathcal{B}(D_s^+ \rightarrow f_0(980) \mu^+ \nu_\mu) = 4.756 \times 10^{-3}$, 4.717×10^{-3} , 5.036×10^{-3} ; $\mathcal{B}(D_s^+ \rightarrow f_1(1420) \mu^+ \nu_\mu) = 4.472 \times 10^{-4}$, 4.403×10^{-4} , 4.990×10^{-4} ; and $\mathcal{B}(D_s^+ \rightarrow f_2'(1525) \mu^+ \nu_\mu) = 8.079 \times 10^{-7}$, 7.863×10^{-7} , 9.744×10^{-7} in the same three schemes. In the spectator- c sector, after removing the channels with vanishing branching fractions, only the electron mode $D_s^+ \rightarrow D^0 e^+ \nu_e$ remains, with $\mathcal{B} = 7.888 \times 10^{-10}$, 7.288×10^{-10} , 1.333×10^{-9} and corrected values $\mathcal{B}_C = 9.201 \times 10^{-10}$, 8.501×10^{-10} , 1.555×10^{-9} for the PDG-fit, semi-relativistic, and non-relativistic inputs, respectively.

5.2 Tetraquark Rearrangement Decay

For the compact open-flavor tetraquark the dominant topology is the Fierz rearrangement

$$cs\bar{s}\bar{s} \longrightarrow (c\bar{s})(s\bar{s}), \quad (64)$$

where the $c\bar{s}$ and $s\bar{s}$ bilinears are brought together and normalized to unity, following the spectator-pair idea used in Ref. [77]. In the present $cs\bar{s}\bar{s}$ system the rearranged color-singlet pairs appear on shell as

$$(c\bar{s})_{0-} \rightarrow D_s, \quad (c\bar{s})_{1-} \rightarrow D_s^*, \quad (s\bar{s})_{0-} \rightarrow \eta, \eta', \quad (s\bar{s})_{1-} \rightarrow \phi. \quad (65)$$

Thus the primary two-body modes are $D_s^{(*)} X_s$, with $X_s = \eta, \eta', \phi$. This topology is the most direct strong-decay diagnostic of a compact $cs\bar{s}\bar{s}$ state because it does not require creating light non-strange valence quarks; it instead tests the overlap between the compact $[cs][\bar{s}\bar{s}]$ wavefunction and the $D_s^{(*)} X_s$ continuum. The channel set also overlaps with the decay modes emphasized in recent multi-strange tetraquark calculations, where $D_s \eta'$, $D_{(s)}^* \phi$, and related vector-vector channels were identified as promising search modes [58]. The absolute primary vertices are evaluated with the two-point and three-point QCD sum-rule construction described below, while the subsequent observed channels are obtained by allowing the rearranged mesons to decay.

The daughter-meson part of the rearrangement decay is implemented in direct analogy with the spectator-pair treatment. For the $cs\bar{s}\bar{s}$ tetraquark the relevant mechanisms are:

- A spin-0 color-singlet $s\bar{s}$ pair, represented by the strange component of η or η' , can annihilate into two gluons or two photons; the gluons hadronize into lighter hadrons and the leading strong annihilation rate is of order α_s^2 .
- A spin-1 color-singlet $s\bar{s}$ pair, represented mainly by the ϕ , decays through its physical hadronic and electromagnetic modes, such as $K\bar{K}$, $\ell^+ \ell^-$ and radiative $P\gamma$ channels. The compact annihilation component corresponds to three-gluon annihilation and is of order α_s^3 .
- Color-octet $s\bar{s}$ components do not directly form an isolated meson pair. In the rearrangement picture their spin-0 and spin-1 annihilation pieces proceed through one-gluon and two-gluon mechanisms, respectively, followed by color neutralization and hadronization.
- A spin-0 color-singlet $c\bar{s}$ pair appears as the D_s meson. It can decay through purely leptonic modes $\ell^+ \nu_\ell$, semileptonic modes, rare radiative leptonic modes $\gamma \ell^+ \nu_\ell$, and factorized two-body nonleptonic channels.

- A spin-1 color-singlet $c\bar{s}$ pair appears as D_s^* . In the present analysis it is treated as a feed-down source to D_s through $D_s^* \rightarrow D_s\gamma$ and $D_s^* \rightarrow D_s\pi^0$, after which the reconstructed D_s decays as in the open-charm meson sector.

For the one-meson spectator-cascade tables below, no additional overlap factor is applied. Each entry is obtained directly from the primary rearrangement width multiplied by the physical branching fraction of the single daughter meson that is explicitly shown as decaying. The D_s daughter modes used here are those collected in Table 8. The hidden-strange vector modes are summarized in Table 7, while the pseudoscalar strange components are included through the physical η and η' channels. For a specific observed cascade we decay only one daughter meson at a time. If H_a decays while H_b remains as the on-shell spectator, or vice versa, the widths are

$$\begin{aligned}\Gamma(T_J \rightarrow [H_a \rightarrow F_a]H_b) &= \Gamma(T_J \rightarrow H_a H_b) \mathcal{B}(H_a \rightarrow F_a), \\ \Gamma(T_J \rightarrow H_a[H_b \rightarrow F_b]) &= \Gamma(T_J \rightarrow H_a H_b) \mathcal{B}(H_b \rightarrow F_b).\end{aligned}\quad (66)$$

No entry below multiplies two daughter branching fractions in the same row. Table 9 lists the primary two-body rearrangement widths, while Tables 10–12 give the expanded one-meson spectator-cascade rates for the 0^+ , 1^+ and 2^+ assignments, respectively, obtained from Eq. (66).

The spectroscopy part of the calculation treats the low-lying S -wave tetraquarks as axial-diquark–axial-antidiquark states with $S_d = S_{\bar{d}} = 1$. Recoupling the spin wave functions from the diquark basis to the meson-meson basis gives

$$|\{(cs)^1(\bar{s}\bar{s})^1\}^0\rangle = -\frac{1}{2} |\{(c\bar{s})^1(s\bar{s})^1\}^0\rangle + \frac{\sqrt{3}}{2} |\{(c\bar{s})^0(s\bar{s})^0\}^0\rangle, \quad (67a)$$

$$|\{(cs)^1(\bar{s}\bar{s})^1\}^1\rangle = \frac{1}{\sqrt{2}} |\{(c\bar{s})^1(s\bar{s})^0\}^1\rangle + \frac{1}{\sqrt{2}} |\{(c\bar{s})^0(s\bar{s})^1\}^1\rangle, \quad (67b)$$

$$|\{(cs)^1(\bar{s}\bar{s})^1\}^2\rangle = |\{(c\bar{s})^1(s\bar{s})^1\}^2\rangle. \quad (67c)$$

The corresponding color recouplings are

$$|[cs]_{\bar{\mathbf{3}}}[s\bar{s}]_{\mathbf{3}}\rangle = \sqrt{\frac{1}{3}} |(c\bar{s})_{\mathbf{1}}(s\bar{s})_{\mathbf{1}}\rangle - \sqrt{\frac{2}{3}} |(c\bar{s})_{\mathbf{8}}(s\bar{s})_{\mathbf{8}}\rangle, \quad (68a)$$

$$|[cs]_{\mathbf{6}}[s\bar{s}]_{\bar{\mathbf{6}}}\rangle = \sqrt{\frac{2}{3}} |(c\bar{s})_{\mathbf{1}}(s\bar{s})_{\mathbf{1}}\rangle + \sqrt{\frac{1}{3}} |(c\bar{s})_{\mathbf{8}}(s\bar{s})_{\mathbf{8}}\rangle. \quad (68b)$$

Only the color-singlet–color-singlet pieces directly form two physical mesons. The corresponding numerical weights are kept in prose rather than as a separate displayed equation: for the $\bar{\mathbf{3}} - \mathbf{3}$ configuration they are 1/4 for $0^+ \rightarrow D_s\eta_s$, 1/12 for $0^+ \rightarrow D_s^*\phi$, 1/6 for the two 1^+ VP modes, and 1/3 for $2^+ \rightarrow D_s^*\phi$; for the $\mathbf{6} - \bar{\mathbf{6}}$ configuration the corresponding weights are 1/2, 1/6, 1/3, and 2/3. For physical η and η' channels the strange pseudoscalar component is projected through the usual quark-flavor mixing, $\eta_s = -\sin\varphi_P\eta + \cos\varphi_P\eta'$. In the numerical evaluation this mixing is included through the physical QCDSR matrix elements h_η^s and $h_{\eta'}^s$.

The two-point QCD sum rules determine the tetraquark masses and pole residues,

$$\Pi_J^{2\text{pt}} \longrightarrow M_J, \lambda_J, \quad (69)$$

while the three-point sum rules determine the hadronic vertices,

$$\Pi_i^{3\text{pt}} \longrightarrow G_i. \quad (70)$$

For a generic rearrangement channel $T_J(p') \rightarrow H_1(p)H_2(q)$, with $p' = p + q$, the three-point correlator is

$$\Pi_i(p, q) = i^2 \int d^4x d^4y e^{ip \cdot x + iq \cdot y} \langle 0 | T \{ j_{H_1}(x) j_{H_2}(y) J_T^\dagger(0) \} | 0 \rangle. \quad (71)$$

After isolating a clean Lorentz structure, the hadron side is written as

$$\Pi_i^{\text{had}} = \frac{\Lambda_i G_i}{(M_J^2 - p'^2)(m_1^2 - p^2)(m_2^2 - q^2)} + \frac{C_i}{(m_1^2 - p^2)(m_2^2 - q^2)} + \dots, \quad (72)$$

where Λ_i contains the tetraquark pole residue and the two meson decay constants. The parameter C_i accounts for tetraquark-channel transitions to excited and continuum states. On the QCD side one obtains the double spectral representation

$$\Pi_i^{\text{QCD}}(p'^2, p^2, q^2) = \int ds du \frac{\rho_i^{\text{QCD}}(s, u)}{(s - p^2)(u - q^2)} + \dots. \quad (73)$$

Using the direct three-point prescription $p'^2 = \alpha p^2$ with $\alpha = 4$ for open-charm final mesons and applying the double Borel transformation gives the linear working equation

$$R_i(T_1^2, T_2^2) = A_i(T_1^2, T_2^2)G_i + B_i(T_1^2, T_2^2)C_i, \quad (74)$$

where

$$R_i = \int_{\Delta_1^2}^{s_1^0} ds \int_{\Delta_2^2}^{u_0} du \rho_i^{\text{QCD}}(s, u) e^{-s/T_1^2 - u/T_2^2}, \quad (75a)$$

$$A_i = \frac{\Lambda_i}{M_J^2 - \alpha m_1^2} \left[e^{-m_1^2/T_1^2} - e^{-M_J^2/(\alpha T_1^2)} \right] e^{-m_2^2/T_2^2}, \quad (75b)$$

$$B_i = e^{-m_1^2/T_1^2 - m_2^2/T_2^2}. \quad (75c)$$

The coupling G_i and transition parameter C_i are obtained by fitting Eq. (74) over the accepted Borel window. The rearrangement-projected partial width is then

$$\Gamma_i^{\text{rearr}} = \mathcal{W}_i \Gamma_i^{\text{3pt}}(M_J, m_1, m_2, G_i), \quad (76)$$

where Γ_i^{3pt} is the two-body width obtained from the QCDSR coupling and the present masses. This form keeps the Fierz color-spin rearrangement used in Ref. [77], while the absolute vertex strength remains determined by the three-point QCDSR calculation.

The numerical evaluation uses the standard two-body phase space for the allowed PP , VP , and VV rearrangement vertices, with the kinematic momentum $|\vec{p}| = \sqrt{\lambda(M_J^2, m_1^2, m_2^2)}/(2M_J)$. The 2^+ PP and VP modes are higher-partial-wave channels; they are not included in the leading rearrangement table below.

Table 9: Calculated primary rearrangement decay rates of the ground-state $c\bar{s}\bar{s}\bar{s}$ tetraquarks before multiplication by daughter-meson branching fractions, following QCD-sum-rule and Fierz-rearrangement treatments of open-charm tetraquark decays [35, 69, 70]. Only channels and decay rates are tabulated. All rates are in MeV.

Channel	$\bar{\mathbf{3}} - \mathbf{3}$ SR	$\bar{\mathbf{3}} - \mathbf{3}$ NR	$\mathbf{6} - \bar{\mathbf{6}}$ SR	$\mathbf{6} - \bar{\mathbf{6}}$ NR
$0^+ : T_0 \rightarrow D_s \eta$	9.428	9.475	19.27	8.360

Continued on next page

Table 9 – continued from previous page

Channel	$\bar{\mathbf{3}} - \mathbf{3}$ SR	$\bar{\mathbf{3}} - \mathbf{3}$ NR	$\mathbf{6} - \bar{\mathbf{6}}$ SR	$\mathbf{6} - \bar{\mathbf{6}}$ NR
$0^+ : T_0 \rightarrow D_s \eta'$	8.607	8.807	19.15	0
$0^+ : T_0 \rightarrow D_s^* \phi$	2.670	2.939	8.778	0
$1^+ : T_1 \rightarrow D_s \phi$	5.745	5.878	12.75	0
$1^+ : T_1 \rightarrow D_s^* \eta$	2.505	2.523	5.173	0
$1^+ : T_1 \rightarrow D_s^* \eta'$	2.238	2.287	4.903	0
$2^+ : T_2 \rightarrow D_s^* \phi$	5.177	5.213	9.307	0

The expanded one-meson spectator-cascade tables below use all non-zero D_s^+ daughter channels listed in Table 8, the two dominant D_s^{*+} feed-down η , η' and ϕ daughter modes used for the hidden-strange component. They are split by tetraquark spin assignment into separate 0^+ , 1^+ and 2^+ tables. For the 1^+ and 2^+ spectator-cascade tables, the $\mathbf{6} - \bar{\mathbf{6}}$ NR column is omitted because all entries vanish: the corresponding central tetraquark masses lie below the relevant rearrangement thresholds. Inclusive daughter entries and upper limits are not combined with exclusive rows, because doing so would double count final states. Each entry still decays only one daughter meson at a time:

$$\Gamma(T_J \rightarrow [H_a \rightarrow f_a]H_b) = \Gamma(T_J \rightarrow H_a H_b) \mathcal{B}(H_a \rightarrow f_a), \quad (77)$$

or equivalently with H_a and H_b interchanged. The bracketed meson is the decaying daughter and the unbracketed meson is kept on shell.

Table 10: Expanded one-meson spectator-cascade decay rates of the ground-state $0^+ cs\bar{s}\bar{s}$ tetraquark, using daughter branching-fraction inputs from Refs. [3, 75]. Only one daughter meson decays in each row; all rates are in MeV.

Channel	$\bar{\mathbf{3}} - \mathbf{3}$ SR	$\bar{\mathbf{3}} - \mathbf{3}$ NR	$\mathbf{6} - \bar{\mathbf{6}}$ SR	$\mathbf{6} - \bar{\mathbf{6}}$ NR
D_s^+ daughter decays; hidden-strange meson kept on shell				
$0^+ : T_0 \rightarrow [D_s^+ \rightarrow \eta e^+ \nu_e] \eta$	2.6×10^{-1}	2.741×10^{-1}	5.315×10^{-1}	2.419×10^{-1}
$0^+ : T_0 \rightarrow [D_s^+ \rightarrow \eta \mu^+ \nu_\mu] \eta$	2.552×10^{-1}	2.691×10^{-1}	5.216×10^{-1}	2.374×10^{-1}
$0^+ : T_0 \rightarrow [D_s^+ \rightarrow \eta' e^+ \nu_e] \eta$	5.005×10^{-2}	5.351×10^{-2}	1.023×10^{-1}	4.722×10^{-2}
$0^+ : T_0 \rightarrow [D_s^+ \rightarrow \eta' \mu^+ \nu_\mu] \eta$	4.782×10^{-2}	5.12×10^{-2}	9.774×10^{-2}	4.518×10^{-2}
$0^+ : T_0 \rightarrow [D_s^+ \rightarrow K^0 e^+ \nu_e] \eta$	2.718×10^{-2}	2.865×10^{-2}	5.556×10^{-2}	2.528×10^{-2}
$0^+ : T_0 \rightarrow [D_s^+ \rightarrow K^0 \mu^+ \nu_\mu] \eta$	2.673×10^{-2}	2.819×10^{-2}	5.463×10^{-2}	2.487×10^{-2}
$0^+ : T_0 \rightarrow [D_s^+ \rightarrow \phi e^+ \nu_e] \eta$	2.767×10^{-1}	2.978×10^{-1}	5.656×10^{-1}	2.628×10^{-1}
$0^+ : T_0 \rightarrow [D_s^+ \rightarrow \phi \mu^+ \nu_\mu] \eta$	2.613×10^{-1}	2.817×10^{-1}	5.342×10^{-1}	2.485×10^{-1}
$0^+ : T_0 \rightarrow [D_s^+ \rightarrow K^{*0} e^+ \nu_e] \eta$	2.014×10^{-2}	2.153×10^{-2}	4.116×10^{-2}	1.899×10^{-2}
$0^+ : T_0 \rightarrow [D_s^+ \rightarrow K^{*0} \mu^+ \nu_\mu] \eta$	1.92×10^{-2}	2.055×10^{-2}	3.925×10^{-2}	1.813×10^{-2}
$0^+ : T_0 \rightarrow [D_s^+ \rightarrow f_0(980) e^+ \nu_e] \eta$	4.672×10^{-2}	5.005×10^{-2}	9.548×10^{-2}	4.416×10^{-2}
$0^+ : T_0 \rightarrow [D_s^+ \rightarrow f_0(980) \mu^+ \nu_\mu] \eta$	4.447×10^{-2}	4.772×10^{-2}	9.09×10^{-2}	4.21×10^{-2}
$0^+ : T_0 \rightarrow [D_s^+ \rightarrow K_0^*(1430) e^+ \nu_e] \eta$	2.286×10^{-4}	2.575×10^{-4}	4.673×10^{-4}	2.272×10^{-4}
$0^+ : T_0 \rightarrow [D_s^+ \rightarrow K_0^*(1430) \mu^+ \nu_\mu] \eta$	1.917×10^{-4}	2.178×10^{-4}	3.918×10^{-4}	1.922×10^{-4}
$0^+ : T_0 \rightarrow [D_s^+ \rightarrow f_1(1420) e^+ \nu_e] \eta$	4.959×10^{-3}	5.601×10^{-3}	1.014×10^{-2}	4.942×10^{-3}
$0^+ : T_0 \rightarrow [D_s^+ \rightarrow f_1(1420) \mu^+ \nu_\mu] \eta$	4.151×10^{-3}	4.728×10^{-3}	8.485×10^{-3}	4.172×10^{-3}
$0^+ : T_0 \rightarrow [D_s^+ \rightarrow K_1(1270) e^+ \nu_e] \eta$	6.313×10^{-4}	6.952×10^{-4}	1.29×10^{-3}	6.134×10^{-4}
$0^+ : T_0 \rightarrow [D_s^+ \rightarrow K_1(1270) \mu^+ \nu_\mu] \eta$	5.677×10^{-4}	6.276×10^{-4}	1.16×10^{-3}	5.538×10^{-4}
$0^+ : T_0 \rightarrow [D_s^+ \rightarrow K_1(1400) e^+ \nu_e] \eta$	1.409×10^{-4}	1.583×10^{-4}	2.881×10^{-4}	1.397×10^{-4}
$0^+ : T_0 \rightarrow [D_s^+ \rightarrow K_1(1400) \mu^+ \nu_\mu] \eta$	1.203×10^{-4}	1.363×10^{-4}	2.459×10^{-4}	1.202×10^{-4}
$0^+ : T_0 \rightarrow [D_s^+ \rightarrow f_2'(1525) e^+ \nu_e] \eta$	1.398×10^{-5}	1.69×10^{-5}	2.858×10^{-5}	1.491×10^{-5}
$0^+ : T_0 \rightarrow [D_s^+ \rightarrow f_2'(1525) \mu^+ \nu_\mu] \eta$	7.413×10^{-6}	9.232×10^{-6}	1.515×10^{-5}	8.146×10^{-6}
$0^+ : T_0 \rightarrow [D_s^+ \rightarrow K_2^*(1430) e^+ \nu_e] \eta$	2.264×10^{-6}	2.639×10^{-6}	4.627×10^{-6}	2.328×10^{-6}
$0^+ : T_0 \rightarrow [D_s^+ \rightarrow K_2^*(1430) \mu^+ \nu_\mu] \eta$	1.437×10^{-6}	1.705×10^{-6}	2.937×10^{-6}	1.504×10^{-6}
$0^+ : T_0 \rightarrow [D_s^+ \rightarrow D^0 e^+ \nu_e] \eta$	8.015×10^{-9}	1.473×10^{-8}	1.638×10^{-8}	1.3×10^{-8}
$0^+ : T_0 \rightarrow [D_s^+ \rightarrow \eta \pi^+] \eta$	3.946×10^{-1}	4.06×10^{-1}	8.064×10^{-1}	3.582×10^{-1}
$0^+ : T_0 \rightarrow [D_s^+ \rightarrow \eta \rho^+] \eta$	7.337×10^{-1}	7.652×10^{-1}	1.5×10^0	6.752×10^{-1}
$0^+ : T_0 \rightarrow [D_s^+ \rightarrow \eta' \pi^+] \eta$	1.591×10^{-1}	1.652×10^{-1}	3.251×10^{-1}	1.458×10^{-1}
$0^+ : T_0 \rightarrow [D_s^+ \rightarrow \eta' \rho^+] \eta$	1.38×10^{-1}	1.516×10^{-1}	2.821×10^{-1}	1.338×10^{-1}
$0^+ : T_0 \rightarrow [D_s^+ \rightarrow \phi \pi^+] \eta$	3.601×10^{-1}	3.751×10^{-1}	7.359×10^{-1}	3.31×10^{-1}
$0^+ : T_0 \rightarrow [D_s^+ \rightarrow \phi \rho^+] \eta$	1.361×10^0	1.441×10^0	2.783×10^0	1.272×10^0
$0^+ : T_0 \rightarrow [D_s^+ \rightarrow K^0 \pi^+] \eta$	3.734×10^{-2}	3.841×10^{-2}	7.633×10^{-2}	3.389×10^{-2}
$0^+ : T_0 \rightarrow [D_s^+ \rightarrow K^0 \rho^+] \eta$	7.329×10^{-2}	7.628×10^{-2}	1.498×10^{-1}	6.731×10^{-2}
$0^+ : T_0 \rightarrow [D_s^+ \rightarrow K^{*0} \pi^+] \eta$	1.796×10^{-2}	1.863×10^{-2}	3.671×10^{-2}	1.644×10^{-2}
$0^+ : T_0 \rightarrow [D_s^+ \rightarrow K^{*0} \rho^+] \eta$	8.103×10^{-2}	8.455×10^{-2}	1.656×10^{-1}	7.46×10^{-2}
$0^+ : T_0 \rightarrow [D_s^+ \rightarrow f_0(980) \pi^+] \eta$	1.589×10^{-1}	1.652×10^{-1}	3.247×10^{-1}	1.458×10^{-1}
$0^+ : T_0 \rightarrow [D_s^+ \rightarrow K_0^*(1430) \pi^+] \eta$	2.612×10^{-3}	2.804×10^{-3}	5.338×10^{-3}	2.474×10^{-3}
$0^+ : T_0 \rightarrow [D_s^+ \rightarrow f_1(1420) \pi^+] \eta$	1.908×10^{-2}	2.055×10^{-2}	3.9×10^{-2}	1.813×10^{-2}
$0^+ : T_0 \rightarrow [D_s^+ \rightarrow K_1(1270) \pi^+] \eta$	1.491×10^{-3}	1.577×10^{-3}	3.047×10^{-3}	1.391×10^{-3}
$0^+ : T_0 \rightarrow [D_s^+ \rightarrow K_1(1400) \pi^+] \eta$	5.357×10^{-4}	5.751×10^{-4}	1.095×10^{-3}	5.075×10^{-4}
$0^+ : T_0 \rightarrow [D_s^+ \rightarrow f_2'(1525) \pi^+] \eta$	4.64×10^{-4}	5.417×10^{-4}	9.485×10^{-4}	4.779×10^{-4}
$0^+ : T_0 \rightarrow [D_s^+ \rightarrow K_2^*(1430) \pi^+] \eta$	5.263×10^{-5}	5.938×10^{-5}	1.076×10^{-4}	5.239×10^{-5}
$0^+ : T_0 \rightarrow [D_s^+ \rightarrow \eta e^+ \nu_e] \eta'$	2.374×10^{-1}	2.548×10^{-1}	5.282×10^{-1}	0
$0^+ : T_0 \rightarrow [D_s^+ \rightarrow \eta \mu^+ \nu_\mu] \eta'$	2.33×10^{-1}	2.501×10^{-1}	5.184×10^{-1}	0
$0^+ : T_0 \rightarrow [D_s^+ \rightarrow \eta' e^+ \nu_e] \eta'$	4.569×10^{-2}	4.974×10^{-2}	1.017×10^{-1}	0
$0^+ : T_0 \rightarrow [D_s^+ \rightarrow \eta' \mu^+ \nu_\mu] \eta'$	4.365×10^{-2}	4.759×10^{-2}	9.713×10^{-2}	0
$0^+ : T_0 \rightarrow [D_s^+ \rightarrow K^0 e^+ \nu_e] \eta'$	2.481×10^{-2}	2.663×10^{-2}	5.521×10^{-2}	0

Continued on next page

Table 10 – continued from previous page

Channel	$\bar{3} - \bar{3}$ SR	$\bar{3} - \bar{3}$ NR	$\mathbf{6} - \bar{\mathbf{6}}$ SR	$\mathbf{6} - \bar{\mathbf{6}}$ NR
$0^+ : T_0 \rightarrow [D_s^+ \rightarrow K^0 \mu^+ \nu_\mu] \eta'$	2.44×10^{-2}	2.62×10^{-2}	5.429×10^{-2}	0
$0^+ : T_0 \rightarrow [D_s^+ \rightarrow \phi e^+ \nu_e] \eta'$	2.526×10^{-1}	2.768×10^{-1}	5.621×10^{-1}	0
$0^+ : T_0 \rightarrow [D_s^+ \rightarrow \phi \mu^+ \nu_\mu] \eta'$	2.386×10^{-1}	2.618×10^{-1}	5.308×10^{-1}	0
$0^+ : T_0 \rightarrow [D_s^+ \rightarrow K^{*0} e^+ \nu_e] \eta'$	1.838×10^{-2}	2.001×10^{-2}	4.09×10^{-2}	0
$0^+ : T_0 \rightarrow [D_s^+ \rightarrow K^{*0} \mu^+ \nu_\mu] \eta'$	1.753×10^{-2}	1.91×10^{-2}	3.901×10^{-2}	0
$0^+ : T_0 \rightarrow [D_s^+ \rightarrow f_0(980) e^+ \nu_e] \eta'$	4.265×10^{-2}	4.652×10^{-2}	9.489×10^{-2}	0
$0^+ : T_0 \rightarrow [D_s^+ \rightarrow f_0(980) \mu^+ \nu_\mu] \eta'$	4.06×10^{-2}	4.435×10^{-2}	9.033×10^{-2}	0
$0^+ : T_0 \rightarrow [D_s^+ \rightarrow K_0^*(1430) e^+ \nu_e] \eta'$	2.087×10^{-4}	2.394×10^{-4}	4.644×10^{-4}	0
$0^+ : T_0 \rightarrow [D_s^+ \rightarrow K_0^*(1430) \mu^+ \nu_\mu] \eta'$	1.75×10^{-4}	2.025×10^{-4}	3.893×10^{-4}	0
$0^+ : T_0 \rightarrow [D_s^+ \rightarrow f_1(1420) e^+ \nu_e] \eta'$	4.527×10^{-3}	5.206×10^{-3}	1.007×10^{-2}	0
$0^+ : T_0 \rightarrow [D_s^+ \rightarrow f_1(1420) \mu^+ \nu_\mu] \eta'$	3.79×10^{-3}	4.395×10^{-3}	8.432×10^{-3}	0
$0^+ : T_0 \rightarrow [D_s^+ \rightarrow K_1(1270) e^+ \nu_e] \eta'$	5.763×10^{-4}	6.462×10^{-4}	1.282×10^{-3}	0
$0^+ : T_0 \rightarrow [D_s^+ \rightarrow K_1(1270) \mu^+ \nu_\mu] \eta'$	5.182×10^{-4}	5.834×10^{-4}	1.153×10^{-3}	0
$0^+ : T_0 \rightarrow [D_s^+ \rightarrow K_1(1400) e^+ \nu_e] \eta'$	1.287×10^{-4}	1.472×10^{-4}	2.863×10^{-4}	0
$0^+ : T_0 \rightarrow [D_s^+ \rightarrow K_1(1400) \mu^+ \nu_\mu] \eta'$	1.098×10^{-4}	1.266×10^{-4}	2.444×10^{-4}	0
$0^+ : T_0 \rightarrow [D_s^+ \rightarrow f_2'(1525) e^+ \nu_e] \eta'$	1.276×10^{-5}	1.571×10^{-5}	2.84×10^{-5}	0
$0^+ : T_0 \rightarrow [D_s^+ \rightarrow f_2'(1525) \mu^+ \nu_\mu] \eta'$	6.768×10^{-6}	8.582×10^{-6}	1.506×10^{-5}	0
$0^+ : T_0 \rightarrow [D_s^+ \rightarrow K_2^*(1430) e^+ \nu_e] \eta'$	2.067×10^{-6}	2.453×10^{-6}	4.598×10^{-6}	0
$0^+ : T_0 \rightarrow [D_s^+ \rightarrow K_2^*(1430) \mu^+ \nu_\mu] \eta'$	1.312×10^{-6}	1.584×10^{-6}	2.918×10^{-6}	0
$0^+ : T_0 \rightarrow [D_s^+ \rightarrow D^0 e^+ \nu_e] \eta'$	7.317×10^{-9}	1.369×10^{-8}	1.628×10^{-8}	0
$0^+ : T_0 \rightarrow [D_s^+ \rightarrow \eta \pi^+] \eta'$	3.602×10^{-1}	3.774×10^{-1}	8.014×10^{-1}	0
$0^+ : T_0 \rightarrow [D_s^+ \rightarrow \eta \rho^+] \eta'$	6.698×10^{-1}	7.113×10^{-1}	1.49×10^0	0
$0^+ : T_0 \rightarrow [D_s^+ \rightarrow \eta' \pi^+] \eta'$	1.452×10^{-1}	1.536×10^{-1}	3.231×10^{-1}	0
$0^+ : T_0 \rightarrow [D_s^+ \rightarrow \eta' \rho^+] \eta'$	1.26×10^{-1}	1.409×10^{-1}	2.804×10^{-1}	0
$0^+ : T_0 \rightarrow [D_s^+ \rightarrow \phi \pi^+] \eta'$	3.287×10^{-1}	3.487×10^{-1}	7.313×10^{-1}	0
$0^+ : T_0 \rightarrow [D_s^+ \rightarrow \phi \rho^+] \eta'$	1.243×10^0	1.34×10^0	2.765×10^0	0
$0^+ : T_0 \rightarrow [D_s^+ \rightarrow K^0 \pi^+] \eta'$	3.409×10^{-2}	3.57×10^{-2}	7.585×10^{-2}	0
$0^+ : T_0 \rightarrow [D_s^+ \rightarrow K^0 \rho^+] \eta'$	6.691×10^{-2}	7.091×10^{-2}	1.489×10^{-1}	0
$0^+ : T_0 \rightarrow [D_s^+ \rightarrow K^{*0} \pi^+] \eta'$	1.64×10^{-2}	1.731×10^{-2}	3.648×10^{-2}	0
$0^+ : T_0 \rightarrow [D_s^+ \rightarrow K^{*0} \rho^+] \eta'$	7.398×10^{-2}	7.858×10^{-2}	1.646×10^{-1}	0
$0^+ : T_0 \rightarrow [D_s^+ \rightarrow f_0(980) \pi^+] \eta'$	1.45×10^{-1}	1.536×10^{-1}	3.227×10^{-1}	0
$0^+ : T_0 \rightarrow [D_s^+ \rightarrow K_0^*(1430) \pi^+] \eta'$	2.384×10^{-3}	2.606×10^{-3}	5.305×10^{-3}	0
$0^+ : T_0 \rightarrow [D_s^+ \rightarrow f_1(1420) \pi^+] \eta'$	1.742×10^{-2}	1.91×10^{-2}	3.876×10^{-2}	0
$0^+ : T_0 \rightarrow [D_s^+ \rightarrow K_1(1270) \pi^+] \eta'$	1.361×10^{-3}	1.465×10^{-3}	3.028×10^{-3}	0
$0^+ : T_0 \rightarrow [D_s^+ \rightarrow K_1(1400) \pi^+] \eta'$	4.89×10^{-4}	5.346×10^{-4}	1.088×10^{-3}	0
$0^+ : T_0 \rightarrow [D_s^+ \rightarrow f_2'(1525) \pi^+] \eta'$	4.236×10^{-4}	5.035×10^{-4}	9.426×10^{-4}	0
$0^+ : T_0 \rightarrow [D_s^+ \rightarrow K_2^*(1430) \pi^+] \eta'$	4.804×10^{-5}	5.519×10^{-5}	1.069×10^{-4}	0
D_s^{*+} daughter feed-down; hidden-strange meson kept on shell				
$0^+ : T_0 \rightarrow [D_s^{*+} \rightarrow D_s^+ \gamma] \phi$	2.498×10^0	2.75×10^0	8.214×10^0	0
$0^+ : T_0 \rightarrow [D_s^{*+} \rightarrow D_s^+ \pi^0] \phi$	1.538×10^{-1}	1.693×10^{-1}	5.056×10^{-1}	0
Hidden-strange daughter decays; $D_s^{(*)}$ meson kept on shell				
$0^+ : T_0 \rightarrow D_s^+ [\eta \rightarrow \gamma\gamma]$	3.711×10^0	3.729×10^0	7.584×10^0	3.29×10^0
$0^+ : T_0 \rightarrow D_s^+ [\eta \rightarrow 3\pi^0]$	3.07×10^0	3.085×10^0	6.275×10^0	2.722×10^0
$0^+ : T_0 \rightarrow D_s^+ [\eta \rightarrow \pi^+ \pi^- \pi^0]$	2.17×10^0	2.181×10^0	4.436×10^0	1.924×10^0
$0^+ : T_0 \rightarrow D_s^+ [\eta \rightarrow \pi^+ \pi^- \gamma]$	4.032×10^{-1}	4.052×10^{-1}	8.242×10^{-1}	3.575×10^{-1}
$0^+ : T_0 \rightarrow D_s^+ [\eta \rightarrow e^+ e^- \gamma]$	6.604×10^{-2}	6.637×10^{-2}	1.35×10^{-1}	5.856×10^{-2}
$0^+ : T_0 \rightarrow D_s^+ [\eta \rightarrow \mu^+ \mu^- \gamma]$	2.924×10^{-3}	2.939×10^{-3}	5.977×10^{-3}	2.593×10^{-3}
$0^+ : T_0 \rightarrow D_s^+ [\eta \rightarrow \pi^0 \gamma\gamma]$	2.408×10^{-3}	2.42×10^{-3}	4.921×10^{-3}	2.135×10^{-3}
$0^+ : T_0 \rightarrow D_s^+ [\eta \rightarrow \pi^+ \pi^- e^+ e^- (\gamma)]$	2.527×10^{-3}	2.539×10^{-3}	5.165×10^{-3}	2.241×10^{-3}
$0^+ : T_0 \rightarrow D_s^+ [\eta \rightarrow 2e^+ 2e^-]$	2.263×10^{-4}	2.274×10^{-4}	4.625×10^{-4}	2.006×10^{-4}
$0^+ : T_0 \rightarrow D_s^+ [\eta \rightarrow \mu^+ \mu^-]$	5.482×10^{-5}	5.51×10^{-5}	1.121×10^{-4}	4.861×10^{-5}
$0^+ : T_0 \rightarrow D_s^+ [\eta \rightarrow 2\mu^+ 2\mu^-]$	4.715×10^{-8}	4.738×10^{-8}	9.637×10^{-8}	4.181×10^{-8}
$0^+ : T_0 \rightarrow D_s^+ [\eta' \rightarrow \pi^+ \pi^- \eta]$	3.655×10^0	3.74×10^0	8.133×10^0	0
$0^+ : T_0 \rightarrow D_s^+ [\eta' \rightarrow \rho^0 \gamma]$	2.537×10^0	2.596×10^0	5.646×10^0	0
$0^+ : T_0 \rightarrow D_s^+ [\eta' \rightarrow \pi^0 \pi^0 \eta]$	1.926×10^0	1.97×10^0	4.284×10^0	0
$0^+ : T_0 \rightarrow D_s^+ [\eta' \rightarrow \omega \gamma]$	2.168×10^{-1}	2.218×10^{-1}	4.824×10^{-1}	0
$0^+ : T_0 \rightarrow D_s^+ [\eta' \rightarrow \gamma\gamma]$	1.985×10^{-1}	2.032×10^{-1}	4.418×10^{-1}	0
$0^+ : T_0 \rightarrow D_s^+ [\eta' \rightarrow \pi^+ \pi^- \pi^0]$	3.103×10^{-2}	3.176×10^{-2}	6.905×10^{-2}	0
$0^+ : T_0 \rightarrow D_s^+ [\eta' \rightarrow \pi^0 \gamma\gamma]$	2.754×10^{-2}	2.818×10^{-2}	6.128×10^{-2}	0
$0^+ : T_0 \rightarrow D_s^+ [\eta' \rightarrow 3\pi^0]$	2.151×10^{-2}	2.201×10^{-2}	4.786×10^{-2}	0
$0^+ : T_0 \rightarrow D_s^+ [\eta' \rightarrow \pi^+ \pi^- e^+ e^-]$	2.09×10^{-2}	2.138×10^{-2}	4.65×10^{-2}	0
$0^+ : T_0 \rightarrow D_s^+ [\eta' \rightarrow \gamma e^+ e^-]$	4.134×10^{-3}	4.23×10^{-3}	9.198×10^{-3}	0
$0^+ : T_0 \rightarrow D_s^+ [\eta' \rightarrow \pi^+ \pi^- 2\pi^0]$	1.815×10^{-3}	1.857×10^{-3}	4.037×10^{-3}	0
$0^+ : T_0 \rightarrow D_s^+ [\eta' \rightarrow \omega e^+ e^-]$	1.696×10^{-3}	1.735×10^{-3}	3.773×10^{-3}	0
$0^+ : T_0 \rightarrow D_s^+ [\eta' \rightarrow \mu^+ \mu^- \gamma]$	9.729×10^{-4}	9.955×10^{-4}	2.165×10^{-3}	0
$0^+ : T_0 \rightarrow D_s^+ [\eta' \rightarrow 2(\pi^+ \pi^-)]$	7.327×10^{-4}	7.497×10^{-4}	1.63×10^{-3}	0
$0^+ : T_0 \rightarrow D_s^+ [\eta' \rightarrow \pi^+ \pi^- \mu^+ \mu^-]$	1.829×10^{-4}	1.872×10^{-4}	4.07×10^{-4}	0
$0^+ : T_0 \rightarrow D_s^+ [\eta' \rightarrow e^+ e^- e^+ e^-]$	3.852×10^{-5}	3.941×10^{-5}	8.57×10^{-5}	0
$0^+ : T_0 \rightarrow D_s^{*+} [\phi \rightarrow K^+ K^-]$	1.332×10^0	1.466×10^0	4.379×10^0	0
$0^+ : T_0 \rightarrow D_s^{*+} [\phi \rightarrow K_L^0 K_S^0]$	8.982×10^{-1}	9.887×10^{-1}	2.953×10^0	0

Continued on next page

Table 10 – continued from previous page

Channel	$\bar{3} - 3$ SR	$\bar{3} - 3$ NR	$6 - \bar{6}$ SR	$6 - \bar{6}$ NR
$0^+ : T_0 \rightarrow D_s^{*+} [\phi \rightarrow \rho\pi/\pi^+\pi^-\pi^0]$	3.979×10^{-1}	4.38×10^{-1}	1.308×10^0	0
$0^+ : T_0 \rightarrow D_s^{*+} [\phi \rightarrow \eta\gamma]$	3.488×10^{-2}	3.839×10^{-2}	1.147×10^{-1}	0
$0^+ : T_0 \rightarrow D_s^{*+} [\phi \rightarrow \pi^0\gamma]$	3.546×10^{-3}	3.903×10^{-3}	1.166×10^{-2}	0
$0^+ : T_0 \rightarrow D_s^{*+} [\phi \rightarrow f_0(980)\gamma]$	8.607×10^{-4}	9.474×10^{-4}	2.83×10^{-3}	0
$0^+ : T_0 \rightarrow D_s^{*+} [\phi \rightarrow e^+e^-]$	7.913×10^{-4}	8.711×10^{-4}	2.602×10^{-3}	0
$0^+ : T_0 \rightarrow D_s^{*+} [\phi \rightarrow \mu^+\mu^-]$	7.642×10^{-4}	8.412×10^{-4}	2.512×10^{-3}	0
$0^+ : T_0 \rightarrow D_s^{*+} [\phi \rightarrow \pi^0\pi^0\gamma]$	3.006×10^{-4}	3.309×10^{-4}	9.882×10^{-4}	0
$0^+ : T_0 \rightarrow D_s^{*+} [\phi \rightarrow \eta e^+e^-]$	2.895×10^{-4}	3.187×10^{-4}	9.518×10^{-4}	0
$0^+ : T_0 \rightarrow D_s^{*+} [\phi \rightarrow \pi^+\pi^-]$	2.537×10^{-4}	2.792×10^{-4}	8.34×10^{-4}	0
$0^+ : T_0 \rightarrow D_s^{*+} [\phi \rightarrow a_0(980)\gamma]$	2.03×10^{-4}	2.235×10^{-4}	6.674×10^{-4}	0
$0^+ : T_0 \rightarrow D_s^{*+} [\phi \rightarrow \pi^0\eta\gamma]$	1.94×10^{-4}	2.136×10^{-4}	6.379×10^{-4}	0
$0^+ : T_0 \rightarrow D_s^{*+} [\phi \rightarrow \eta'\gamma]$	1.664×10^{-4}	1.832×10^{-4}	5.472×10^{-4}	0
$0^+ : T_0 \rightarrow D_s^{*+} [\phi \rightarrow \omega\pi^0]$	1.263×10^{-4}	1.39×10^{-4}	4.153×10^{-4}	0
$0^+ : T_0 \rightarrow D_s^{*+} [\phi \rightarrow \pi^+\pi^-\gamma]$	1.095×10^{-4}	1.205×10^{-4}	3.599×10^{-4}	0
$0^+ : T_0 \rightarrow D_s^{*+} [\phi \rightarrow \mu^+\mu^-\gamma]$	3.818×10^{-5}	4.203×10^{-5}	1.255×10^{-4}	0
$0^+ : T_0 \rightarrow D_s^{*+} [\phi \rightarrow \pi^0 e^+e^-]$	3.546×10^{-5}	3.903×10^{-5}	1.166×10^{-4}	0
$0^+ : T_0 \rightarrow D_s^{*+} [\phi \rightarrow \pi^+\pi^-\pi^+\pi^-]$	1.054×10^{-5}	1.16×10^{-5}	3.466×10^{-5}	0

Table 11: Expanded one-meson spectator-cascade decay rates of the ground-state $1^+ cs\bar{s}\bar{s}$ tetraquark, using daughter branching-fraction inputs from Refs. [3, 75]. Only one daughter meson decays in each row; all rates are in MeV.

Channel	$\bar{3} - 3$ SR	$\bar{3} - 3$ NR	$6 - \bar{6}$ SR
D_s^+ daughter decays; hidden-strange meson kept on shell			
$1^+ : T_1 \rightarrow [D_s^+ \rightarrow \eta e^+\nu_e] \phi$	1.584×10^{-1}	1.701×10^{-1}	3.516×10^{-1}
$1^+ : T_1 \rightarrow [D_s^+ \rightarrow \eta \mu^+\nu_\mu] \phi$	1.555×10^{-1}	1.669×10^{-1}	3.451×10^{-1}
$1^+ : T_1 \rightarrow [D_s^+ \rightarrow \eta' e^+\nu_e] \phi$	3.05×10^{-2}	3.32×10^{-2}	6.769×10^{-2}
$1^+ : T_1 \rightarrow [D_s^+ \rightarrow \eta' \mu^+\nu_\mu] \phi$	2.914×10^{-2}	3.176×10^{-2}	6.467×10^{-2}
$1^+ : T_1 \rightarrow [D_s^+ \rightarrow K^0 e^+\nu_e] \phi$	1.656×10^{-2}	1.778×10^{-2}	3.676×10^{-2}
$1^+ : T_1 \rightarrow [D_s^+ \rightarrow K^0 \mu^+\nu_\mu] \phi$	1.629×10^{-2}	1.749×10^{-2}	3.615×10^{-2}
$1^+ : T_1 \rightarrow [D_s^+ \rightarrow \phi e^+\nu_e] \phi$	1.686×10^{-1}	1.847×10^{-1}	3.742×10^{-1}
$1^+ : T_1 \rightarrow [D_s^+ \rightarrow \phi \mu^+\nu_\mu] \phi$	1.593×10^{-1}	1.748×10^{-1}	3.534×10^{-1}
$1^+ : T_1 \rightarrow [D_s^+ \rightarrow K^{*0} e^+\nu_e] \phi$	1.227×10^{-2}	1.335×10^{-2}	2.723×10^{-2}
$1^+ : T_1 \rightarrow [D_s^+ \rightarrow K^{*0} \mu^+\nu_\mu] \phi$	1.17×10^{-2}	1.275×10^{-2}	2.597×10^{-2}
$1^+ : T_1 \rightarrow [D_s^+ \rightarrow f_0(980) e^+\nu_e] \phi$	2.847×10^{-2}	3.105×10^{-2}	6.318×10^{-2}
$1^+ : T_1 \rightarrow [D_s^+ \rightarrow f_0(980) \mu^+\nu_\mu] \phi$	2.71×10^{-2}	2.96×10^{-2}	6.014×10^{-2}
$1^+ : T_1 \rightarrow [D_s^+ \rightarrow K_0^{*+}(1430) e^+\nu_e] \phi$	1.393×10^{-4}	1.598×10^{-4}	3.092×10^{-4}
$1^+ : T_1 \rightarrow [D_s^+ \rightarrow K_0^{*+}(1430) \mu^+\nu_\mu] \phi$	1.168×10^{-4}	1.351×10^{-4}	2.592×10^{-4}
$1^+ : T_1 \rightarrow [D_s^+ \rightarrow f_1(1420) e^+\nu_e] \phi$	3.022×10^{-3}	3.474×10^{-3}	6.706×10^{-3}
$1^+ : T_1 \rightarrow [D_s^+ \rightarrow f_1(1420) \mu^+\nu_\mu] \phi$	2.53×10^{-3}	2.933×10^{-3}	5.614×10^{-3}
$1^+ : T_1 \rightarrow [D_s^+ \rightarrow K_1(1270) e^+\nu_e] \phi$	3.847×10^{-4}	4.313×10^{-4}	8.537×10^{-4}
$1^+ : T_1 \rightarrow [D_s^+ \rightarrow K_1(1270) \mu^+\nu_\mu] \phi$	3.459×10^{-4}	3.894×10^{-4}	7.677×10^{-4}
$1^+ : T_1 \rightarrow [D_s^+ \rightarrow K_1(1400) e^+\nu_e] \phi$	8.589×10^{-5}	9.822×10^{-5}	1.906×10^{-4}
$1^+ : T_1 \rightarrow [D_s^+ \rightarrow K_1(1400) \mu^+\nu_\mu] \phi$	7.331×10^{-5}	8.453×10^{-5}	1.627×10^{-4}
$1^+ : T_1 \rightarrow [D_s^+ \rightarrow f_2'(1525) e^+\nu_e] \phi$	8.52×10^{-6}	1.049×10^{-5}	1.891×10^{-5}
$1^+ : T_1 \rightarrow [D_s^+ \rightarrow f_2'(1525) \mu^+\nu_\mu] \phi$	4.517×10^{-6}	5.728×10^{-6}	1.003×10^{-5}
$1^+ : T_1 \rightarrow [D_s^+ \rightarrow K_2^+(1430) e^+\nu_e] \phi$	1.379×10^{-6}	1.637×10^{-6}	3.061×10^{-6}
$1^+ : T_1 \rightarrow [D_s^+ \rightarrow K_2^+(1430) \mu^+\nu_\mu] \phi$	8.755×10^{-7}	1.057×10^{-6}	1.943×10^{-6}
$1^+ : T_1 \rightarrow [D_s^+ \rightarrow D^0 e^+\nu_e] \phi$	4.884×10^{-9}	9.14×10^{-9}	1.084×10^{-8}
$1^+ : T_1 \rightarrow [D_s^+ \rightarrow \eta \pi^+] \phi$	2.404×10^{-1}	2.519×10^{-1}	5.336×10^{-1}
$1^+ : T_1 \rightarrow [D_s^+ \rightarrow \eta \rho^+] \phi$	4.471×10^{-1}	4.747×10^{-1}	9.922×10^{-1}
$1^+ : T_1 \rightarrow [D_s^+ \rightarrow \eta' \pi^+] \phi$	9.692×10^{-2}	1.025×10^{-1}	2.151×10^{-1}
$1^+ : T_1 \rightarrow [D_s^+ \rightarrow \eta' \rho^+] \phi$	8.411×10^{-2}	9.405×10^{-2}	1.867×10^{-1}
$1^+ : T_1 \rightarrow [D_s^+ \rightarrow \phi \pi^+] \phi$	2.194×10^{-1}	2.327×10^{-1}	4.869×10^{-1}
$1^+ : T_1 \rightarrow [D_s^+ \rightarrow \phi \rho^+] \phi$	8.296×10^{-1}	8.94×10^{-1}	1.841×10^0
$1^+ : T_1 \rightarrow [D_s^+ \rightarrow K^0 \pi^+] \phi$	2.276×10^{-2}	2.383×10^{-2}	5.05×10^{-2}
$1^+ : T_1 \rightarrow [D_s^+ \rightarrow K^0 \rho^+] \phi$	4.466×10^{-2}	4.732×10^{-2}	9.912×10^{-2}
$1^+ : T_1 \rightarrow [D_s^+ \rightarrow K^{*0} \pi^+] \phi$	1.094×10^{-2}	1.156×10^{-2}	2.429×10^{-2}
$1^+ : T_1 \rightarrow [D_s^+ \rightarrow K^{*0} \rho^+] \phi$	4.938×10^{-2}	5.245×10^{-2}	1.096×10^{-1}
$1^+ : T_1 \rightarrow [D_s^+ \rightarrow f_0(980) \pi^+] \phi$	9.68×10^{-2}	1.025×10^{-1}	2.148×10^{-1}
$1^+ : T_1 \rightarrow [D_s^+ \rightarrow K_0^+(1430) \pi^+] \phi$	1.591×10^{-3}	1.739×10^{-3}	3.532×10^{-3}
$1^+ : T_1 \rightarrow [D_s^+ \rightarrow f_1(1420) \pi^+] \phi$	1.163×10^{-2}	1.275×10^{-2}	2.581×10^{-2}
$1^+ : T_1 \rightarrow [D_s^+ \rightarrow K_1(1270) \pi^+] \phi$	9.083×10^{-4}	9.781×10^{-4}	2.016×10^{-3}
$1^+ : T_1 \rightarrow [D_s^+ \rightarrow K_1(1400) \pi^+] \phi$	3.264×10^{-4}	3.568×10^{-4}	7.245×10^{-4}
$1^+ : T_1 \rightarrow [D_s^+ \rightarrow f_2'(1525) \pi^+] \phi$	2.828×10^{-4}	3.36×10^{-4}	6.276×10^{-4}
$1^+ : T_1 \rightarrow [D_s^+ \rightarrow K_2^+(1430) \pi^+] \phi$	3.207×10^{-5}	3.684×10^{-5}	7.117×10^{-5}

Continued on next page

Table 11 – continued from previous page

Channel	$\bar{3} - 3$ SR	$\bar{3} - 3$ NR	$6 - \bar{6}$ SR
D_s^{*+} daughter feed-down; hidden-strange meson kept on shell			
$1^+ : T_1 \rightarrow [D_s^{*+} \rightarrow D_s^+ \gamma] \eta$	2.344×10^0	2.361×10^0	4.84×10^0
$1^+ : T_1 \rightarrow [D_s^{*+} \rightarrow D_s^+ \pi^0] \eta$	1.443×10^{-1}	1.453×10^{-1}	2.98×10^{-1}
$1^+ : T_1 \rightarrow [D_s^{*+} \rightarrow D_s^+ \gamma] \eta'$	2.094×10^0	2.14×10^0	4.588×10^0
$1^+ : T_1 \rightarrow [D_s^{*+} \rightarrow D_s^+ \pi^0] \eta'$	1.289×10^{-1}	1.317×10^{-1}	2.824×10^{-1}
Hidden-strange daughter decays; $D_s^{(*)}$ meson kept on shell			
$1^+ : T_1 \rightarrow D_s^{*+} [\eta \rightarrow \gamma\gamma]$	9.859×10^{-1}	9.93×10^{-1}	2.036×10^0
$1^+ : T_1 \rightarrow D_s^{*+} [\eta \rightarrow 3\pi^0]$	8.157×10^{-1}	8.215×10^{-1}	1.684×10^0
$1^+ : T_1 \rightarrow D_s^{*+} [\eta \rightarrow \pi^+ \pi^- \pi^0]$	5.766×10^{-1}	5.808×10^{-1}	1.191×10^0
$1^+ : T_1 \rightarrow D_s^{*+} [\eta \rightarrow \pi^+ \pi^- \gamma]$	1.071×10^{-1}	1.079×10^{-1}	2.212×10^{-1}
$1^+ : T_1 \rightarrow D_s^{*+} [\eta \rightarrow e^+ e^- \gamma]$	1.755×10^{-2}	1.767×10^{-2}	3.623×10^{-2}
$1^+ : T_1 \rightarrow D_s^{*+} [\eta \rightarrow \mu^+ \mu^- \gamma]$	7.769×10^{-4}	7.825×10^{-4}	1.604×10^{-3}
$1^+ : T_1 \rightarrow D_s^{*+} [\eta \rightarrow \pi^0 \gamma\gamma]$	6.397×10^{-4}	6.443×10^{-4}	1.321×10^{-3}
$1^+ : T_1 \rightarrow D_s^{*+} [\eta \rightarrow \pi^+ \pi^- e^+ e^- (\gamma)]$	6.714×10^{-4}	6.762×10^{-4}	1.386×10^{-3}
$1^+ : T_1 \rightarrow D_s^{*+} [\eta \rightarrow 2e^+ 2e^-]$	6.012×10^{-5}	6.055×10^{-5}	1.242×10^{-4}
$1^+ : T_1 \rightarrow D_s^{*+} [\eta \rightarrow \mu^+ \mu^-]$	1.457×10^{-5}	1.467×10^{-5}	3.008×10^{-5}
$1^+ : T_1 \rightarrow D_s^{*+} [\eta \rightarrow 2\mu^+ 2\mu^-]$	1.253×10^{-8}	1.262×10^{-8}	2.587×10^{-8}
$1^+ : T_1 \rightarrow D_s^{*+} [\eta' \rightarrow \pi^+ \pi^- \eta]$	9.504×10^{-1}	9.713×10^{-1}	2.082×10^0
$1^+ : T_1 \rightarrow D_s^{*+} [\eta' \rightarrow \rho^0 \gamma]$	6.598×10^{-1}	6.742×10^{-1}	1.445×10^0
$1^+ : T_1 \rightarrow D_s^{*+} [\eta' \rightarrow \pi^0 \pi^0 \eta]$	5.007×10^{-1}	5.116×10^{-1}	1.097×10^0
$1^+ : T_1 \rightarrow D_s^{*+} [\eta' \rightarrow \omega \gamma]$	5.638×10^{-2}	5.761×10^{-2}	1.235×10^{-1}
$1^+ : T_1 \rightarrow D_s^{*+} [\eta' \rightarrow \gamma\gamma]$	5.163×10^{-2}	5.276×10^{-2}	1.131×10^{-1}
$1^+ : T_1 \rightarrow D_s^{*+} [\eta' \rightarrow \pi^+ \pi^- \pi^0]$	8.07×10^{-3}	8.246×10^{-3}	1.768×10^{-2}
$1^+ : T_1 \rightarrow D_s^{*+} [\eta' \rightarrow \pi^0 \gamma\gamma]$	7.162×10^{-3}	7.318×10^{-3}	1.569×10^{-2}
$1^+ : T_1 \rightarrow D_s^{*+} [\eta' \rightarrow 3\pi^0]$	5.594×10^{-3}	5.716×10^{-3}	1.225×10^{-2}
$1^+ : T_1 \rightarrow D_s^{*+} [\eta' \rightarrow \pi^+ \pi^- e^+ e^-]$	5.434×10^{-3}	5.553×10^{-3}	1.19×10^{-2}
$1^+ : T_1 \rightarrow D_s^{*+} [\eta' \rightarrow \gamma e^+ e^-]$	1.075×10^{-3}	1.099×10^{-3}	2.355×10^{-3}
$1^+ : T_1 \rightarrow D_s^{*+} [\eta' \rightarrow \pi^+ \pi^- 2\pi^0]$	4.718×10^{-4}	4.822×10^{-4}	1.034×10^{-3}
$1^+ : T_1 \rightarrow D_s^{*+} [\eta' \rightarrow \omega e^+ e^-]$	4.409×10^{-4}	4.505×10^{-4}	9.659×10^{-4}
$1^+ : T_1 \rightarrow D_s^{*+} [\eta' \rightarrow \mu^+ \mu^- \gamma]$	2.53×10^{-4}	2.585×10^{-4}	5.542×10^{-4}
$1^+ : T_1 \rightarrow D_s^{*+} [\eta' \rightarrow 2(\pi^+ \pi^-)]$	1.905×10^{-4}	1.947×10^{-4}	4.174×10^{-4}
$1^+ : T_1 \rightarrow D_s^{*+} [\eta' \rightarrow \pi^+ \pi^- \mu^+ \mu^-]$	4.757×10^{-5}	4.861×10^{-5}	1.042×10^{-4}
$1^+ : T_1 \rightarrow D_s^{*+} [\eta' \rightarrow e^+ e^- e^+ e^-]$	1.002×10^{-5}	1.023×10^{-5}	2.194×10^{-5}
$1^+ : T_1 \rightarrow D_s^+ [\phi \rightarrow K^+ K^-]$	2.866×10^0	2.932×10^0	6.361×10^0
$1^+ : T_1 \rightarrow D_s^+ [\phi \rightarrow K_L^0 K_S^0]$	1.933×10^0	1.977×10^0	4.289×10^0
$1^+ : T_1 \rightarrow D_s^+ [\phi \rightarrow \rho\pi/\pi^+ \pi^- \pi^0]$	8.561×10^{-1}	8.759×10^{-1}	1.9×10^0
$1^+ : T_1 \rightarrow D_s^+ [\phi \rightarrow \eta\gamma]$	7.504×10^{-2}	7.678×10^{-2}	1.665×10^{-1}
$1^+ : T_1 \rightarrow D_s^+ [\phi \rightarrow \pi^0 \gamma]$	7.629×10^{-3}	7.806×10^{-3}	1.693×10^{-2}
$1^+ : T_1 \rightarrow D_s^+ [\phi \rightarrow f_0(980)\gamma]$	1.852×10^{-3}	1.895×10^{-3}	4.11×10^{-3}
$1^+ : T_1 \rightarrow D_s^+ [\phi \rightarrow e^+ e^-]$	1.703×10^{-3}	1.742×10^{-3}	3.779×10^{-3}
$1^+ : T_1 \rightarrow D_s^+ [\phi \rightarrow \mu^+ \mu^-]$	1.644×10^{-3}	1.682×10^{-3}	3.649×10^{-3}
$1^+ : T_1 \rightarrow D_s^+ [\phi \rightarrow \pi^0 \pi^0 \gamma]$	6.468×10^{-4}	6.618×10^{-4}	1.435×10^{-3}
$1^+ : T_1 \rightarrow D_s^+ [\phi \rightarrow \eta e^+ e^-]$	6.229×10^{-4}	6.373×10^{-4}	1.382×10^{-3}
$1^+ : T_1 \rightarrow D_s^+ [\phi \rightarrow \rho\pi/\pi^+ \pi^-]$	5.458×10^{-4}	5.585×10^{-4}	1.211×10^{-3}
$1^+ : T_1 \rightarrow D_s^+ [\phi \rightarrow a_0(980)\gamma]$	4.368×10^{-4}	4.469×10^{-4}	9.694×10^{-4}
$1^+ : T_1 \rightarrow D_s^+ [\phi \rightarrow \pi^0 \eta\gamma]$	4.175×10^{-4}	4.271×10^{-4}	9.265×10^{-4}
$1^+ : T_1 \rightarrow D_s^+ [\phi \rightarrow \eta' \gamma]$	3.581×10^{-4}	3.664×10^{-4}	7.948×10^{-4}
$1^+ : T_1 \rightarrow D_s^+ [\phi \rightarrow \omega\pi^0]$	2.718×10^{-4}	2.781×10^{-4}	6.032×10^{-4}
$1^+ : T_1 \rightarrow D_s^+ [\phi \rightarrow \pi^+ \pi^- \gamma]$	2.355×10^{-4}	2.41×10^{-4}	5.228×10^{-4}
$1^+ : T_1 \rightarrow D_s^+ [\phi \rightarrow \mu^+ \mu^- \gamma]$	8.215×10^{-5}	8.406×10^{-5}	1.823×10^{-4}
$1^+ : T_1 \rightarrow D_s^+ [\phi \rightarrow \pi^0 e^+ e^-]$	7.63×10^{-5}	7.807×10^{-5}	1.693×10^{-4}
$1^+ : T_1 \rightarrow D_s^+ [\phi \rightarrow \pi^+ \pi^- \pi^+ \pi^-]$	2.268×10^{-5}	2.321×10^{-5}	5.034×10^{-5}

Table 12: Expanded one-meson spectator-cascade decay rates of the ground-state $2^+ c\bar{s}\bar{s}\bar{s}$ tetraquark, using daughter branching-fraction inputs from Refs. [3, 75]. Only one daughter meson decays in each row; all rates are in MeV.

Channel	$\bar{3} - 3$ SR	$\bar{3} - 3$ NR	$6 - \bar{6}$ SR
D_s^{*+} daughter feed-down; hidden-strange meson kept on shell			
$2^+ : T_2 \rightarrow [D_s^{*+} \rightarrow D_s^+ \gamma] \phi$	4.844×10^0	4.878×10^0	8.709×10^0
$2^+ : T_2 \rightarrow [D_s^{*+} \rightarrow D_s^+ \pi^0] \phi$	2.982×10^{-1}	3.003×10^{-1}	5.361×10^{-1}
Hidden-strange daughter decays; $D_s^{(*)}$ meson kept on shell			
$2^+ : T_2 \rightarrow D_s^{*+} [\phi \rightarrow K^+ K^-]$	2.583×10^0	2.601×10^0	4.643×10^0
$2^+ : T_2 \rightarrow D_s^{*+} [\phi \rightarrow K_L^0 K_S^0]$	1.742×10^0	1.754×10^0	3.131×10^0

Continued on next page

Table 12 – continued from previous page

Channel	$\bar{\mathbf{3}} - \mathbf{3}$ SR	$\bar{\mathbf{3}} - \mathbf{3}$ NR	$\mathbf{6} - \bar{\mathbf{6}}$ SR
$2^+ : T_2 \rightarrow D_s^{*+} [\phi \rightarrow \rho\pi/\pi^+\pi^-\pi^0]$	7.715×10^{-1}	7.768×10^{-1}	1.387×10^0
$2^+ : T_2 \rightarrow D_s^{*+} [\phi \rightarrow \eta\gamma]$	6.762×10^{-2}	6.809×10^{-2}	1.216×10^{-1}
$2^+ : T_2 \rightarrow D_s^{*+} [\phi \rightarrow \pi^0\gamma]$	6.875×10^{-3}	6.923×10^{-3}	1.236×10^{-2}
$2^+ : T_2 \rightarrow D_s^{*+} [\phi \rightarrow f_0(980)\gamma]$	1.669×10^{-3}	1.68×10^{-3}	3×10^{-3}
$2^+ : T_2 \rightarrow D_s^{*+} [\phi \rightarrow e^+e^-]$	1.534×10^{-3}	1.545×10^{-3}	2.758×10^{-3}
$2^+ : T_2 \rightarrow D_s^{*+} [\phi \rightarrow \mu^+\mu^-]$	1.482×10^{-3}	1.492×10^{-3}	2.664×10^{-3}
$2^+ : T_2 \rightarrow D_s^{*+} [\phi \rightarrow \pi^0\pi^0\gamma]$	5.828×10^{-4}	5.869×10^{-4}	1.048×10^{-3}
$2^+ : T_2 \rightarrow D_s^{*+} [\phi \rightarrow \eta e^+e^-]$	5.613×10^{-4}	5.652×10^{-4}	1.009×10^{-3}
$2^+ : T_2 \rightarrow D_s^{*+} [\phi \rightarrow \pi^+\pi^-]$	4.919×10^{-4}	4.953×10^{-4}	8.843×10^{-4}
$2^+ : T_2 \rightarrow D_s^{*+} [\phi \rightarrow a_0(980)\gamma]$	3.936×10^{-4}	3.964×10^{-4}	7.076×10^{-4}
$2^+ : T_2 \rightarrow D_s^{*+} [\phi \rightarrow \pi^0\eta\gamma]$	3.762×10^{-4}	3.788×10^{-4}	6.763×10^{-4}
$2^+ : T_2 \rightarrow D_s^{*+} [\phi \rightarrow \eta'\gamma]$	3.227×10^{-4}	3.249×10^{-4}	5.801×10^{-4}
$2^+ : T_2 \rightarrow D_s^{*+} [\phi \rightarrow \omega\pi^0]$	2.449×10^{-4}	2.466×10^{-4}	4.403×10^{-4}
$2^+ : T_2 \rightarrow D_s^{*+} [\phi \rightarrow \pi^+\pi^-\gamma]$	2.123×10^{-4}	2.137×10^{-4}	3.816×10^{-4}
$2^+ : T_2 \rightarrow D_s^{*+} [\phi \rightarrow \mu^+\mu^-\gamma]$	7.403×10^{-5}	7.455×10^{-5}	1.331×10^{-4}
$2^+ : T_2 \rightarrow D_s^{*+} [\phi \rightarrow \pi^0 e^+e^-]$	6.876×10^{-5}	6.924×10^{-5}	1.236×10^{-4}
$2^+ : T_2 \rightarrow D_s^{*+} [\phi \rightarrow \pi^+\pi^-\pi^+\pi^-]$	2.044×10^{-5}	2.058×10^{-5}	3.675×10^{-5}

The $\mathbf{6} - \bar{\mathbf{6}}$ NR axial-vector and tensor cases are threshold closed and are therefore omitted from Tables 11 and 12.

6 Results and Discussion

The present work connects the charm–strange meson sector with the open-flavor compact tetraquark system $cs\bar{s}\bar{s}$. The analysis is not limited to the mass spectrum. It first fixes the D_s meson spectrum and weak-decay inputs, then constructs the $[cs]$ and $[ss]$ diquark building blocks, predicts the compact tetraquark spectrum in the $\bar{\mathbf{3}} - \mathbf{3}$ and $\mathbf{6} - \bar{\mathbf{6}}$ color configurations, compares the tetraquark levels with two-meson thresholds, studies Regge behavior, evaluates primary rearrangement widths, and finally translates the primary two-body decays into one-daughter spectator-cascade modes. The discussion is therefore organized into two parts: the meson sector, which supplies the reference masses, form factors, and daughter branching fractions, and the tetraquark sector, where the spectroscopy and decay phenomenology of the $cs\bar{s}\bar{s}$ system are interpreted.

6.1 The D_s meson sector

The calculated D_s spectrum in Table 1 provides the numerical base for the full analysis. In the ground S -wave sector, the 1^1S_0 mass is obtained as 1967.87 ± 19.58 MeV in the semi-relativistic scheme and 2003.55 ± 19.75 MeV in the non-relativistic scheme, while the vector 1^3S_1 state lies at 2113.05 ± 29.72 MeV and 2128.65 ± 29.80 MeV, respectively. The semi-relativistic masses are generally lower than the non-relativistic masses because the semi-relativistic Hamiltonian retains the higher-order kinetic-energy correction through $\mathcal{O}(p^6)$. The effect is moderate for the lowest states but becomes more visible for radial and orbital excitations, where the SR–NR separation is typically several tens of MeV.

For the P -wave D_s states, the lowest scalar, axial-vector, and tensor levels occur in the range 2.38–2.53 GeV. The 1^3P_0 mass is 2382.74 ± 22.79 MeV in the SR treatment and 2402.32 ± 22.96 MeV in the NR treatment. The 1^1P_1 and 1^3P_1 states lie close to each other near 2.47–2.50 GeV, which is relevant because physical heavy-light axial states can involve 1^1P_1 – 3^3P_1 mixing. The tensor 1^3P_2 state appears at 2512.02 ± 26.36 MeV (SR) and 2531.59 ± 26.56 MeV (NR). The lowest D -wave states cluster around 2.73–2.77 GeV, and the lowest F -wave states cluster around 2.94–3.00 GeV. Thus the calculated spectrum gives a smooth charm–strange tower from the ground states to high orbital excitations.

The present meson masses are consistent with the broad pattern of other theoretical calculations. The low-lying $1S$ values agree closely with the relativistic independent-quark-model results of Shah *et al.* [78] and with the relativized quark-model values of Godfrey and Moats [49]. The scalar 1^3P_0 entry is

comparatively low and remains closer to the light $D_{s0}^*(2317)$ region than many conventional quark-model predictions. For radial and orbital excitations, especially in the D -wave sector, the present values are generally lower than the Godfrey–Moats spectrum by several tens to a few hundred MeV. This difference reflects the sensitivity of excited heavy-light states to the kinetic-energy expansion and the confinement prescription, while the ordering of the S , P , D , and F multiplets remains conventional.

The weak-decay block of the D_s meson is summarized in Table 8 and in Figs. 7 and 8. The form-factor panels show smooth semi-relativistic behavior over the physical q^2 intervals for pseudoscalar, vector, scalar, axial-vector, and tensor final states. The differential-width plots display the expected relation between electron and muon modes: for most channels the two curves are close over much of the phase space, while the muon distribution is more suppressed near endpoints because of the finite lepton mass. Among the semileptonic modes, the largest branching fractions are obtained for $D_s^+ \rightarrow \eta \ell^+ \nu_\ell$ and $D_s^+ \rightarrow \phi \ell^+ \nu_\ell$, both at the few-percent level. The η' and $f_0(980)$ modes are smaller but still important, whereas transitions into higher scalar, axial-vector, and tensor strange states are suppressed by phase space and by the corresponding form factors.

The nonleptonic entries in Table 8 are important for the tetraquark part of the work because they are used as daughter branching-fraction inputs in the spectator-cascade tables. The largest factorized nonleptonic benchmark is $D_s^+ \rightarrow \phi \rho^+$, with branching fractions of order 10^{-1} , followed by $D_s^+ \rightarrow \eta \rho^+$, $D_s^+ \rightarrow \phi \pi^+$, and the corresponding η' and $f_0(980)$ channels. In contrast, the spectator- c transition $D_s^+ \rightarrow D^0 e^+ \nu_e$ is strongly suppressed, at the 10^{-9} level, because the available phase space for the $\bar{s} \rightarrow \bar{u}$ transition inside the charged D_s meson is very small.

The mesonic decay results can be compared directly with the PDG 2025 averages by using $\Gamma_{D_s} = \hbar/\tau_{D_s} = 1.31327 \times 10^{-12}$ GeV and converting each branching fraction through $\Gamma_i = \mathcal{B}_i \Gamma_{D_s}$. With the semi-relativistic corrected values, the present semileptonic widths for $D_s^+ \rightarrow \eta e^+ \nu_e$ and $D_s^+ \rightarrow \eta \mu^+ \nu_\mu$ are 3.622×10^{-14} and 3.555×10^{-14} GeV, respectively. The corresponding PDG 2025 values are $(2.981 \pm 0.079) \times 10^{-14}$ and $(2.942 \pm 0.092) \times 10^{-14}$ GeV, so both channels are higher by about 21% in the present calculation. For the η' modes the trend is reversed: the calculated widths 0.697×10^{-14} and 0.666×10^{-14} GeV for $e^+ \nu_e$ and $\mu^+ \nu_\mu$ are about two thirds of the PDG values $(1.064 \pm 0.053) \times 10^{-14}$ and $(1.051 \pm 0.079) \times 10^{-14}$ GeV. This opposite behavior of the η and η' channels shows that the comparison is sensitive to the adopted η – η' strange-component mixing and to the assumed pole shapes of the form factors [3, 79–83]. The additional CLEO-c and BESIII measurements are useful here because they separate the η , η' , K^0 , K^{*0} , $f_0(980)$, and ϕ modes in the same experimental environment, making the pattern of channel-by-channel deviations more meaningful than a comparison with inclusive semileptonic rates alone [80, 82, 83].

For vector and open-strangeness semileptonic modes, the $\phi \ell \nu$ channels are also moderately high, whereas the $K^{(*)}$ channels are close to the experimental scale. The predicted $D_s^+ \rightarrow \phi e^+ \nu_e$ and $D_s^+ \rightarrow \phi \mu^+ \nu_\mu$ widths are 3.854×10^{-14} and 3.640×10^{-14} GeV, compared with the PDG values $(3.073 \pm 0.158) \times 10^{-14}$ and $(2.942 \pm 0.144) \times 10^{-14}$ GeV, corresponding to ratios of about 1.25 and 1.24. In contrast, $D_s^+ \rightarrow K^0 e^+ \nu_e$ gives 0.379×10^{-14} GeV against the PDG value $(0.378 \pm 0.034) \times 10^{-14}$ GeV, while $D_s^+ \rightarrow K^{*0} e^+ \nu_e$ gives 0.281×10^{-14} GeV against $(0.269 \pm 0.026) \times 10^{-14}$ GeV. These two modes therefore provide the best normalization check of the semileptonic block. The $D_s^+ \rightarrow f_0(980) e^+ \nu_e$ entry is less direct: the model gives 0.651×10^{-14} GeV for the parent transition, while the PDG comparison value $(0.215 \pm 0.017) \times 10^{-14}$ GeV is quoted for the specified $f_0(980) \rightarrow \pi^+ \pi^-$ final-state convention. This difference should therefore be interpreted as a line-shape and daughter-branching convention issue rather than only as a form-factor discrepancy [80, 82–87]. The same convention issue appears in earlier $D_s^+ \rightarrow K^+ K^- e^+ \nu_e$ and $D_s^+ \rightarrow f_0(980) e^+ \nu_e$ analyses, where the quoted rates depend on the selected $K^+ K^-$ or $\pi^+ \pi^-$ mass window and on how the ϕ and scalar components are separated [82, 86, 87].

The factorized nonleptonic channels show a wider spread, as expected for modes that can receive

nonfactorizable and resonance-substructure contributions. The present widths for $D_s^+ \rightarrow \eta\rho^+$ and $D_s^+ \rightarrow \phi\pi^+$ are 10.220×10^{-14} and 5.015×10^{-14} GeV, close to the PDG-based widths $(11.688 \pm 1.051) \times 10^{-14}$ and $(5.910 \pm 0.525) \times 10^{-14}$ GeV. The $K^{*0}\pi^+$ channel is also reasonable, with 0.250×10^{-14} GeV compared with $(0.221 \pm 0.034) \times 10^{-14}$ GeV. By contrast, $D_s^+ \rightarrow \eta\pi^+$ is overestimated, 5.496×10^{-14} versus $(2.214 \pm 0.035) \times 10^{-14}$ GeV, whereas the $\eta'\pi^+$ and $\eta'\rho^+$ modes are underestimated, 2.215×10^{-14} and 1.923×10^{-14} GeV compared with $(5.187 \pm 0.105) \times 10^{-14}$ and $(7.617 \pm 1.970) \times 10^{-14}$ GeV. The largest overestimates occur in the vector-vector or resonance-dominated channels $D_s^+ \rightarrow \phi\rho^+$ and $D_s^+ \rightarrow K^{*0}\rho^+$, where the present widths, 18.964×10^{-14} and 1.129×10^{-14} GeV, exceed the PDG-based values $(7.341 \pm 0.447) \times 10^{-14}$ and $(0.512 \pm 0.053) \times 10^{-14}$ GeV. These deviations indicate the expected limitation of a simple factorized treatment once broad resonances, final-state interactions, and amplitude-analysis conventions become important [88–100]. In particular, the Dalitz-plot studies of $D_s^+ \rightarrow K^+K^-\pi^+$ and the absolute double-tag measurements show that modes such as $\phi\pi^+$, K^*K , $f_0(980)\pi^+$, and nonresonant components are not independent narrow two-body channels; this is why the factorized widths in Table 8 are treated as reconstruction-scale estimates rather than as precision amplitude-analysis predictions [88, 89, 95, 96].

The D_s^{*+} modes are treated differently because the PDG 2025 listing gives only an upper limit on the total width, $\Gamma_{D_s^{*+}} < 1.9$ MeV at 90% C.L. The measured branching pattern is nevertheless useful for the cascade analysis: $D_s^{*+} \rightarrow D_s^+\gamma$ dominates with $(93.6 \pm 0.4)\%$, while $D_s^{*+} \rightarrow D_s^+\pi^0$ contributes $(5.77 \pm 0.35)\%$. The Dalitz and leptonic modes are much smaller, with $\mathcal{B}(D_s^{*+} \rightarrow D_s^+e^+e^-) = (6.7 \pm 1.6) \times 10^{-3}$ and $\mathcal{B}(D_s^{*+} \rightarrow e^+\nu_e) = (2.1_{-0.9}^{+1.2}) \times 10^{-5}$. Using the width limit, these correspond to partial-width upper bounds of 1.78 MeV, 0.110 MeV, 1.27×10^{-2} MeV, and 3.99×10^{-5} MeV, respectively. Thus the tetraquark spectator-cascade tables should be read with $D_s^+\gamma$ as the dominant D_s^{*+} feed-down tag and $D_s^+\pi^0$ as the main subleading tag [101–106]. The older Mark-III and CLEO measurements mainly constrain the mass splitting and total-width limit, while the BABAR and BESIII ratios fix the relative importance of the electromagnetic and isospin-violating feed-down paths used in the cascade tables [101, 102, 105, 106].

The Regge analysis of the mesons, summarized in Table 5 and Figs. 1–2, shows that the calculated D_s trajectories are approximately linear in both the orbital and radial planes. The orbital slopes lie mostly between 0.61 and 0.78 GeV^{-2} , while the radial slopes lie near 0.42–0.49 GeV^{-2} . The SR/NR slope ratios remain close to unity for most trajectories, which means that the semi-relativistic correction shifts the absolute masses without destroying the global trajectory pattern. This stability is useful because the meson slopes provide the baseline against which the tetraquark orbital and radial slopes are compared.

6.2 The $cs\bar{s}\bar{s}$ tetraquark sector

The central phenomenology of the paper is the compact $cs\bar{s}\bar{s}$ tetraquark. The calculation begins with the axial-vector diquark inputs in Table 2, because the Pauli-allowed $[\bar{s}\bar{s}]$ antidiquark forces the lowest compact basis toward the axial $[cs][\bar{s}\bar{s}]$ construction. The $[cs]$ subsystem is heavier than the $[ss]$ subsystem, as expected from the charm-quark mass. In the attractive color-antitriplet channel, the $[cs]$ mass is 2214.23 ± 21.39 MeV (SR) and 2225.75 ± 21.34 MeV (NR), while the $[ss]$ mass is 1317.32 ± 12.81 MeV (SR) and 1329.08 ± 12.64 MeV (NR). The sextet diquark masses are slightly larger: 2257.53 ± 38.28 MeV and 2259.37 ± 38.26 MeV for $[cs]$, and 1337.93 ± 12.81 MeV and 1340.16 ± 12.76 MeV for $[ss]$. These values quantify the color dependence of the two-quark building blocks before they are combined into the compact tetraquark.

The resulting $cs\bar{s}\bar{s}$ spectrum is presented in Table 3. For the ground positive-parity spin multiplet in the $\bar{\mathbf{3}} - \mathbf{3}$ color configuration, the predicted SR masses are 3345.41 ± 41.76 MeV for 1^1S_0 , 3451.20 ± 73.29 MeV for 1^3S_1 , and 3656.37 ± 48.09 MeV for 1^5S_2 . The corresponding NR values are 3379.82 ± 41.80 MeV,

3474.11 \pm 72.90 MeV, and 3662.70 \pm 48.32 MeV. The $\bar{\mathbf{3}} - \mathbf{3}$ ground multiplet is therefore located between about 3.35 and 3.66 GeV, with the tensor state the heaviest. This ordering is consistent with a positive spin-dependent shift when the total spin of the axial-vector diquark–antidiquark pair increases from $S_T = 0$ to $S_T = 2$.

The $\mathbf{6} - \bar{\mathbf{6}}$ configuration is more sensitive to the details of the model. In the SR calculation the three ground S -wave entries are centered near 3564.42 MeV, whereas the NR central values are close to 2595.46 MeV. This large SR–NR separation is one of the most important features of the tetraquark spectrum and indicates that the sextet–antisextet configuration should not be interpreted from the central mass alone. Instead, its physical relevance must be judged together with the threshold offsets in Table 4 and the open-channel pattern in Table 9. The excited S -, P -, and D -wave entries extend the compact spectrum into the 3.7–4.5 GeV region, where several rearrangement channels are naturally open.

Comparison with other theoretical studies shows that the present $\bar{\mathbf{3}} - \mathbf{3}$ scalar and axial-vector masses lie above the older chiral SU(3) quark-model estimates of Zhang *et al.* [37], which placed scalar configurations around 2.75–3.12 GeV and axial-vector configurations around 2.88–3.07 GeV. They are closer to QCD sum-rule estimates for related doubly strange open-flavor tetraquarks, which give central values near 3.02, 3.20, and 3.49 GeV for 0^+ , 1^+ , and 2^+ assignments [35]. Recent complex-scaling Gaussian-expansion calculations predict compact $c\bar{s}s\bar{s}$ resonances at still higher masses, with scalar poles near 3726 and 3763 MeV and tensor poles near 3888 and 3923 MeV [58]. The spread among these predictions shows that this sector is highly sensitive to the assumed color basis, continuum coupling, and treatment of compact versus molecular components. The present results sit between the lower chiral-model estimates and the higher complex-scaling resonances, while the $\mathbf{6} - \bar{\mathbf{6}}$ sector remains the most model-dependent part of the spectrum.

The two-meson thresholds in Table 4 provide the first diagnostic for whether a compact tetraquark is expected to be stable against, or open to, rearrangement into meson pairs. The threshold comparison is expressed through $\Delta = M_T - M_{\text{th}}$, so positive values indicate a mass above the corresponding model threshold. In the $\bar{\mathbf{3}} - \mathbf{3}$ ground S -wave sector, the listed $\eta_s D_s$, $\eta_s D_s^*$, ϕD_s , and ϕD_s^* channels have positive offsets for the relevant assignments, showing that rearrangement decays are expected. The $\mathbf{6} - \bar{\mathbf{6}}$ NR ground state is instead below several thresholds, which explains the closed channels and zero entries in the rearrangement-width table. Thus, a zero width in Table 9 should be read as a kinematic result at the central mass rather than as the absence of the corresponding Fierz component.

The tetraquark Regge trajectories in Table 6 and Figs. 3–6 are generally less steep than the mesonic trajectories. In the $\bar{\mathbf{3}} - \mathbf{3}$ configuration, the orbital slope for the $S_T = 0$, $n = 0$ trajectory is 0.3443 (SR) and 0.3519 (NR), corresponding to tetraquark-to-meson ratios of about 0.56 and 0.58. The spin-1 trajectory has slopes 0.4145 and 0.4162, while the spin-2 trajectory has slopes 0.5458 and 0.5352. Radial slopes are closer to the meson slopes, with ratios often in the 0.75–0.95 range. This suggests that radial excitation in the compact tetraquark is more meson-like than orbital excitation, although the heavier multiquark system still produces reduced slopes. The $\mathbf{6} - \bar{\mathbf{6}}$ trajectories show larger irregularities at low excitation, again reflecting the sensitivity of that color configuration.

The tetraquark decay treatment is based on the rearrangement topology

$$c\bar{s}\bar{s}s \rightarrow (c\bar{s})(s\bar{s}),$$

with the final mesons identified as $D_s^{(*)}$ and a hidden-strange state $X_s = \eta, \eta', \phi$. The Fierz spin-color rearrangement selects the allowed meson pairs for each J^P assignment, and the absolute strengths are supplied by the two-point and three-point QCDSR framework. For the scalar 0^+ tetraquark, the leading modes are $D_s\eta$, $D_s\eta'$, and $D_s^*\phi$. In the $\bar{\mathbf{3}} - \mathbf{3}$ configuration, the total primary width is 20.705 MeV (SR) and 21.221 MeV (NR), while the $\mathbf{6} - \bar{\mathbf{6}}$ SR scalar width is larger, 47.198 MeV. The $\mathbf{6} - \bar{\mathbf{6}}$ NR scalar state

has only the $D_s\eta$ mode open at the central mass, giving 8.360 MeV.

For the axial-vector 1^+ tetraquark, the dominant rearrangement modes are $D_s\phi$, $D_s^*\eta$, and $D_s^*\eta'$. The $D_s\phi$ channel is the largest individual contribution, giving 5.745 MeV (SR) and 5.878 MeV (NR) in the $\bar{\mathbf{3}} - \mathbf{3}$ configuration. Including the two D_s^* pseudoscalar modes gives total widths of 10.488 MeV and 10.688 MeV. In the $\mathbf{6} - \bar{\mathbf{6}}$ SR case the total becomes 22.826 MeV, whereas the $\mathbf{6} - \bar{\mathbf{6}}$ NR axial-vector state is below the corresponding central thresholds. For the tensor 2^+ tetraquark, the leading retained mode is $D_s^*\phi$, with widths of 5.177 MeV (SR) and 5.213 MeV (NR) in the $\bar{\mathbf{3}} - \mathbf{3}$ configuration and 9.307 MeV in the $\mathbf{6} - \bar{\mathbf{6}}$ SR configuration. The $\mathbf{6} - \bar{\mathbf{6}}$ NR tensor channel is closed at the central mass.

Tables 10, 11, and 12 translate these primary modes into one-daughter spectator-cascade final states. The construction is deliberately one daughter at a time: for $T_J \rightarrow H_a H_b$, either H_a is decayed while H_b remains on shell, or H_b is decayed while H_a remains on shell. The cascade rate is therefore

$$\Gamma(T_J \rightarrow [H_a \rightarrow f_a]H_b) = \Gamma(T_J \rightarrow H_a H_b)\mathcal{B}(H_a \rightarrow f_a),$$

and similarly for H_b . These tables are not exclusive-width tables to be summed into a second total; they are alternative reconstruction guides for the same primary two-body widths in Table 9. The most useful experimental handles are the large nonleptonic D_s daughter modes, D_s^* feed-down through $D_s\gamma$ and $D_s\pi^0$, and hidden-strange reconstructions such as $\phi \rightarrow K^+K^-$ and $\eta^{(\prime)}$ hadronic or radiative decays.

Overall, the most robust $\bar{\mathbf{3}} - \mathbf{3}$ ground-state tetraquark signals are expected to be moderately narrow rearrangement decays, with total primary widths of about 21 MeV for 0^+ , 10–11 MeV for 1^+ , and about 5 MeV for 2^+ . The $\mathbf{6} - \bar{\mathbf{6}}$ SR states are generally broader, with primary widths near 47 MeV, 23 MeV, and 9 MeV for the same spin sequence, while the $\mathbf{6} - \bar{\mathbf{6}}$ NR ground states are often below threshold and therefore have fewer open two-body rearrangement channels. In the absence of established experimental $cs\bar{s}\bar{s}$ tetraquark candidates, the combined use of threshold offsets, primary rearrangement widths, and one-daughter spectator-cascade channels provides the clearest phenomenological guide for future searches.

7 Conclusion

The article has been recast around the compact $cs\bar{s}\bar{s}$ tetraquark rather than a parallel discussion of conventional and exotic charm–strange systems. The D_s spectrum is retained as a necessary calibration and threshold input, while the main physics output is the $[cs][\bar{s}\bar{s}]$ spectrum, its color dependence, its position relative to $D_s^{(*)}\eta^{(\prime)}$ and $D_s^{(*)}\phi$ thresholds, and its rearrangement decay widths. In the preferred $\bar{\mathbf{3}} - \mathbf{3}$ color configuration, the ground $J^P = 0^+, 1^+, 2^+$ multiplet lies in the few-GeV region and gives moderately narrow primary rearrangement widths. The $\mathbf{6} - \bar{\mathbf{6}}$ configuration is more model-sensitive, especially in the non-relativistic treatment, and should be interpreted together with threshold offsets and open-channel information rather than central masses alone.

The most direct experimental signatures suggested by this analysis are hidden-strangeness open-charm final states of the form $D_s^{(*)}\eta$, $D_s^{(*)}\eta'$, and $D_s^{(*)}\phi$, followed by clean daughter modes such as $\phi \rightarrow K^+K^-$ and D_s^* feed-down. Comparison with chiral SU(3), QCD-sum-rule, molecular, and complex-scaling calculations shows that the $cs\bar{s}\bar{s}$ sector remains highly model dependent, but the convergence of several approaches on axial-diquark spin multiplets and $D_s^{(*)}X_s$ thresholds makes this flavor channel a well-defined target for future open-charm exotic searches.

References

- [1] M. Gell-Mann, “A schematic model of baryons and mesons,” Phys. Lett. **8**, 214–215 (1964), doi:10.1016/S0031-9163(64)92001-3.

- [2] G. Zweig, “An SU(3) model for strong interaction symmetry and its breaking. Version 1,” CERN-TH-401 (1964).
- [3] S. Navas *et al.* [Particle Data Group], “Review of particle physics,” Phys. Rev. D **110**, no.3, 030001 (2024) and 2025 update, doi:10.1103/PhysRevD.110.030001.
- [4] R. L. Jaffe, “Multiquark hadrons. I. Phenomenology of $Q^2\bar{Q}^2$ mesons,” Phys. Rev. D **15**, 267 (1977), doi:10.1103/PhysRevD.15.267.
- [5] R. L. Jaffe, “Multiquark hadrons. II. Methods,” Phys. Rev. D **15**, 281 (1977), doi:10.1103/PhysRevD.15.281.
- [6] S.-K. Choi *et al.* [Belle], “Observation of a narrow charmonium-like state in exclusive $B^\pm \rightarrow K^\pm\pi^+\pi^-J/\psi$ decays,” Phys. Rev. Lett. **91**, 262001 (2003), arXiv:hep-ex/0309032, doi:10.1103/PhysRevLett.91.262001.
- [7] M. Ablikim *et al.* [BESIII], “Observation of a charged charmoniumlike structure in $e^+e^- \rightarrow \pi^+\pi^-J/\psi$ at $\sqrt{s} = 4.26$ GeV,” Phys. Rev. Lett. **110**, 252001 (2013), arXiv:1303.5949 [hep-ex], doi:10.1103/PhysRevLett.110.252001.
- [8] R. Aaij *et al.* [LHCb], “Observation of the resonant character of the $Z(4430)^-$ state,” Phys. Rev. Lett. **112**, no.22, 222002 (2014), arXiv:1404.1903 [hep-ex], doi:10.1103/PhysRevLett.112.222002.
- [9] R. Aaij *et al.* [LHCb], “Observation of new resonances decaying to $J/\psi K^+$ and $J/\psi\phi$,” Phys. Rev. Lett. **127**, no.8, 082001 (2021), arXiv:2103.01803 [hep-ex], doi:10.1103/PhysRevLett.127.082001.
- [10] R. Aaij *et al.* [LHCb], “Model-independent study of structure in $B^+ \rightarrow D^+D^-K^+$ decays,” Phys. Rev. Lett. **125**, 242001 (2020), arXiv:2009.00025 [hep-ex], doi:10.1103/PhysRevLett.125.242001.
- [11] R. Aaij *et al.* [LHCb], “Amplitude analysis of the $B^+ \rightarrow D^+D^-K^+$ decay,” Phys. Rev. D **102**, no.11, 112003 (2020), arXiv:2009.00026 [hep-ex], doi:10.1103/PhysRevD.102.112003.
- [12] F.-K. Guo, C. Hanhart, U.-G. Meißner, Q. Wang, Q. Zhao and B.-S. Zou, “Hadronic molecules,” Rev. Mod. Phys. **90**, no.1, 015004 (2018), arXiv:1705.00141 [hep-ph], doi:10.1103/RevModPhys.90.015004.
- [13] M. Berwein, N. Brambilla, A. Mohapatra and A. Vairo, “Hybrids, tetraquarks, pentaquarks, doubly heavy baryons, and quarkonia in Born–Oppenheimer effective theory,” Phys. Rev. D **110**, no.9, 094040 (2024), arXiv:2408.04719 [hep-ph], doi:10.1103/PhysRevD.110.094040.
- [14] B. Aubert *et al.* [BaBar], “Observation of a narrow meson decaying to $D_s^+\pi^0$ at a mass of 2.32 GeV/ c^2 ,” Phys. Rev. Lett. **90**, 242001 (2003), arXiv:hep-ex/0304021, doi:10.1103/PhysRevLett.90.242001.
- [15] D. Besson *et al.* [CLEO], “Observation of a narrow resonance of mass 2.46 GeV/ c^2 decaying to $D_s^{*+}\pi^0$ and confirmation of the $D_{sJ}^*(2317)$ state,” Phys. Rev. D **68**, 032002 (2003); Erratum: Phys. Rev. D **75**, 119908 (2007), arXiv:hep-ex/0305100, doi:10.1103/PhysRevD.68.032002.
- [16] P. Krokovny *et al.* [Belle], “Observation of the $D_{sJ}(2317)$ and $D_{sJ}(2457)$ in B decays,” Phys. Rev. Lett. **91**, 262002 (2003), arXiv:hep-ex/0308019, doi:10.1103/PhysRevLett.91.262002.
- [17] S. Godfrey and N. Isgur, “Mesons in a relativized quark model with chromodynamics,” Phys. Rev. D **32**, 189–231 (1985), doi:10.1103/PhysRevD.32.189.
- [18] A. Faessler, T. Gutsche, V. E. Lyubovitskij and Y.-L. Ma, “Strong and radiative decays of the $D_{s0}^*(2317)$ meson in the DK -molecule picture,” Phys. Rev. D **76**, 014005 (2007), arXiv:0705.0254 [hep-ph], doi:10.1103/PhysRevD.76.014005.

- [19] G. Moir, M. Peardon, S. M. Ryan, C. E. Thomas and D. J. Wilson, “Coupled-channel $D\pi$, $D\eta$ and $D_s\bar{K}$ scattering from lattice QCD,” *JHEP* **10**, 011 (2016), arXiv:1607.07093 [hep-lat], doi:10.1007/JHEP10(2016)011.
- [20] R. Aaij *et al.* [LHCb], “Observation of the $T_{cs0}^*(2870)^0$ in the $B \rightarrow DD^0 K_S^0$ decay,” *Phys. Rev. Lett.* **134**, no.10, 101901 (2025), arXiv:2411.19781 [hep-ex], doi:10.1103/PhysRevLett.134.101901.
- [21] M. Di Pierro and E. Eichten, “Excited Heavy-Light Systems and Hadronic Transitions,” *Phys. Rev. D* **64**, 114004 (2001), arXiv:hep-ph/0104208, doi:10.1103/PhysRevD.64.114004.
- [22] D. Ebert, R. N. Faustov and V. O. Galkin, “Heavy-light meson spectroscopy and Regge trajectories in the relativistic quark model,” *Eur. Phys. J. C* **66**, 197–206 (2010), arXiv:0910.5612 [hep-ph], doi:10.1140/epjc/s10052-010-1233-6.
- [23] N. Devlani and A. K. Rai, “Spectroscopy and decay properties of the D_s meson,” *Phys. Rev. D* **84**, 074030 (2011), doi:10.1103/PhysRevD.84.074030.
- [24] V. Kher, N. Devlani and A. K. Rai, “Excited state mass spectra, decay properties and Regge trajectories of charm and charm-strange mesons,” *Chin. Phys. C* **41**, no.7, 073101 (2017), arXiv:1704.00439 [hep-ph], doi:10.1088/1674-1137/41/7/073101.
- [25] V. H. Kher, A. K. Rai and T. Vijay, “Interpreting charm-strange mesons with a screened potential model,” *Few Body Syst.* **62**, 42 (2021), doi:10.1007/s00601-021-01651-y.
- [26] N. Devlani and A. K. Rai, “Spectroscopy and decay properties of the D meson,” *Int. J. Theor. Phys.* **52**, 2196–2208 (2013), doi:10.1007/s10773-013-1494-6.
- [27] W. A. Bardeen, E. J. Eichten and C. T. Hill, “Chiral multiplets of heavy-light mesons,” *Phys. Rev. D* **68**, 054024 (2003), arXiv:hep-ph/0305049, doi:10.1103/PhysRevD.68.054024.
- [28] E. E. Kolomeitsev and M. F. M. Lutz, “On heavy-light meson resonances and chiral symmetry,” *Phys. Lett. B* **582**, 39–48 (2004), arXiv:hep-ph/0307133, doi:10.1016/j.physletb.2003.10.118.
- [29] E. van Beveren and G. Rupp, “Observed $D_s(2317)$ and tentative $D(2100 - 2300)$ as the charmed cousins of the light scalar nonet,” *Phys. Rev. Lett.* **91**, 012003 (2003), arXiv:hep-ph/0305035, doi:10.1103/PhysRevLett.91.012003.
- [30] D. Mohler, C. B. Lang, L. Leskovec, S. Prelovsek and R. M. Woloshyn, “ $D_{s0}^*(2317)$ Meson and D -Meson-Kaon Scattering from Lattice QCD,” *Phys. Rev. Lett.* **111**, no.22, 222001 (2013), arXiv:1308.3175 [hep-lat], doi:10.1103/PhysRevLett.111.222001.
- [31] C. B. Lang, L. Leskovec, D. Mohler, S. Prelovsek and R. M. Woloshyn, “ D_s mesons with DK and D^*K scattering near threshold,” *Phys. Rev. D* **90**, no.3, 034510 (2014), arXiv:1403.8103 [hep-lat], doi:10.1103/PhysRevD.90.034510.
- [32] D. Ebert, R. N. Faustov and V. O. Galkin, “Masses of heavy tetraquarks in the relativistic quark model,” *Eur. Phys. J. C* **67**, 513–524 (2010), arXiv:0910.5612 [hep-ph], doi:10.1140/epjc/s10052-010-1297-8.
- [33] M. A. Shifman, A. I. Vainshtein and V. I. Zakharov, “QCD and resonance physics. Theoretical foundations,” *Nucl. Phys. B* **147**, 385–447 (1979), doi:10.1016/0550-3213(79)90022-1.
- [34] M. A. Shifman, A. I. Vainshtein and V. I. Zakharov, “QCD and resonance physics. Applications,” *Nucl. Phys. B* **147**, 448–518 (1979), doi:10.1016/0550-3213(79)90023-3.

- [35] X.-S. Yang, Q. Xin and Z.-G. Wang, “Analysis of the $T_{c\bar{s}}(2900)$ and related tetraquark states with the QCD sum rules,” *Int. J. Mod. Phys. A* **38**, 2350056 (2023), arXiv:2302.01718 [hep-ph], doi:10.1142/S0217751X23500562.
- [36] B. Wang, K. Chen, L. Meng and S.-L. Zhu, “Spectrum of the molecular tetraquarks: Unraveling the $T_{cs0}(2900)$ and $T_{c\bar{s}0}^a(2900)$,” *Phys. Rev. D* **109**, 034027 (2024), arXiv:2309.02191 [hep-ph], doi:10.1103/PhysRevD.109.034027.
- [37] H.-X. Zhang, W.-L. Wang and Z.-Y. Zhang, “Chiral SU(3) quark model study of tetraquark states: $cn\bar{n}\bar{s}/cs\bar{s}\bar{s}$,” *Commun. Theor. Phys.* **49**, 414–420 (2008), arXiv:hep-ph/0607207, doi:10.1088/0253-6102/49/2/35.
- [38] R. Tiwari, D. P. Rathaud and A. K. Rai, “Spectroscopy of all charm tetraquark states,” *Indian J. Phys.* **97**, 943–954 (2023), doi:10.1007/s12648-022-02427-8.
- [39] R. Tiwari and A. K. Rai, “Mass spectra and decay properties of hidden charm-hidden strange tetraquark states,” *Few Body Syst.* **64**, no.2, 20 (2023), arXiv:2206.04478 [hep-ph], doi:10.1007/s00601-023-01805-0.
- [40] C. Lodha and A. K. Rai, “Mass spectra and decay properties of all-light tetraquark states,” *Few Body Syst.* **65**, no.4, 99 (2024), arXiv:2410.14246 [hep-ph], doi:10.1007/s00601-024-01968-4.
- [41] C. Lodha and A. K. Rai, “Spectroscopy and decay properties of light-strange tetraquark states,” *Indian J. Phys.* **99**, 3055–3081 (2025), arXiv:2412.05874 [hep-ph], doi:10.1007/s12648-024-03524-6.
- [42] C. Lodha and A. K. Rai, “Exploring charm bound states: Mass spectra and decay behavior of mesons and tetraquarks,” arXiv:2505.22393 [hep-ph].
- [43] C. Lodha and A. K. Rai, “Spectroscopy and decay properties of open-charm tetraquarks in the diquark–antidiquark picture,” 2024.
- [44] W. Lucha, F. F. Schoberl and D. Gromes, “Bound states of quarks,” *Phys. Rept.* **200**, 127–240 (1991), doi:10.1016/0370-1573(91)90001-3.
- [45] Y. Koma and M. Koma, “Spin-dependent potentials from lattice QCD,” *Nucl. Phys. B* **769**, 79–107 (2007), arXiv:hep-lat/0609078, doi:10.1016/j.nuclphysb.2007.01.033.
- [46] Y. Koma, M. Koma and H. Wittig, “Nonperturbative determination of the QCD potential at $O(1/m)$,” *PoS LATTICE2012*, 140 (2012), arXiv:1211.6795 [hep-lat], doi:10.22323/1.164.0140.
- [47] V. Patel, K. Gandhi and A. K. Rai, “Interpreting charm-strange mesons with a screened potential model,” *Few Body Syst.* **62**, 68 (2021), doi:10.1007/s00601-021-01651-y.
- [48] R.-H. Ni, Q. Li and X.-H. Zhong, “Mass spectra and strong decays of charmed and charmed-strange mesons,” *Phys. Rev. D* **105**, 056006 (2022), arXiv:2110.05024 [hep-ph], doi:10.1103/PhysRevD.105.056006.
- [49] S. Godfrey and K. Moats, “Properties of excited charm and charm-strange mesons,” *Phys. Rev. D* **93**, 034035 (2016), arXiv:1510.08305 [hep-ph], doi:10.1103/PhysRevD.93.034035.
- [50] P. Jakhad and A. K. Rai, “Relativistic flux-tube model predictions from charmed mesons to double-charmed baryons,” *Phys. Rev. D* **113**, 054046 (2026), arXiv:2509.24772 [hep-ph], doi:10.1103/bkwy-5hr9.

- [51] A. Esposito, A. Pilloni and A. D. Polosa, “Multiquark resonances,” *Phys. Rept.* **668**, 1–97 (2017), arXiv:1611.07920 [hep-ph], doi:10.1016/j.physrep.2016.11.002.
- [52] V. R. Debastiani and F. S. Navarra, “A non-relativistic model for the $[cc][\bar{c}\bar{c}]$ tetraquark,” *Chin. Phys. C* **43**, 013105 (2019), arXiv:1706.07553 [hep-ph], doi:10.1088/1674-1137/43/1/013105.
- [53] V. R. Debastiani and F. S. Navarra, “Spectroscopy of the all-charm tetraquark,” 2016.
- [54] S. Fredriksson, M. Jandel and T. I. Larsson, “Diquark deuteron, tetrons and heavy baryons,” *Phys. Rev. Lett.* **46**, 1135 (1981), doi:10.1103/PhysRevLett.46.1135.
- [55] J. K. Chen, J. Q. Xie, X. Feng and H. Song, *Eur. Phys. J. C* (2023) doi:10.1140/epjc/s10052-023-12329-6
- [56] J. K. Chen, X. Feng and J. Q. Xie, *JHEP* **10**, 052 (2023) doi:10.1007/JHEP10(2023)052
- [57] C. Lodha and A. K. Rai, “Mass spectra and Regge trajectories of charm tetraquark systems,” 2024.
- [58] X.-H. Zheng, Y. Ma and S.-L. Zhu, “Singly heavy tetraquark resonant states with multiple strange quarks,” arXiv:2510.01505 [hep-ph].
- [59] C. Lodha and A. K. Rai, *Eur. Phys. J. Plus* **139**, 663 (2024) doi:10.1140/epjp/s13360-024-05461-z
- [60] T. Regge, *Nuovo Cim.* **14**, 951-976 (1959) doi:10.1007/BF02728177
- [61] G. F. Chew and S. C. Frautschi, *Phys. Rev. Lett.* **8**, 41-44 (1962) doi:10.1103/PhysRevLett.8.41
- [62] P. D. B. Collins, Cambridge University Press, Cambridge (1977)
- [63] A. Tang and J. W. Norbury, *Phys. Rev. D* **62**, 016006 (2000) doi:10.1103/PhysRevD.62.016006 [arXiv:hep-ph/0004078 [hep-ph]].
- [64] A. Selem and F. Wilczek, [arXiv:hep-ph/0602128 [hep-ph]].
- [65] J. Oudichhya, K. Gandhi and A. K. Rai, *Phys. Rev. D* **108**, no.1, 014034 (2023) doi:10.1103/PhysRevD.108.014034
- [66] J. Oudichhya and A. K. Rai, *Int. J. Mod. Phys. A* **39**, no.28, 2443004 (2024) doi:10.1142/S0217751X24430048
- [67] J. Oudichhya and A. K. Rai, *Eur. Phys. J. A* **59**, 123 (2023) doi:10.1140/epja/s10050-023-01024-5
- [68] J. Oudichhya and A. K. Rai, *Eur. Phys. J. A* **60**, 125 (2024) doi:10.1140/epja/s10050-024-01344-0
- [69] S. S. Agaev, K. Azizi and H. Sundu, *Eur. Phys. J. C* **78**, no.2, 141 (2018) doi:10.1140/epjc/s10052-018-5640-4 [arXiv:1801.03925 [hep-ph]].
- [70] H. X. Chen, *Chin. Phys. C* **44**, no.11, 114003 (2020) doi:10.1088/1674-1137/abae4b [arXiv:1910.03269 [hep-ph]].
- [71] F. De Fazio and M. R. Pennington, “Probing scalar mesons in semileptonic decays of D_s and B_s ,” *Phys. Lett. B* **521**, 15–21 (2001), arXiv:hep-ph/0104289, doi:10.1016/S0370-2693(01)01172-5.
- [72] C. Aydin and A. H. Yilmaz, “Semileptonic D_s decays in a constituent quark model,” *Int. J. Mod. Phys. A* **20**, 771–784 (2005).
- [73] S. Kazemi and N. Ghahramany, “Semileptonic decays of charmed-strange mesons,” 2017.

- [74] F. De Fazio and M. R. Pennington, “Branching ratios for D_s semileptonic decays to η and η' ,” JHEP **07**, 051 (2000), arXiv:hep-ph/0006007, doi:10.1088/1126-6708/2000/07/051.
- [75] S.-Y. Yu, X.-W. Kang and V. O. Galkin, “Semileptonic decays of D and D_s mesons in the relativistic quark model,” Front. Phys. **18**, 64301 (2023).
- [76] I. Bediaga and J. H. Miranda, “Direct CP violation in charm decays,” Phys. Rev. D **70**, 094025 (2004), arXiv:hep-ph/0406339, doi:10.1103/PhysRevD.70.094025.
- [77] C. Lodha and A. K. Rai, “Exploring charm bound states: Mass spectra and decay behavior of mesons and tetraquarks,” arXiv:2505.22393 [hep-ph].
- [78] Z. Shah, K. Thakkar and A. K. Rai, “Excited state mass spectra of singly charmed mesons,” 2014.
- [79] M. Ablikim *et al.* [BESIII Collaboration], “Precision measurements of $D_s^+ \rightarrow \eta e^+ \nu_e$ and $D_s^+ \rightarrow \eta' e^+ \nu_e$,” Phys. Rev. D **108**, 092003 (2023), arXiv:2306.05194 [hep-ex], doi:10.1103/PhysRevD.108.092003.
- [80] M. Ablikim *et al.* [BESIII Collaboration], “Measurements of the branching fractions of semileptonic D_s^+ decays via $e^+ e^- \rightarrow D_s^{*+} D_s^{*-}$,” Phys. Rev. D **110**, 072017 (2024), arXiv:2406.01332 [hep-ex], doi:10.1103/PhysRevD.110.072017.
- [81] M. Ablikim *et al.* [BESIII Collaboration], “Observation of $D_s^+ \rightarrow \eta' \mu^+ \nu_\mu$, precision test of lepton flavor universality with $D_s^+ \rightarrow \eta^{(\prime)} \ell^+ \nu_\ell$, and first measurements of $D_s^+ \rightarrow \eta^{(\prime)} \mu^+ \nu_\mu$ decay dynamics,” Phys. Rev. Lett. **132**, 091802 (2024), arXiv:2307.12852 [hep-ex], doi:10.1103/PhysRevLett.132.091802.
- [82] J. Yelton *et al.* [CLEO Collaboration], “Absolute branching fraction measurements for exclusive D_s semileptonic decays,” Phys. Rev. D **80**, 052007 (2009), arXiv:0903.0601 [hep-ex], doi:10.1103/PhysRevD.80.052007.
- [83] J. Hietala, D. Cronin-Hennessy, T. Pedlar and I. Shipsey, “Exclusive D_s semileptonic branching fraction measurements,” Phys. Rev. D **92**, no.1, 012009 (2015), arXiv:1505.04205 [hep-ex], doi:10.1103/PhysRevD.92.012009.
- [84] M. Ablikim *et al.* [BESIII Collaboration], “Studies of the decay $D_s^+ \rightarrow K^+ K^- \mu^+ \nu_\mu$,” JHEP **12**, 072 (2023), arXiv:2307.03024 [hep-ex], doi:10.1007/JHEP12(2023)072.
- [85] M. Ablikim *et al.* [BESIII Collaboration], “Improved measurement of the semileptonic decay $D_s^+ \rightarrow K^0 e^+ \nu_e$,” Phys. Rev. D **110**, 052012 (2024), arXiv:2406.19190 [hep-ex], doi:10.1103/PhysRevD.110.052012.
- [86] B. Aubert *et al.* [BABAR Collaboration], “Study of the decay $D_s^+ \rightarrow K^+ K^- e^+ \nu_e$,” Phys. Rev. D **78**, 051101 (2008), arXiv:0807.1599 [hep-ex], doi:10.1103/PhysRevD.78.051101.
- [87] K. M. Ecklund *et al.* [CLEO Collaboration], “Study of the semileptonic decay $D_s^+ \rightarrow f_0(980) e^+ \nu_e$ and implications for $B_s \rightarrow J/\psi f_0$,” Phys. Rev. D **80**, 052009 (2009), arXiv:0907.3201 [hep-ex], doi:10.1103/PhysRevD.80.052009.
- [88] M. Ablikim *et al.* [BESIII Collaboration], “Measurement of absolute branching fractions of D_s^+ hadronic decays,” JHEP **05**, 335 (2024), arXiv:2403.19256 [hep-ex], doi:10.1007/JHEP05(2024)335.
- [89] P. U. E. Onyisi *et al.* [CLEO Collaboration], “Improved measurement of absolute hadronic branching fractions of the D_s^+ meson,” Phys. Rev. D **88**, 032009 (2013), arXiv:1306.5363 [hep-ex], doi:10.1103/PhysRevD.88.032009.

- [90] A. Zupanc *et al.* [Belle Collaboration], “Measurements of branching fractions of leptonic and hadronic D_s^+ meson decays and extraction of the D_s^+ meson decay constant,” JHEP **09**, 139 (2013), arXiv:1307.6240 [hep-ex], doi:10.1007/JHEP09(2013)139.
- [91] H. Mendez *et al.* [CLEO Collaboration], “Measurements of D meson decays to two pseudoscalar mesons,” Phys. Rev. D **81**, 052013 (2010), arXiv:0906.3198 [hep-ex], doi:10.1103/PhysRevD.81.052013.
- [92] C. P. Jessop *et al.* [CLEO Collaboration], “Measurement of the branching ratios for the decays of D_s^+ to $\eta\pi^+$, $\eta'\pi^+$, $\eta\rho^+$, and $\eta'\rho^+$,” Phys. Rev. D **58**, 052002 (1998), arXiv:hep-ex/9801010, doi:10.1103/PhysRevD.58.052002.
- [93] M. Ablikim *et al.* [BESIII Collaboration], “Measurement of the branching fractions of $D_s^+ \rightarrow \eta'X$ and $D_s^+ \rightarrow \eta'\rho^+$ in $e^+e^- \rightarrow D_s^+D_s^-$,” Phys. Lett. B **750**, 466–474 (2015), doi:10.1016/j.physletb.2015.09.059.
- [94] B. Aubert *et al.* [BABAR Collaboration], “Measurement of the $B^0 \rightarrow D^{*-}D_s^{*+}$ and $D_s^+ \rightarrow \phi\pi^+$ branching fractions,” Phys. Rev. D **71**, 091104 (2005), arXiv:hep-ex/0502041, doi:10.1103/PhysRevD.71.091104.
- [95] R. E. Mitchell *et al.* [CLEO Collaboration], “Dalitz plot analysis of $D_s^+ \rightarrow K^+K^-\pi^+$,” Phys. Rev. D **79**, 072008 (2009), arXiv:0903.1301 [hep-ex], doi:10.1103/PhysRevD.79.072008.
- [96] P. del Amo Sanchez *et al.* [BABAR Collaboration], “Dalitz plot analysis of $D_s^+ \rightarrow K^+K^-\pi^+$,” Phys. Rev. D **83**, 052001 (2011), arXiv:1011.4190 [hep-ex], doi:10.1103/PhysRevD.83.052001.
- [97] M. Ablikim *et al.* [BESIII Collaboration], “Amplitude analysis and branching fraction measurement of $D_s^+ \rightarrow K^-K^+\pi^+\pi^0$,” Phys. Rev. D **104**, 032011 (2021), arXiv:2103.02482 [hep-ex], doi:10.1103/PhysRevD.104.032011.
- [98] M. Ablikim *et al.* [BESIII Collaboration], “Amplitude analysis and branching fraction measurement of the decay $D_s^+ \rightarrow K^+\pi^+\pi^-$,” JHEP **08**, 196 (2022), arXiv:2205.08844 [hep-ex], doi:10.1007/JHEP08(2022)196.
- [99] M. Ablikim *et al.* [BESIII Collaboration], “Amplitude analysis and branching fraction measurement of the decay $D_s^+ \rightarrow K^+\pi^+\pi^-\pi^0$,” JHEP **09**, 242 (2022), arXiv:2205.13759 [hep-ex], doi:10.1007/JHEP09(2022)242.
- [100] Y. Guan *et al.* [Belle Collaboration], “Measurement of branching fractions and CP asymmetries for $D_s^+ \rightarrow K^+(\eta, \pi^0)$ and $D_s^+ \rightarrow \pi^+(\eta, \pi^0)$ decays at Belle,” Phys. Rev. D **103**, 112005 (2021), arXiv:2103.09969 [hep-ex], doi:10.1103/PhysRevD.103.112005.
- [101] M. Ablikim *et al.* [BESIII Collaboration], “Measurement of branching fraction of $D_s^{*+} \rightarrow D_s^+\pi^0$ relative to $D_s^{*+} \rightarrow D_s^+\gamma$,” Phys. Rev. D **107**, 032011 (2023), arXiv:2212.13361 [hep-ex], doi:10.1103/PhysRevD.107.032011.
- [102] B. Aubert *et al.* [BABAR Collaboration], “Measurement of the branching ratios $\Gamma(D_s^{*+} \rightarrow D_s^+\pi^0)/\Gamma(D_s^{*+} \rightarrow D_s^+\gamma)$ and $\Gamma(D^{*0} \rightarrow D^0\pi^0)/\Gamma(D^{*0} \rightarrow D^0\gamma)$,” Phys. Rev. D **72**, 091101 (2005), arXiv:hep-ex/0508039, doi:10.1103/PhysRevD.72.091101.
- [103] D. Cronin-Hennessy *et al.* [CLEO Collaboration], “Observation of the Dalitz decay $D_s^{*+} \rightarrow D_s^+e^+e^-$,” Phys. Rev. D **86**, 072005 (2012), arXiv:1104.3265 [hep-ex], doi:10.1103/PhysRevD.86.072005.

- [104] M. Ablikim *et al.* [BESIII Collaboration], “First experimental study of the purely leptonic decay $D_s^{*+} \rightarrow e^+\nu_e$,” Phys. Rev. Lett. **131**, 141802 (2023), arXiv:2304.12159 [hep-ex], doi:10.1103/PhysRevLett.131.141802.
- [105] J. Gronberg *et al.* [CLEO Collaboration], “Measurements of the branching ratios $\Gamma(D_s^{*+} \rightarrow D_s^+\pi^0)/\Gamma(D_s^{*+} \rightarrow D_s^+\gamma)$ and $\Gamma(D^{*0} \rightarrow D^0\pi^0)/\Gamma(D^{*0} \rightarrow D^0\gamma)$,” Phys. Rev. Lett. **75**, 3232–3235 (1995), doi:10.1103/PhysRevLett.75.3232.
- [106] G. T. Blaylock *et al.* [Mark III Collaboration], “Observation of $e^+e^- \rightarrow D_s^\pm D_s^{*\mp}$ at $\sqrt{s} = 4.14$ GeV,” Phys. Rev. Lett. **58**, 2171–2174 (1987), doi:10.1103/PhysRevLett.58.2171.